Dynamical Evolution of Small Solar System Bodies Inferred from Interior Density Distribution and YORP-induced Spin Alteration

by

Masanori Kanamaru

A dissertation submitted to Osaka University in conformity with the requirements for the degree of Doctor of Philosophy.

Osaka, Japan

March, 2020

Primary Reader and Advisor:

Sho Sasaki

Secondary Readers:

Tadashi Kondo

Kentaro Terada

Kazuto Saiki

Tomokatsu Morota

Abstract

Small solar system bodies are minor celestial bodies revolving around the Sun such as asteroids, comets and inter-planetary dust. The small bodies are considered to be remnants in the early stage of the planetary system formation. Small bodies are essential suppliers of volatiles such as water and organic matter to the inner solar system over the snowline, where the volatiles condense at a certain distance from the Sun. Dynamical evolution of the small bodies is a key to shed light on their origins and processes of mass transport in the solar system. In this dissertation, we address (1) numerical simulation of spin state evolution of an asteroid and (2) a new method to estimate interior density distribution within small bodies.

(1) The Japan's spacecraft Hayabusa2 revealed a nature of a near-Earth Asteroid (162173) Ryugu. The top-shaped asteroid has an elevated ridge in the equatorial region, which is considered to be formed by deformation or mass wasting when Ryugu used to be spinning faster. We aimed to evaluate the time scale of the spin-down process from the faster rotation to the current mild rotation and compare it with the surface age estimated from the crater statistics for better understanding the

dynamical evolution of Ryugu.

The YORP effect is known as a secular change in a spin state of an asteroid. The radiation from the surface of the irregularly shaped body is generally asymmetrical and the thermally induced torque changes the rotation period and the spin pole orientation (obliquity). Given Ryugu's orbital elements, spin state and 3D shape model obtained by Hayabusa2, it has turned out that Ryugu is currently decreasing its spin rate. Moreover, we simulated long-term spin evolution of Ryugu with various initial periods and obliquities given. It is found that some initial conditions can reach the current spin state of Ryugu in 0.25 to 2.3 million years. The time scale of the spin alteration is shorter than the surface age of about 9 million years, estimated from the crater statistics on Ryugu. It is indicated that Ryugu experienced a disturbance of its spin such as an impact or an Earth-flyby at least in the last 2.3 million years.

(2) We propose a method to estimate density distribution within small bodies in order to gain additional information about their interiors and formation processes. There are so-called "smooth terrains" on some small bodies, which are flat regions located in areas of potential-lows and covered with finer particles. Our technique is to determine the interior density distribution by fitting the gravity field on the surface to the observed smooth terrain (Kanamaru et al., 2019). With this technique, it is considered that there is a contrast in bulk density by about 20% between the two lobes of asteroid Itokawa. In contrast, Comet 67P/Churyumov-Gerasimenko has global homogeneity in density.

– Below is the abstract in Japanese. –

小惑星・彗星・宇宙塵をはじめとする太陽系小天体（以下、小天体）は、太陽系形成初期の微惑星あるいはその生き残りであると考えられている。揮発性物質が凝縮する低温領域、すなわちスノーラインの外側で形成した小天体が地球に飛来することで、原始地球に水や有機物が供給された。小天体が経験した軌道進化や衝突・破壊・再集積といった力学進化過程を理解することは、小天体の起源を制約し、太陽系内の物質輸送過程を明らかにする上で重要である。小惑星探査機が取得したデータから力学進化過程を復元する手法を確立することを目的として、（１）小惑星の自転状態の進化を再現する数値計算と、（２）小天体内部の密度分布を推定する手法の開発を行った。

（１）日本の小惑星探査機「はやぶさ２」は、2018 年 6 月に小惑星 Ryugu に到着し、詳細な科学観測を行った。小惑星 Ryugu 最大の特徴の一つが、「コマ型」と呼ばれるひし形の天体形状である。赤道域が隆起したコマ型形状は、かつて Ryugu が高速に自転していた時代に、小惑星の変形あるいは表層の物質移動によって形成したと考えられている。本研究は、高速自転の状態（自転周期 ∼ 3.5 h）から現在のゆるやかな自転状態（自転周期 7.6 h）に至る減速過程を明らかにして、小惑星 Ryugu の力学進化史の構築を目指した。

小惑星の自転状態を変化させる現象として、「YORP 効果」が知られている。太陽光に温められた小惑星の表面から熱放射が起こるとき、天体の不規則な形状に起因して異方性が生じる。熱放射の異方性によるトルクは、百万年スケールで小惑星の自転周期や自転軸の向きを変化させる。はやぶさ２が取得した小惑星 Ryugu の軌道・自転・形状に関するデータをもとに、自転速度と自転

軸傾斜角の変化率を計算した。本研究の結果は、Ryugu の自転が現在は減速していることを示唆している。さらに、様々な自転周期と自転軸傾斜角を初期条件として、その後の自転状態の進化を計算した。Ryugu が現在の自転状態に達するまでの時間スケールは 25 万年〜230 万年程度であり、これはクレーターの数密度から見積もられる Ryugu の表層年代〜900 万年に比べると短いことがわかった。これらの結果は、隕石衝突や地球への接近といった自転状態を変化させるイベントが少なくとも 230 万年以内に起きたことを示唆している。

（２）小惑星内部の密度分布は、天体の形成過程を解明するための重要な手がかりである。しかしながら、小惑星探査においては、探査機の軌道から天体の重力場を高精度で決定して、内部構造を制約することが困難である。そこで、小惑星の３次元形状から計算した重力場と地質学的な特徴から密度分布を推定する手法を提案した (Kanamaru et al., 2019)。小惑星には、低地に砂礫が堆積して形成した平坦な地形 (smooth terrain) が見られる。我々の密度分布推定法は、天体形状から抽出した smooth terrain の分布と天体表面における等ポテンシャル面が一致するような密度分布を探索するものである。はやぶさ初号機が探査を行なった小惑星 Itokawa は、二つの楕円体（「頭」と「胴体」）が合体したような形状をもつ。本手法を Itokawa に適用したところ、頭と胴体に 20%程度の密度差（空隙率の差）があることが示唆された。同様の形状をもつ彗星 67P/Churyumov-Gerasimenko にも本手法を適用し、Itokawa とは対照的に、全球で一様な密度分布を示唆する結果を得た。推定された密度分布は、小天体の集積過程を理解する上で重要な示唆を与える。

Acknowledgments

First of all, I am deeply grateful to my advisor, Sho Sasaki. Discussion with him has been inspiring me to advance research over 6 years. His generous guidance has provided me with the greatest opportunity to explore such a wonderful field in accordance with my own interests. In addition, he has treated me as a fully fledged scientist on an equal basis. I would like to acknowledge the other committee members, Tadashi Kondo, Kentaro Terada, Kazuto Saiki and Tomokatsu Morota for their constructive comments to my dissertation. I also appreciate all faculties and students in my laboratory, who produces a relaxing but exciting atmosphere for the sake of my research and graduate life. From Nice Observatory, I owe my deepest gratitude to Mark Wieczorek for exciting collaboration and his continuous supports. I was very glad that he sympathized my research interest and invited me to Nice. His passion and knowledge made a substantial contribution to boost my study.

The Hayabusa spacecraft inspired me in my high school days and brought me to the field of planetary science. Subsequently, Hayabusa2 broaden my horizon with exciting discoveries and collaboration such that I became an independent scientist. I really appreciate such a great opportunity and all of the people who have been involved with me in this project. I also had precious experiences thanks to the supportive teachers and the pleasant colleagues in the CBI program.

Finally, I would like to offer my special thanks to my family members. I could not complete the graduate course and realize my dream to become a scientist without their support and love.

Contents

List of Tables

List of Figures

Chapter 1

Introduction of Asteroids' Dynamics

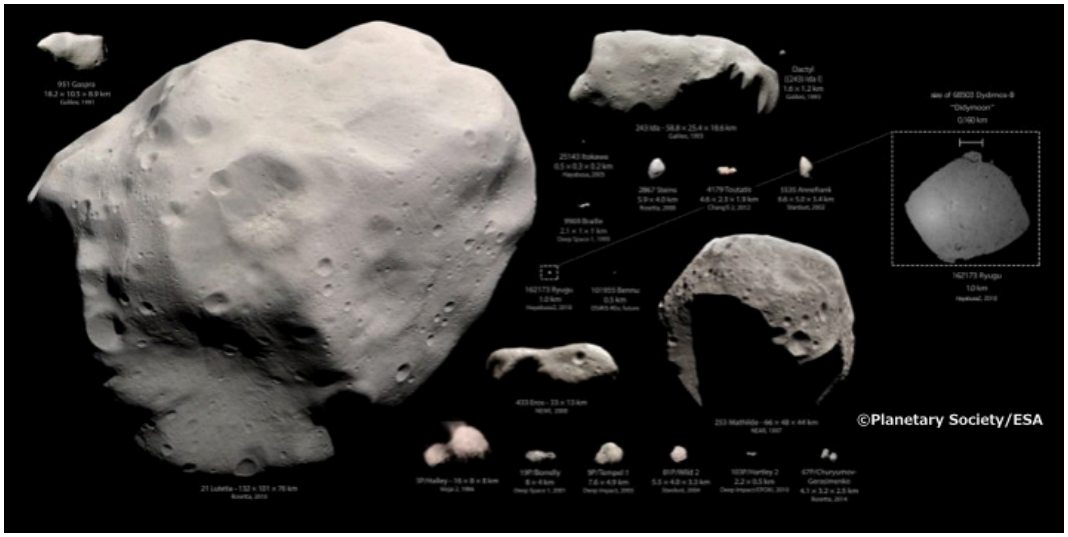

General introduction of dynamical evolution of small solar system bodies.

1.1 Small Solar System Bodies

Small solar system bodies include asteroids, comets and interplanetary dust, which revolve around the Sun. They are considered to be remnants of the early stage of the planetary formation process. The currently observed asteroids exist in clusters (i.e. asteroid families) and are concentrated between Mars and Jupiter orbits, called the main belt (See Figure 1.1). The most primitive small bodies are considered to include pristine materials to provide us with a clue to construct the environment of the early solar system. The initial distribution of materials in the solar system must have been formed according to a distance from the Sun. Rocky asteroids and volatile-rich comets were formed at different locations in the early solar system and have been experienced dynamical evolution. We are required to understand the dynamical processes to evolve the population of the small bodies for the purpose of constructing the history of the solar system. Figure 1.2 describes a possible scenario of the solar system evolution. After the formation of the planets, they are considered to have migrated dynamically by interaction with the accretion disk according to the Grand Tack model (Walsh et al., 2011) and the Nice model (Gomes et al., 2005; Morbidelli et al., 2005; Tsiganis et al., 2005). The planetary migration induced mixing of the materials in the radial direction and removal of small bodies from the inner solar system by the powerful resonances. The other key processes for the dynamical evolution such as collisions and non-gravitational effects are addressed in the next sections.

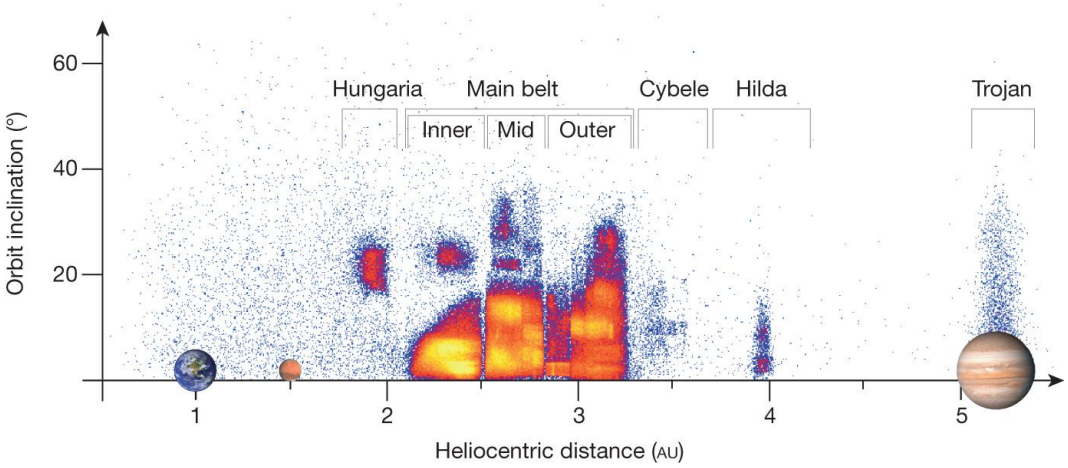

Figure 1.1: Distribution of orbital elements of asteroids, orbital inclination vs. orbital semi-major axis from DeMeo and Carry (2014).

1.2 Collisional Evolution of Small Bodies

Collisions have controlled the dynamical evolution of the solar system in over a wide range of bodies' size. A larger body in the asteroid belt is a reservoir of smaller bodies. Fragmentation by a collisional event can produce next-generation small bodies and will result in the current population of the asteroid belt. The intrinsic collision probability P_i and the mean impact velocity $V_{\rm imp}$ of a group of main belt asteroids are computed by Bottke et al. (1994) and they are reasonable to explain the today's population of the asteroids ($P_i \sim 2.9 \times 10^{-18}$ km^{-2}year^{-1} and $V_{imp} \sim 5.3$ km/s). Figure 1.3 shows the consequent size-frequency distribution (SFD) of asteroids from Bottke et al. (2015). The SFD of fragments estimated by Bottke et al. (2005a) and Bottke et al. (2005b) (solid curves) are consistent with the observed population both in near-Earth and the main belt.

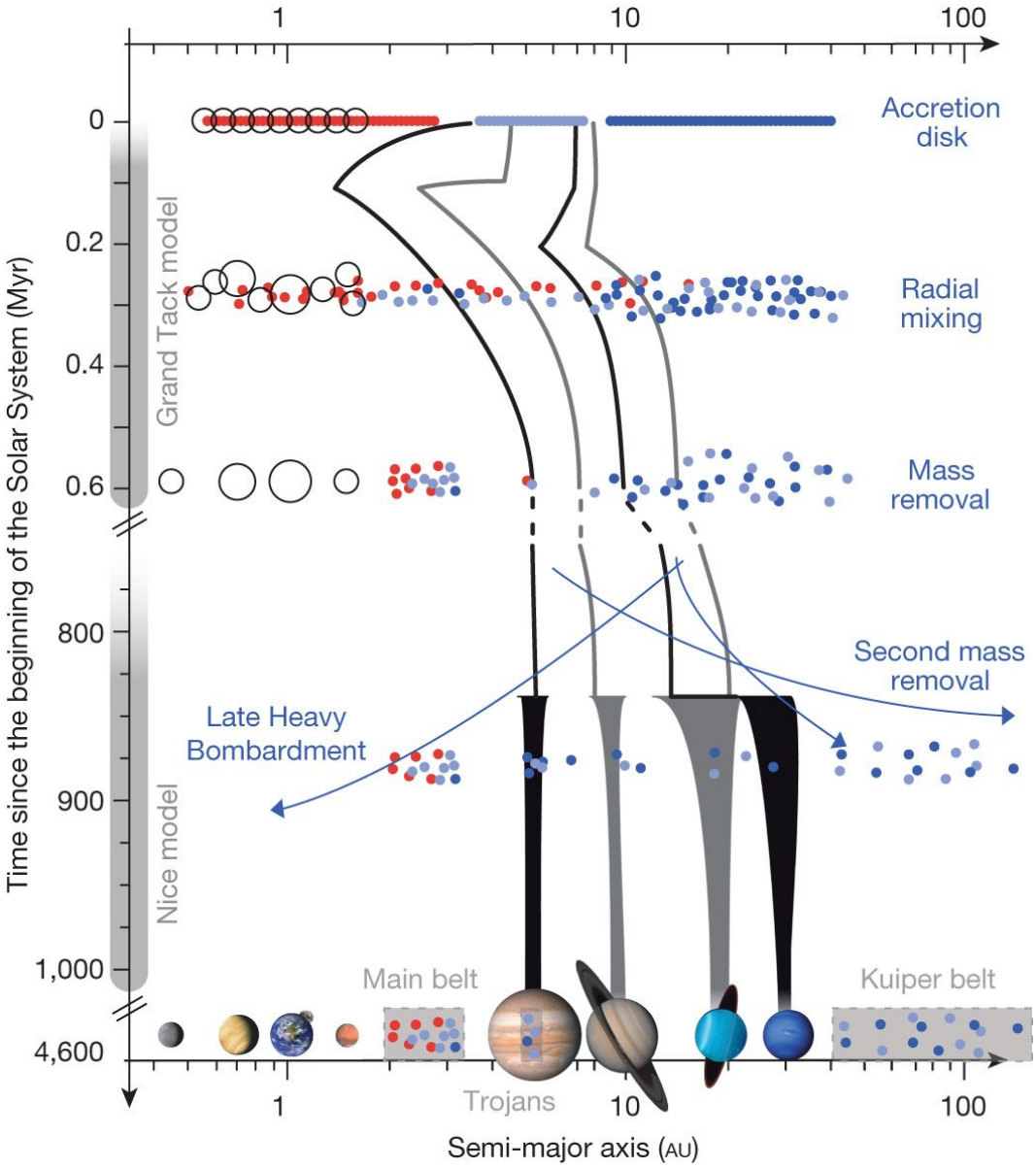

Figure 1.2: Possible scenario of dynamical evolution of the solar system from DeMeo and Carry (2014).

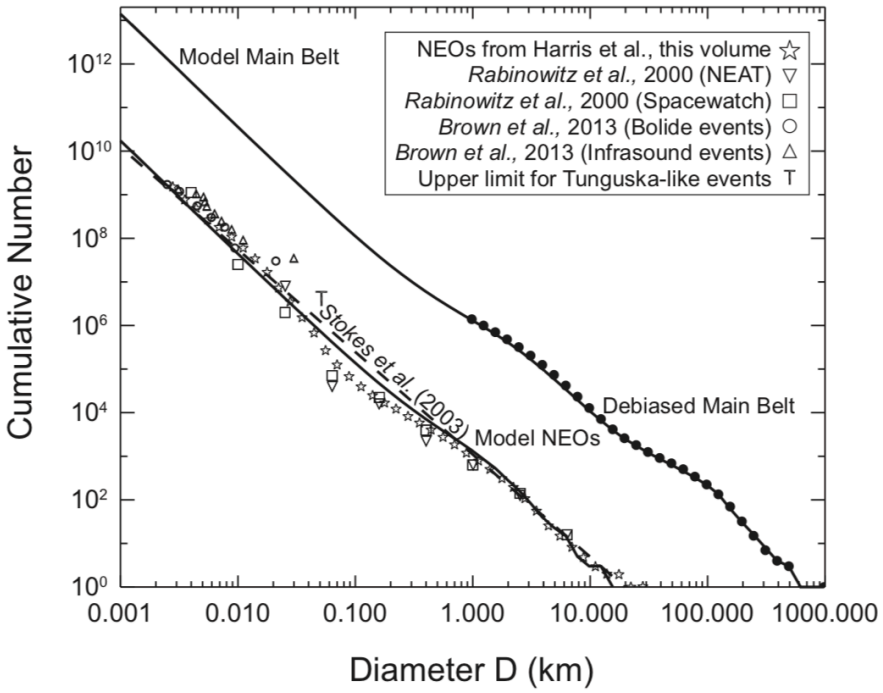

Figure 1.3: Size frequency distributions of asteroids in near-Earth orbits and the main belt (Bottke et al., 2015).

Therefore, it can be said that most of the existing small bodies are fragments, or fragments of fragments. The history of the collisional evolution can be observed as the structure of each asteroid. Some asteroids have consolidated structures with high bulk density similar to that of a meteorite and others have porous structures with lower bulk density. The latter ones are considered to be gravitational aggregates of fragments produced by catastrophic disruption of their parent bodies, which are the so-called "rubble pile" asteroids. Figure 1.4 plots estimated masses of asteroids as functions of bulk density (upper) and porosity (lower). Porosity of an asteroid or a fraction of internal empty space can be calculated from bulk density and grain density of the corresponding meteorite. Rocky asteroids have a wide variety of bulk

densities and porosities depending on their interior structures. The details of density distribution within asteroids will be discussed in Chapter 3.

1.3 Non-Gravitational Effects

As well as the gravitational interactions with the Sun and major planets, non-gravitational effects on small bodies also have contributed to their dynamical evolution. In contrast to stochastic events such as a close encounter with a planet and a collision with another body, photons have great roles in systematic changes of their orbits and spin states. Size-dependence of these effects are essential to explain population, distribution and dynamical lifetimes of small bodies. From larger to smaller bodies, the Yarkovsky and YORP effects, Poynting-Robertson drag and solar radiation pressure perturb their Keplerian orbits around the Sun.

1.3.1 Yarkovsky effect

After a long history since the advocacy of this effect by Ivan O. Yarkovsky (1844–1902), the Yarkovsky effect becomes recognized as a key process to deliver asteroids and meteorites to near-Earth orbits (Hartmann et al., 1999). The Yarkovsky effect is defined as a secular change of an orbital semi-major axis of a small body induced by thermal recoil force. Transportation of materials from the main belt cannot be explained by orbital resonance with the gas giants alone. Without the Yarkovsky drift, a collision event near a resonant orbit is the only process that can

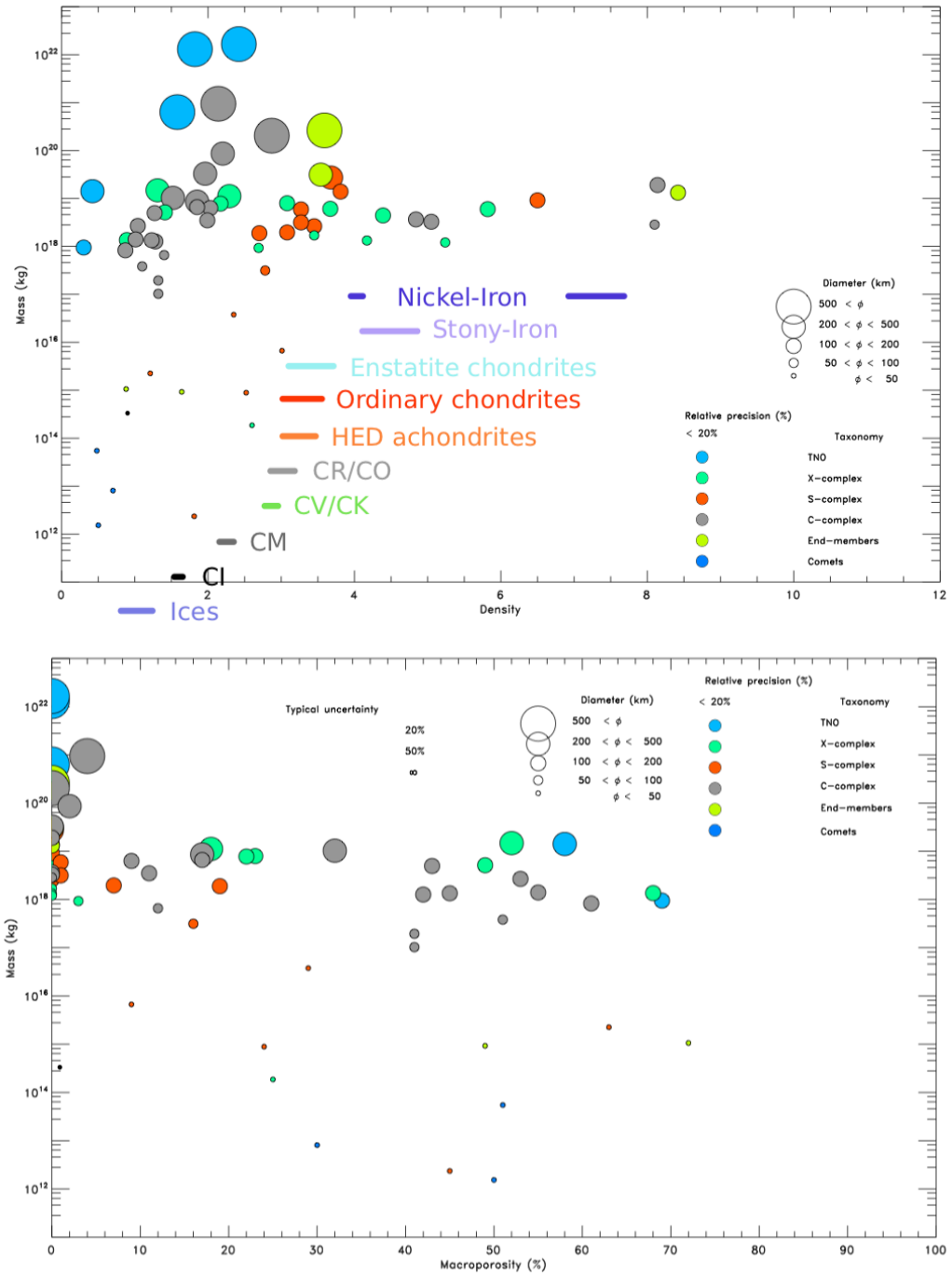

Figure 1.4: Asteroids' mass vs. bulk density (upper) and mass vs. porosity (Carry, 2012).

inject fragments into the "escape hatch" (Bottke et al., 2006). The directly injected fragments will be immediately removed from the resonance orbit in a few million years or less and transferred to the near-Earth orbits (Gladman, 1997). However, meteorite samples have cosmic-ray exposure (CRE) ages equal to or greater than their dynamical lifetimes from the main belt, for example, 10–100 Ma for stony meteorites and 0.1–1 Ga for iron meteorites (Eugster, 2003; Eugster et al., 2006). The CRE ages indicate integral time from the breakup event, which exposed the samples on the surface of the bodies. Hence it follows that the small bodies were transferred to the resonant hatch over a longer distance and a longer period of time. In addition, the combination of the Yarkovsky drift and the orbital resonance is essential to sustain population of Near-Earth asteroids (NEAs) and impactor flux which produces craters on the terrestrial planets in the inner Solar System (Bottke et al., 2005b; McEwen et al., 1997).

Figure 1.5 is a schematic chart from Bottke et al. (2006) about the Yarkovsky force affecting a semi-major axis of an asteroid. The both panels in the figure look down on the orbital plane of the asteroid. The panels (a) and (b) show a prograde rotating asteroid with a pole perpendicular to the orbital plane and an asteroid with a pole along the plane, respectively. The two cases respectively correspond to axial tilt angles or obliquities of 0° and 90°, denoted by ε. A retrograde rotator is expressed with obliquity larger than 90° and obliquity of 180° also corresponds to a spin pole perpendicular to the orbital plane but it is rotating in an opposite direction with respect to the orbital motion.

A "diurnal" Yarkovsky effect increases or decreases the orbital semi-major axis depending on whether the body is a prograde or retrograde rotator. Given non-zero thermal conductivity, the hottest spot on the surface of the irradiated object becomes out of the sub-solar point and shifts eastwards. For the prograde rotator ($\varepsilon \sim 0°$), this offset concentrates thermal radiation from the surface on the back side. Therefore, thermal recoil force is produced so as to increase the orbital velocity and the asteroid will gradually spiral outward. Conversely, a retrograde rotator with $\varepsilon \sim 180°$ will decrease a semi-major axis and spiral inward because the hottest spot appears in the leading hemisphere of the body. On the other hand, a "seasonal" component of the Yarkovsky effect becomes maximum at obliquity of $90°$. In Figure 1.5 (b), an asteroid is spinning around an axis in the orbital plane. The northern hemisphere of the body are irradiated most efficiently at the point A. Subsequently, the hottest season comes in the northern hemisphere at the point B and then thermal recoil force works backward with respect to the orbital motion. The same thing occurs for the southern hemisphere at the points C to D. Net thermal force over a cycle of revolution decreases the semi-major axis and shrink the asteroid's orbit.

By integrating thermal recoil force over a whole surface of a spherical body, the diurnal and seasonal components of the Yarkovsky drift rate are expressed as follows

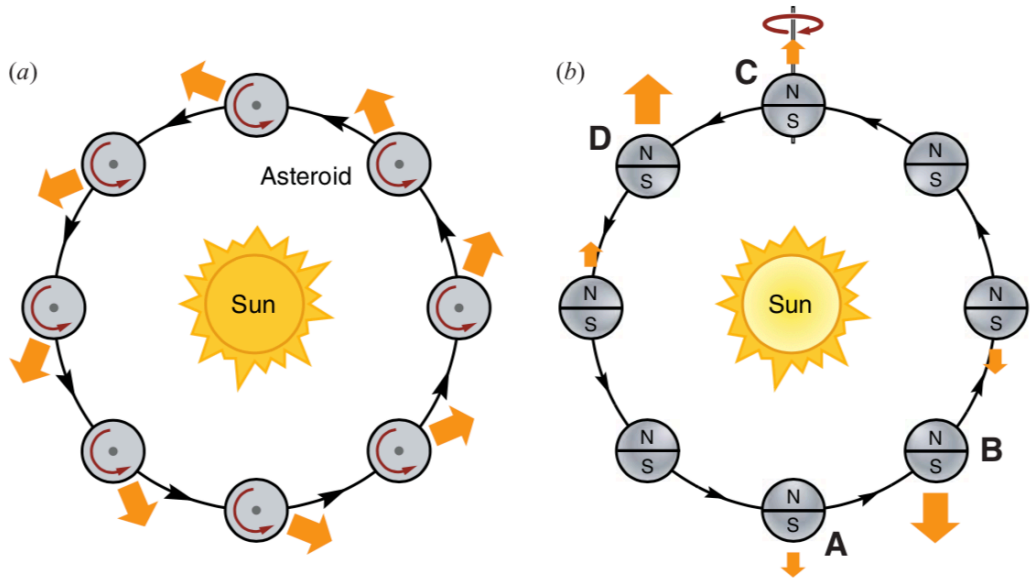

Figure 1.5: The diurnal (a) and seasonal (b) effects of the Yarkovsky drift described by Bottke et al. (2006).

(Bottke et al., 2006; Vokrouhlický et al., 2015).

$$\left(\frac{da}{dt}\right)_{\text{diurnal}} = -\frac{8}{9}\frac{(1-A)\Phi}{n}W(R_\omega, \Theta_\omega)\cos\varepsilon + \mathcal{O}(e) \tag{1.1}$$

$$\left(\frac{da}{dt}\right)_{\text{seasonal}} = \frac{4}{9}\frac{(1-A)\Phi}{n}W(R_n, \Theta_n)\sin^2\varepsilon + \mathcal{O}(e) \tag{1.2}$$

where a, e, and n denote the orbital semi-major axis, eccentricity and mean motion of the asteroid, respectively. A is bond albedo of the body and ε is obliquity of the spin pole. The factor of radiation pressure Φ is expressed as $\Phi = \pi R^2 F/(mc)$, where R and m are the radius and the mass of the spherical body. c is the speed of light and F is the solar radiation flux in a circular orbit of a semi-major axis a. From the expression of the Φ factor, it is clear that the magnitude of the drift rate $|da/dt|$ depends on the body's radius by $\propto R^{-1}$, for the mass m is scaled by $\propto R^3$.

Thus, the Yarkovsky effect dominates orbital evolution of meter- to kilometer-sized bodies. Asteroids larger than 30–40 km will not drift far during their dynamical lifetimes.

Another parameter dependence of the Yarkovsky effect can be seen in the function W, related to a cycle of heating and cooling.

$$W(R_\nu, \Theta_\nu) = -\frac{\kappa_1(R_\nu)\Theta_\nu}{1 + 2\kappa_2(R_\nu)\Theta_\nu + \kappa_3(R_\nu)\Theta_\nu^2} \tag{1.3}$$

where the frequency ν is replaced by either the rotation frequency ω for the diurnal effect or the orbital mean motion n for the seasonal effect as shown in Equations 1.1 and 1.2. The thermal parameter Θ_ν is defined for each frequency of the rotation or the revolution as follows (Vokrouhlický et al., 2015).

$$\Theta_\nu = \frac{\Gamma\sqrt{\nu}}{\epsilon\sigma T_\star^3} \tag{1.4}$$

where ϵ, σ and $T_\star$ are the thermal emissivity of the body, the Stefan-Boltzmann constant and the surface temperature at a sub-solar point, respectively. The thermal inertia Γ is defined as a product of the thermal conductivity K, the density ρ and the heat capacity C of the surface of the body, thus:

$$\Gamma = \sqrt{K\rho C} \tag{1.5}$$

The thermal coefficients κ_i include a non-dimensional radius of the body, which is

defined as $R_\nu = R/l_\nu$. The characteristic length l_ν is the thermal penetration depth where temperature changes during each heat cycle of the frequency ν.

$$l_\nu = \sqrt{\frac{K}{\rho C \nu}} \tag{1.6}$$

You can find a detail of the κ-coefficients as functions of the characteristic radius R_ν of the asteroid in Vokrouhlický (1998).

As mentioned at the beginning of this section, the Yarkovsky effect has an important role to deliver small bodies to resonances. Since the diurnal component changes its sign depending on the direction of rotation, the Yarkovsky effect can separate members of an asteroid family into prograde rotators and retrograde ones, and will further disperse them over time. The size-dependency of the drift rate (*i.e.* smaller bodies are more quickly carried) results in the so-called Yarkovsky V-shape as shown in Figure 1.6. The both panels plot the same data of asteroids' absolute magnitude observed by NASA's Wide-Field Infrared Survey Explorer (WISE) as a function of an orbital semi-major axis. The red and blue curves outline the V-shape distributions of the two different families.

1.3.2 YORP effect

Thermal recoil force on an asteroid's surface can alter not only its orbit but also its spin. In general, scattering of sunlight and thermal reradiation from the surface cannot be completely isotropic because of an irregular shape and surface topography.

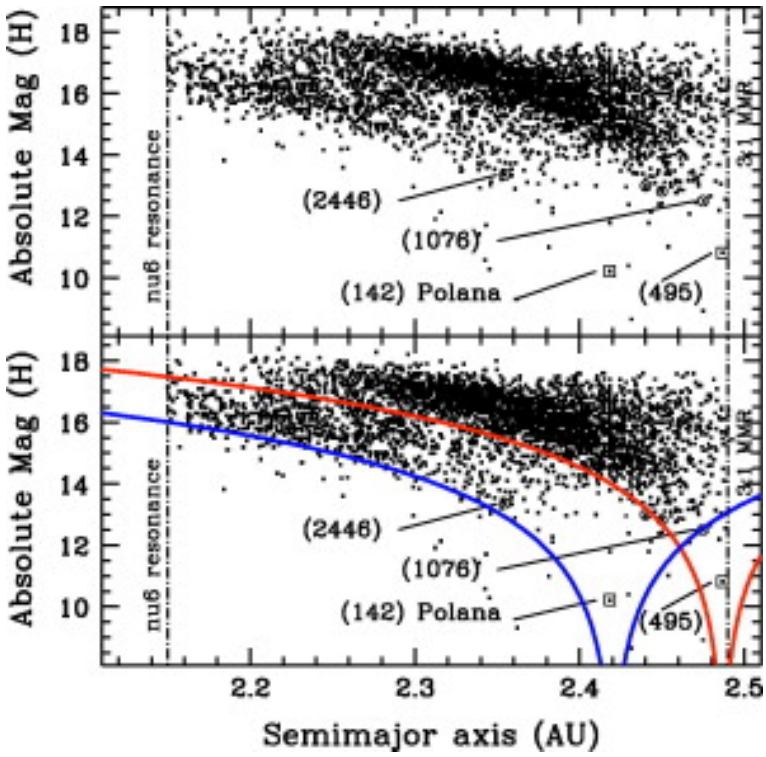

Figure 1.6: Yarkovsky-induced dispersion of family members (Walsh et al., 2013). Absolute magnitude of WISE-observed asteroids are plotted as a function of a semi-major axis.

Resultant torque on the body may alter angular velocity of rotation and obliquity of the spin pole, and may excite precession (Rubincam, 2000). The secular change of the spin state is named Yarkovsky-O'Keefe-Radzievskii-Paddack (YORP) effect after four contributors to the discovery of this phenomenon.

Before detailed YORP modeling of an individual target are described in Chapter 2, we hereby make sure that the YORP effect exists by means of observed distribution of rotation states of asteroids. A catastrophic disruption of a parent body is considered to produce random distribution of spin pole orientations and rotation periods. What is observed in the Koronis asteroid family, however, the distribution of the spin parameters are clustered, not random (Slivan, 2002; Vokrouhlický et al., 2003). Slivan et al. (2008) confirmed a non-Maxwellian distribution of rotation frequencies of 40 Koronis asteroids as a result of spin-down by the YORP torque (See Figure 1.7).

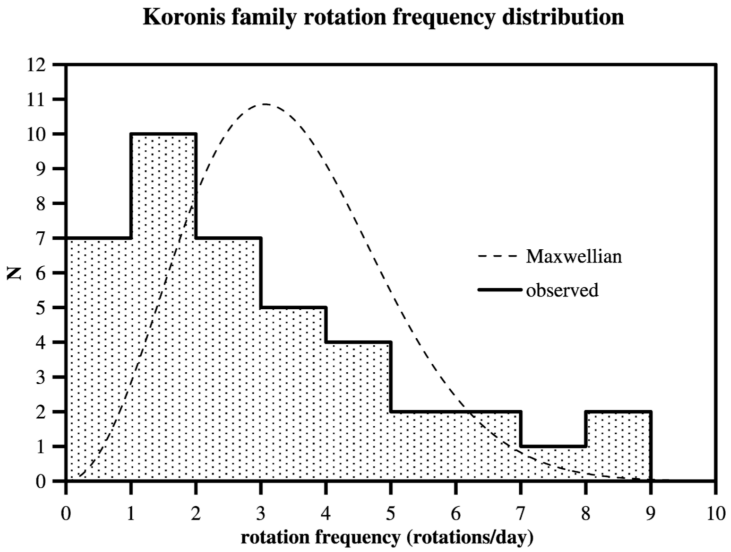

Figure 1.7: The observed rotation frequencies of Koronis family asteroids, compared with a random Maxwellian distribution (Slivan et al., 2008).

In addition, the combination of the Yarkovsky and YORP effects makes an influence on the spin pole distribution of NEAs. As shown in Figure 1.8 from Vokrouhlický et al. (2015), the number of retrograde rotators significantly dominate that of prograde rotators among the NEA population unlike the main belt asteroids. This anisotropic distribution is considered to be derived from a direction of the Yarkovsky drift and a position of a resonant escape hatch in the main belt (Kryszczyńska et al., 2007; La Spina et al., 2004). Statistical simulations of asteroids' orbital evolution indicated that more than 60% of NEAs came from the inner main belt (Bottke et al., 2002; Morbidelli and Vokrouhlický, 2003). Especially, the ν_6 secular resonance with Saturn is located in the inner end of the main belt (around $\sim$ 2 AU of semi-major axis and $\sim$ 20° of orbital inclination). This escape hatch is close to the near-Earth orbits, and more importantly the hatch has no source to supply asteroids into itself on the inward side. In terms of the relationship between the directions of asteroids' rotation and the Yarkovsky-driven migration, the only sources that can enter the ν_6 resonance from the outside are retrograde spinning asteroids.

1.4 Dissertation Overview

As well as sustained efforts of ground-based observations, several spacecraft missions have revealed rocky worlds of asteroids. We have already entered a new phase to understand details of geophysical processes by means of close-up imagery

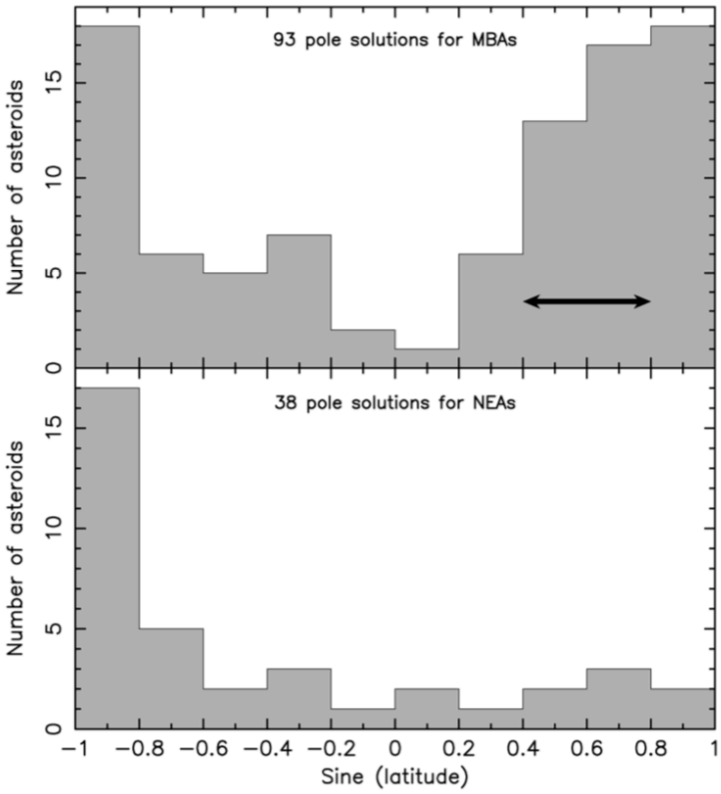

Figure 1.8: Distributions of spin pole latitudes with respect to the ecliptic plane among near-Earth asteroids (NEAs) and main belt asteroids (MBAs) (Vokrouhlický et al., 2015). Values of $\sin(\text{latitude}) = -1$ and 1 correspond to retrograde and prograde rotation about perpendicular axes, respectively.

and detailed 3-dimensional shape models. In this thesis, we aim to shed light on dynamical evolution processes of small bodies based on spacecraft data.

Chapter 2: *YORP Effect on Asteroid Ryugu*

Japan's Hayabusa2 spacecraft revealed the nature of asteroid 162173 Ryugu in June 2018. The formation of its spinning top-shape is a key question. In this chapter, we address how thermal-induced torque alters the spin state of Ryugu. We are the first to simulate the YORP effect on Ryugu and the long-term spin history, which can provide a clue to understand the formation and evolution process of the asteroid.

Chapter 3: *Density Distribution Estimation for Small Bodies*

We propose a new approach to make a constraint on internal structures of small bodies based on a relationship between the surface topography and the gravity field. In general, it is difficult to measure the gravity field precisely enough to estimate the internal density distribution. Our technique can be useful even for a target whose gravity is not well measured. We will apply it to asteroid 25143 Itokawa and comet 67P/Churyumov-Gerasimenko and discuss implications for accumulation processes of the rubble pile asteroid and the comet nucleus. The case study on asteroid Itokawa has already been published from Kanamaru and Sasaki (2019) and Kanamaru et al. (2019).

Chapter 2

YORP Effect on Asteroid Ryugu

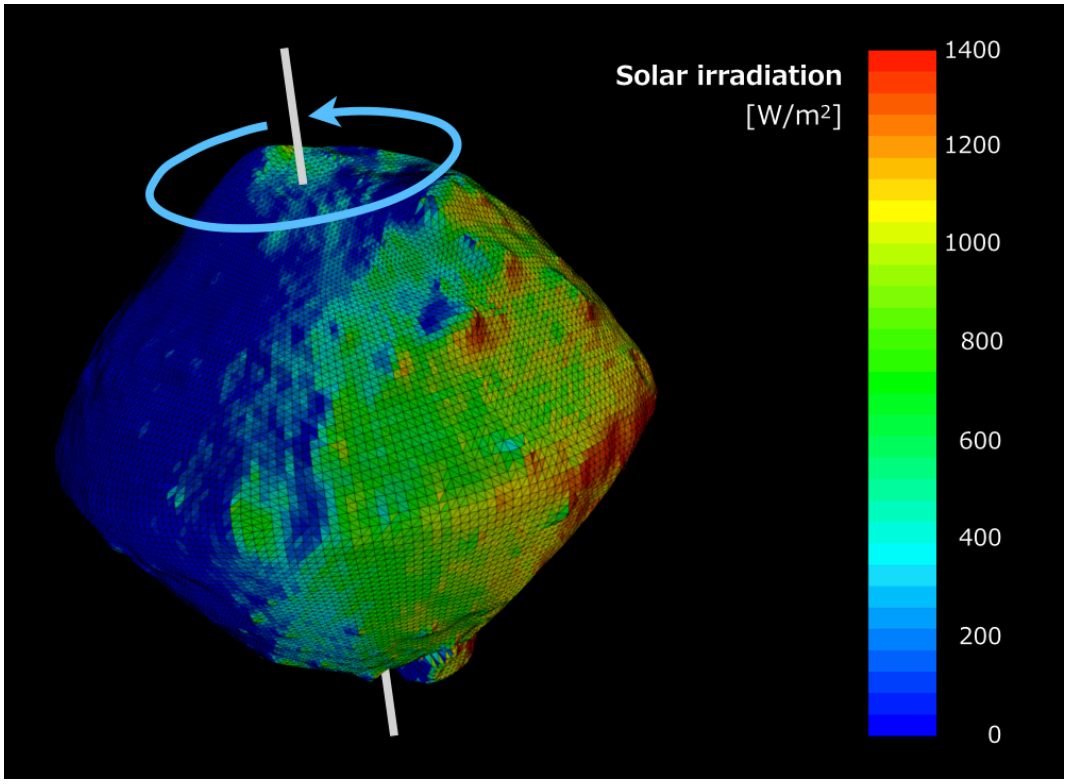

Theory of thermally induced spin alteration of an asteroid (*i.e.* YORP effect) and application to dynamical evolution of asteroid Ryugu.

2.1 Method of YORP Simulation

This section explains a way of modeling the YORP effect on an asteroid and simulating the evolution of the spin state. In order to calculate torque on the body, we need a thermal model to evaluate temperature or energy flux of radiation from the surface of the asteroid (Section 2.1.1). Afterwards, we just have to integrate the equation of motion for the asteroid's rotation according to the thermal torque varying from moment to moment.

2.1.1 Thermal model

We begin with the energy conservation law at each surface element of a small body's shape. The following thermal diffusion equation presents the balance between the incident energy from the sunlight (the left hand side) and a sum of energy derived from thermal re-radiation from the surface element and heat conduction into the ground (the right hand side).

$$(1 - A)\Phi(\hat{\boldsymbol{n}}_i \cdot \hat{\boldsymbol{r}}_{sun}) = \epsilon\sigma T_i^4 + K\hat{\boldsymbol{n}}_i \cdot \nabla T_i \tag{2.1}$$

where A is albedo of the surface, which is treated as a constant regardless of places and time. Φ denotes solar irradiation or energy flux of the sunlight per unit area depending on the heliocentric distance of the asteroid. In this study, we calculated the energy flux $\Phi(t)$ in each time step based on the Kepler motion of the asteroid

around the Sun.

$$\Phi(t) = \Phi_{Earth} \left(\frac{r_{Earth}}{r_{body}(t)} \right)^2 \tag{2.2}$$

The solar irradiation at the Earth's orbit $r_{Earth} = 1\mathrm{AU}$ is called as the solar constant Φ_{Earth} and it decreases inversely proportional to the square of the body's distance from the Sun. It makes a great influence on strength or time scale of the YORP effect depending on an orbital semi-major axis and eccentricity. For example, there is a difference in the energy flux in about six times between the Near-Earth orbit ($\sim$ 1 AU) and the inner main belt ($\sim$ 2.5 AU). A Near-Earth asteroid would have seasonal variation in the solar irradiation in a few times because of its eccentric orbit. We used 1366.0 $\mathrm{W/m^2}$ for the solar constant in our simulations.

Consequently, the left hand side of Equation 2.1 expresses the amount of the solar energy absorbed by the ith surface element of a normal vector $\hat{\boldsymbol{n}}_i$. A normalized vector $\hat{\boldsymbol{r}}_{sun}$ indicates the direction of the Sun in the asteroid-fixed coordinate frame whose origin is located on the asteroid's center. Therefore, the factor $(\hat{\boldsymbol{n}}_i \cdot \hat{\boldsymbol{r}}_{sun})$ means a fraction of the input energy to the solar irradiation depending on the degree of the element's tilt. In the opposite side of the Sun's direction or the night side of the body, this factor becomes negative and the solar irradiation is supposed to be turned off in our simulations.

In the right hand side of Equation 2.1, the emission term includes emissivity ϵ of the body, the Stefan-Boltzmann constant σ and temperature T_i of the ith surface element. The second term represents the heat flux from the surface element into

the body's interior. K denotes thermal conductivity of the material. Some authors implemented 1-dimensional thermophysical modelling to evaluate the surface temperature concurrently with computation of thermal torque on the body as stated below (e.g. Čapek and Vokrouhlický (2004)). Combination of these models would be computationally costly for the spin alteration in a longer time scale.

The Rubincam (2000) model has been widely used to simplify the thermal equilibrium equation shown in Equation 2.1 for the YORP modeling. Rubincam (2000) assumed (1) zero-conductivity and (2) Lambert radiation from each surface element. According to the former assumption, we can neglect the conduction term in Equation 2.1 as follows.

$$(1 - A)\Phi(\hat{\boldsymbol{n}}_i \cdot \hat{\boldsymbol{r}}_{sun}) \approx \epsilon\sigma T_i^4 \tag{2.3}$$

This equation means that the incident energy from the sunlight is immediately emitted from the surface with no time lag. This assumption allows us to easily determine the surface temperature of the body from the amount of the incident energy.

Moreover, the Lambert surface isotropically reflects or radiates light, where the same intensity of emission is observed from any angle. The Lambert radiation assumption results in a simple formula to represent a force working on each surface

element (Rubincam, 2000; Vokrouhlický and Čapek, 2002).

$$d\boldsymbol{f}_i = -\frac{2}{3}\frac{\epsilon\sigma T^4}{c}\hat{\boldsymbol{n}}_i dS_i \tag{2.4}$$

$$= -\frac{2\Phi}{3c}(\hat{\boldsymbol{n}}_i \cdot \hat{\boldsymbol{r}}_{sun})\hat{\boldsymbol{n}}_i dS_i \tag{2.5}$$

where c is speed of light. The thermal "kick-back" force directs opposite along the surface normal $\hat{\boldsymbol{n}}_i$ and it is proportional to the area of the element, dS_i. In the above equation, we converted the factor $(1 - A)$ to 1 in order to combine the effects of scattering on the surface and thermal re-radiation. If the scattered light reflects isotropically on the Lambert surface, we can add the same expression with the thermal radiation with the factor of albedo A.

Then, we can compute the net torque $\boldsymbol{\tau}$ of the YORP effect by integrating the above force over the entire surface of the asteroid.

$$\boldsymbol{\tau} = \int_S \boldsymbol{r} \times d\boldsymbol{f} = \sum_{i=1}^{N_S} \boldsymbol{r}_i \times d\boldsymbol{f}_i \tag{2.6}$$

where $\boldsymbol{r}$ and $\boldsymbol{r}_i$ are centroid position vectors of surface elements. Given a polyhedral shape model covered with N_S triangular surface meshes, we just have to sum torque on every surface element as a cross product of the element's position $\boldsymbol{r}_i$ and the thermal kick-back $d\boldsymbol{f}_i$.

2.1.2 Equation of motion

Given a body rotating around the shortest axis, angular momentum $\vec{L}$ is expressed by the moment of inertia C and a spin vector.

$$\boldsymbol{L} = C\omega\hat{\boldsymbol{s}} \tag{2.7}$$

where the spin vector is here separated into a normal vector $\hat{\boldsymbol{s}}$ to indicate the direction of the spin pole and angular velocity of the rotation ω. When we think about an arbitrary rotation, the moment of inertia should be expressed as an inertia tensor I of 3×3 dimensions. Many authors has assumed a uniform rotation for the YORP modeling by neglecting components of the inertia tensor other than the (z, z) component (e.g. Bottke et al. (2006)). It means that the angular momentum vector $\boldsymbol{L}$ and the normal spin vector $\hat{\boldsymbol{s}}$ always faces in the same direction. Given a long time scale of the spin alteration by the YORP effect ($\sim$ millions of years), the rotation pole is quickly relaxed to the shortest axis by external torque from the gravity of the Sun or major planets. In this study, we made this assumption of the uniform rotation.

The YORP torque $\boldsymbol{\tau}$ as stated in the previous section changes the angular momentum of the asteroid. The equation of motion (EOM) for the body's rotation is expressed as follows.

$$\frac{d\boldsymbol{L}}{dt} = \boldsymbol{\tau} \tag{2.8}$$

We can combine the above EOM with Equation 2.7 and decompose it into the components parallel/perpendicular to the spin pole $\hat{\boldsymbol{s}}$.

$$\frac{d}{dt}(C\omega\hat{\boldsymbol{s}}) = C\frac{d\omega}{dt}\hat{\boldsymbol{s}} + C\omega\frac{d\hat{\boldsymbol{s}}}{dt} = (\boldsymbol{\tau}\cdot\hat{\boldsymbol{s}})\hat{\boldsymbol{s}} + \left[\boldsymbol{\tau} - (\boldsymbol{\tau}\cdot\hat{\boldsymbol{s}})\hat{\boldsymbol{s}}\right] \tag{2.9}$$

Then, we obtain each component.

$$\frac{d\omega}{dt} = \frac{\boldsymbol{\tau}\cdot\hat{\boldsymbol{s}}}{C} \tag{2.10}$$

$$\frac{d\hat{\boldsymbol{s}}}{dt} = \frac{\boldsymbol{\tau} - (\boldsymbol{\tau}\cdot\hat{\boldsymbol{s}})\hat{\boldsymbol{s}}}{C\omega} \tag{2.11}$$

The first component along the spin pole changes the spin rate ω. If this term is positive, the YORP torque accelerates the body's rotation, and vice versa. The second one perpendicular to the spin pole changes its orientation. For convenience, Bottke et al. (2006) decomposed this term of the spin pole orientation into another two parts, thus:

$$\frac{d\omega}{dt} = \frac{\tau_\omega}{C} \tag{2.12}$$

$$\frac{d\varepsilon}{dt} = \frac{\tau_\varepsilon}{C\omega} \tag{2.13}$$

$$\frac{d\psi}{dt} = \frac{\tau_\psi}{C\omega} \tag{2.14}$$

where the first term indicates a change of the spin rate as with Equation 2.10. The second and third indicate a component which changes obliquity of the spin pole and

a component which induces precession, respectively. The obliquity (or the axial tilt) ε is the angle between the spin normal vector $\hat{\boldsymbol{s}}$ and a normal vector $\hat{\boldsymbol{N}}$ to the orbital plane. The spin pole could be tumbling because of the thermal torque in precession longitude ψ. Each component of the YORP torque $\boldsymbol{\tau}(\tau_\omega, \tau_\varepsilon, \tau_\psi)$ can be defined as follows:

$$\tau_\omega \equiv \boldsymbol{\tau} \cdot \hat{\boldsymbol{s}} \tag{2.15}$$

$$\tau_\varepsilon \equiv \boldsymbol{\tau} \cdot \hat{\boldsymbol{e}}_{\perp 1} \tag{2.16}$$

$$\tau_\psi \equiv \boldsymbol{\tau} \cdot \hat{\boldsymbol{e}}_{\perp 2} \tag{2.17}$$

where two kinds of unit vectors perpendicular to the spin pole, $\hat{\boldsymbol{e}}_{\perp 1}$ and $\hat{\boldsymbol{e}}_{\perp 2}$ are defined as follows (Bottke et al., 2006):

$$\hat{\boldsymbol{e}}_{\perp 1} \equiv \frac{(\hat{\boldsymbol{N}} \cdot \hat{\boldsymbol{s}})\hat{\boldsymbol{s}} - \hat{\boldsymbol{N}}}{\sin \varepsilon} \tag{2.18}$$

$$\hat{\boldsymbol{e}}_{\perp 2} \equiv \frac{\hat{\boldsymbol{s}} \times \hat{\boldsymbol{N}}}{\sin \varepsilon} \tag{2.19}$$

Figure 2.1 illustrates these base vectors of the coordinate system to express the spin state of the asteroid.

Finally, the magnitude of the YORP effect is often characterized by a time scale for the thermal torque τ to double or halve the angular velocity ω of the rotating asteroid, that is, the so-called YORP time scale (Rubincam, 2000). The time scale of spin-up/down can be expressed by the torque component parallel to the spin axis

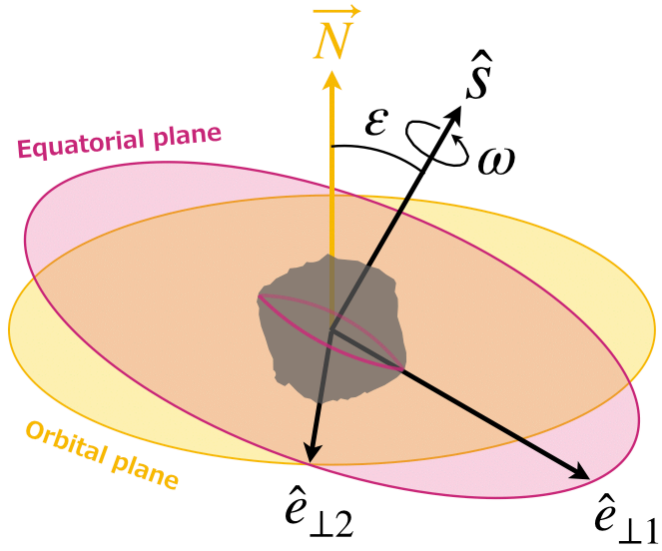

Figure 2.1: Definition of the spin unit vectors.

according to Equation 2.12.

$$t_{\text{double}} = \frac{\omega}{\left|\frac{d\omega}{dt}\right|} = \frac{C\omega}{|\tau_\omega|} \quad (\text{when spinning-up; } \tau_\omega > 0) \tag{2.20}$$

$$t_{\text{halve}} = \frac{\omega/2}{\left|\frac{d\omega}{dt}\right|} = \frac{C\omega}{2\,|\tau_\omega|} \quad (\text{when spinning-down; } \tau_\omega < 0) \tag{2.21}$$

If the spin rate ω is increasing ($\frac{d\omega}{dt} > 0$ or $\tau_\omega > 0$), ω will increase twofold in the time scale of t_{double} (or it will halve the rotation period $P = 2\pi/\omega$). If the spin rate is decreasing, the reverse will happen in the time scale of t_{halve}. Moreover, the magnitude of the YORP effect on the asteroid can be easily scaled by its orbit, size R and bulk density ρ. The solar irradiation attenuates with an inverse squared distance from the Sun as described in Equation 2.2. The magnitude of the YORP effect decreases with R^{-2} dependence on the body's size. That's because the thermal torque becomes stronger as the size of the asteroid increases with dependence of

$R^2 \times R$ (the surface area and length of the lever arm), while the moment of inertia increases more rapidly by $R^3 \times R^2$ (mass and radius from the axis) (Rubincam, 2000). The higher bulk density of the body, the smaller YORP effect by ρ^{-1} dependence.

2.2 Asteroid Ryugu as Revealed by Hayabusa2

Japan's Hayabusa2 is a sample return mission from a C-type Near-Earth asteroid, 162173 (1999 JU_3) Ryugu (Tachibana et al., 2014; Tsuda et al., 2019; Watanabe et al., 2017). The Hayabusa2 spacecraft arrived at the target asteroid in June 2018 and started homeward to the Earth in November 2019 after about 17 months of the asteroid-proximity phase, including successes of two touchdowns for sampling the surface material, an artificial cratering experiment and deployment of rovers. Hayabusa2 revealed the nature of the rocky surface and its spinning top shape (Watanabe et al., 2019). The top-shaped body has an elevated ridge in the equatorial region and a flat cross section in comparison with a spherical or ellipsoidal object. The Ryugu's shape is considered to be a result of rotationally induced deformation in the past (Watanabe et al., 2019). According to the finite element method (FEM) analysis by Hirabayashi et al. (2019), a fast rotation at a period of about 3.0–3.5 hours is enough to induce structural failure in the interior or mass wasting on the surface by the centrifugal force. However, the spin-down process from the past fast rotation to the current mild state (7.6 hours period) still remains unknown. The goal of this section is to shed light on the YORP effect responsible for the dynamical

evolution of Ryugu on comparison of its time scale with the geological age.

We hereby address a brief review of the initial achievement of the Hayabusa2 mission. Watanabe et al. (2019) is a flagship report on the first impression of Ryugu such as the spinning top shape as mentioned above. For our later simulations, we utilized the orbital elements, rotation period, spin pole orientation and other physical properties of Ryugu released with this paper (See Table A.3). Ryugu is spinning at a period of 7.63 hours, and the right ascension (RA) and declination (Dec) of the spin pole are respectively $\alpha = 96.40°$ and $\gamma = -66.40°$ on the Earth's equatorial plane in the J2000.0 frame. This pole orientation corresponds to $\lambda = 179.3°$ and $\beta = -87.44°$ in longitude and latitude on the reference plane of the ecliptic. From these parameters of the orbit and spin, the obliquity ε, or the tilt angle of the spin pole on reference of the Ryugu's own orbital plane, can be calculated as $171.6°$. Ryugu is a retrograde rotator with the pole nearly perpendicular to the orbital plane.

3-dimensional shape models of Ryugu were constructed from images of the onboard Optical Navigation Camera-Telescopic (ONC-T) and have been updated until the time of writing. In the Hayabusa2 project, two different methods are used for the 3D shape reconstruction: stereo-photoclinometry (SPC) (Gaskell et al., 2006, 2008) and Structure-from-Motion (SfM) (Szeliski, 2011) (See Table B.4). Ryugu's volume derived from the above shape model and mass from spacecraft tracking data during a descent operation to the asteroid yielded a bulk density of $1{,}190 \pm 20\,\mathrm{kg/m^3}$ (Watanabe et al., 2019). Ryugu's typical reflectance from visible to near-infrared wavelength shows very flat spectra and a low geometric albedo of $4.5 \pm 0.2\%$ at

0.55 μm band (Kitazato et al., 2019; Sugita et al., 2019). This reflectance spectra can be classified as Cb-type in the Bus taxonomy (Bus and Binzel, 2002b). Weak absorption at 2.72 μm was detected throughout the whole surface and these features suggest that Ryugu is composed of CM- or CI-like materials such as heated Ivuna meteorite (Kitazato et al., 2019). Since the bulk density of Ryugu is smaller than many types of carbonaceous chondrites, the porosity of Ryugu could reach more than 50% (Watanabe et al., 2019).

Sugita et al. (2019) summarized overall features on Ryugu in geomorphology. It was found from global mapping by ONC that the surface of Ryugu had faint color variation in spectral slope between b- and x-band (480-860 μm). The spatial distribution of the b-x spectral slope is correlated with distribution of geo-potential (or elevation). Areas of high potentials such as the polar and equatorial regions tend to have smaller or negative slopes (i.e. bluer spectra). On the other hand, the mid-latitude areas of Ryugu have redder spectra with steeper slope. This color variation suggests that materials weathered on the surface are migrating from highlands to lowlands in response to the current shape and the gravity field of Ryugu (Sugita et al., 2019).

Crater statistics are indicators of surface age of a solid body and mechanical properties of the surface layer. (Hirata et al., 2020) provided a comprehensive list of impact craters on Ryugu and discussed their spatial distribution. 77 craters larger than 10 meters in diameter were identified and another 9 candidates with less confidence were classified into non-crater features. A statistical randomness

analysis by (Hirata et al., 2020) confirmed that those craters were concentrated on the equatorial region (30°S – 30°N) rather than a random distribution. Moreover, number density of the craters has longitudinal variation. The so-called western bulge (160°E – 290°E) has less craters than regions around the prime meridian of Ryugu (300°E – 30°E). An origin of the western bulge is proposed as a deformation process of Ryugu during a period of fast rotation (Hirabayashi et al., 2019) or regolith landslides towards the western side at a rapid spin in the past (Scheeres, 2015). These processes could resurface the western hemisphere of Ryugu and result in the east-west dichotomy in crater density. Papers on the craters' depth-to-diameter ratios and morphological analyses are to be published sooner or later (Noguchi et al. in revision and Cho et al. in prep., respectively). Given unconsolidated surface materials, a surface age of Ryugu was estimated as 8.9 ± 2.5 Ma in Sugita et al. (2019). More detailed statistics with close-up images are planned to be appear shortly (Morota et al. in revision). In Section 2.4, we will compare the surface age with a time scale of evolution of Ryugu's spin state induced by the YORP effect.

2.3 Thermal Net Torque on Ryugu

For YORP modeling of asteroid Ryugu, we utilized the orbital elements, spin pole orientation and rotation period published by Watanabe et al. (2019) (See Table A.3). During a cycle of the revolution, we simulated the direction of the Sun in the asteroid-fixed frame and evaluated the thermal torque $\boldsymbol{\tau}$ at every time step. The each

time step of this simulation was fixed to about 382 seconds, corresponding to the spin phase of 5 degrees. Therefore, we divided the rotation period of 7.63262 hours into equal 72 steps and put the time step forward until the asteroid revolves around the Sun in approximately 474 Earth-days. The orbital period of Ryugu corresponded to about 1490.1 cycles of the rotation[1] and the total number of the time steps was 107,288.

The YORP torque $\boldsymbol{\tau}$ was transformed from the body-fixed frame to the orbital plane frame, where the x-y plane lies in the orbital plane, the Sun is located in the origin and the x-axis is in the direction of the periapsis. Then, Equations 2.15 to 2.17 allow us to obtain the three components $(\tau_\omega, \tau_\varepsilon, \tau_\psi)$, affecting the spin rate ω, the obliquity ε (angle of axial tilt) and the longitude of precession ψ, respectively (See also Figure 2.1).

The 3-dimensional shape models used for later simulation and analysis are listed in Table B.4. We hereby show the results of the latest version model released on August 2 in 2019, which is constructed by the shape model team of Hayabusa2 project using the stereo-photoclinometry (SPC) software (Watanabe et al., 2019). The number of the surface triangular meshes is 49,152. In Section 2.5, we will discuss differences in resultant YORP effects derived from the two methods of 3D shape reconstruction (SPC and Structure-from-Motion (SfM)), versions and

[1] In our simulation, the rotation phase is not identical with the initial state when the asteroid comes back in the starting point of the orbit. Since the daily variation in torque is much greater than the year-averaged net torque, the phase overrun may possibly change the resultant YORP effect. Given various initial phase offsets to Ryugu's spin state, we calculated the net torque and compared each others. As a result, the standard deviation of the net torque with different phase offsets was at most 5×10^{-4} [N $\cdot$ m]. At least, the first three digits of the data are free from this uncertainty.

resolution of the shape models.

Figures 2.2 and 2.3 present time variation in the three torque components over cycles of the rotation and revolution since 2018 July 1.0 TDB (barycentric dynamical time), respectively. The magnitude of the three components are comparable with each others and the values are fluctuating from negative to positive during daily and annual cycles. The seasonal variation in YORP effect is derived from the change of the heliocentric distance because of the eccentric orbit (Eccentricity $e = 0.1903$) and the obliquity of the spin pole (Obliquity $\varepsilon = 171.64$). For example, torque around the spin axis of $\tau_\omega = 10$ [N $\cdot$ m] corresponds to pushing the equator of Ryugu in the tangential direction with about 2 grams-force (under the Earth's gravity circumstance). Since the time variation in torque is not fully cancelled over the annual cycle, the residual torque induces a secular change in the spin state of the asteroid.

We computed net torque $\bar{\boldsymbol{\tau}}(\bar{\tau}_\omega, \bar{\tau}_\varepsilon, \bar{\tau}_\psi)$ by averaging the above time variation in thermal torque over the cycle of the revolution. In the nominal case of the SPC-based 49k model (ver. 2019-08-02), the year-averaged torque resulted in $(\bar{\tau}_\omega, \bar{\tau}_\varepsilon, \bar{\tau}_\psi) = (-0.1254, 0.1179, 4.179)$ [N $\cdot$ m] (Table 2.1). The negative value of the ω-related component implies that Ryugu is currently decreasing the angular velocity or spinning down. Changes in the spin rate and the obliquity of Ryugu induced by the net torque corresponds to $\Delta\omega = -0.005609$ [deg/sec] and $\Delta\varepsilon = 23.07$ [deg] per million years, respectively. According to Equation 2.21, a time scale of spin down corresponds to $t_{\rm halve} = 1.168$ million years.

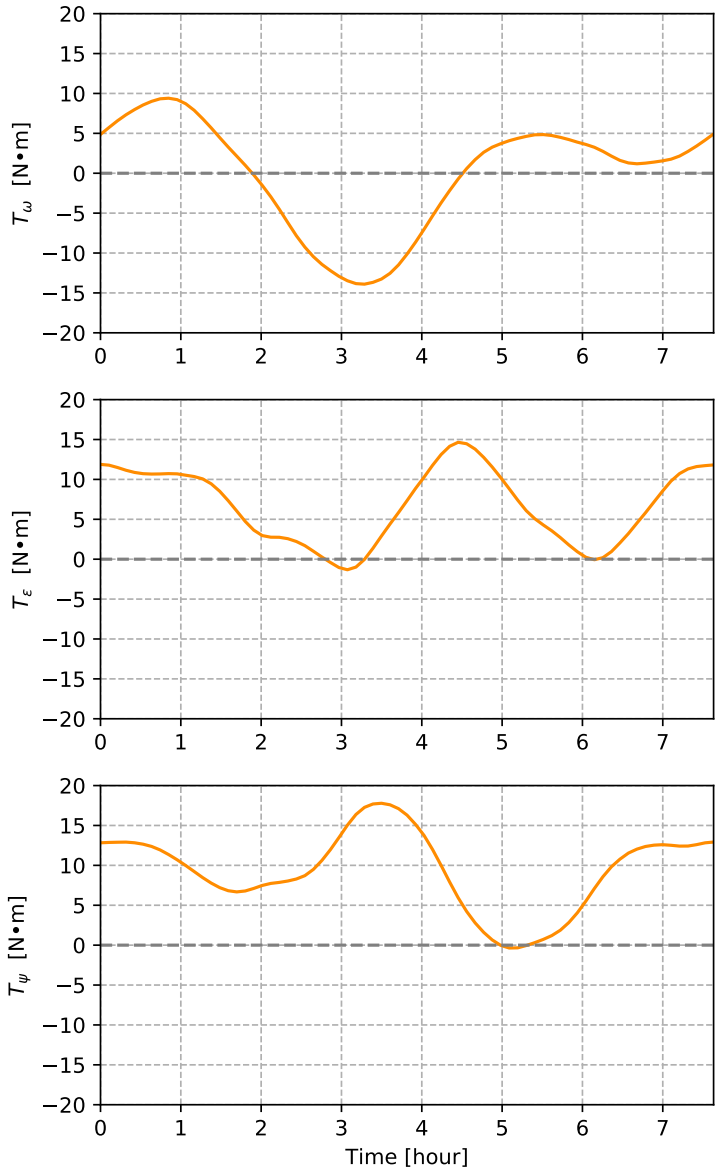

Figure 2.2: Time variation in the thermal torque over a cycle of the rotation (Ryugu's rotation period $P \sim 7.6$ hours). Three panels indicate the each component of the torque as function of time in hour: (*upper*) the component parallel to the spin pole τ_ω increasing or decreasing the spin rate, (*middle*) the component tilting the spin pole τ_ε, and (*bottom*) the component exciting the precession. The 3D shape model of Ryugu used in this simulation was the SPC-based model of 49,152 meshes released on August 2 in 2019.

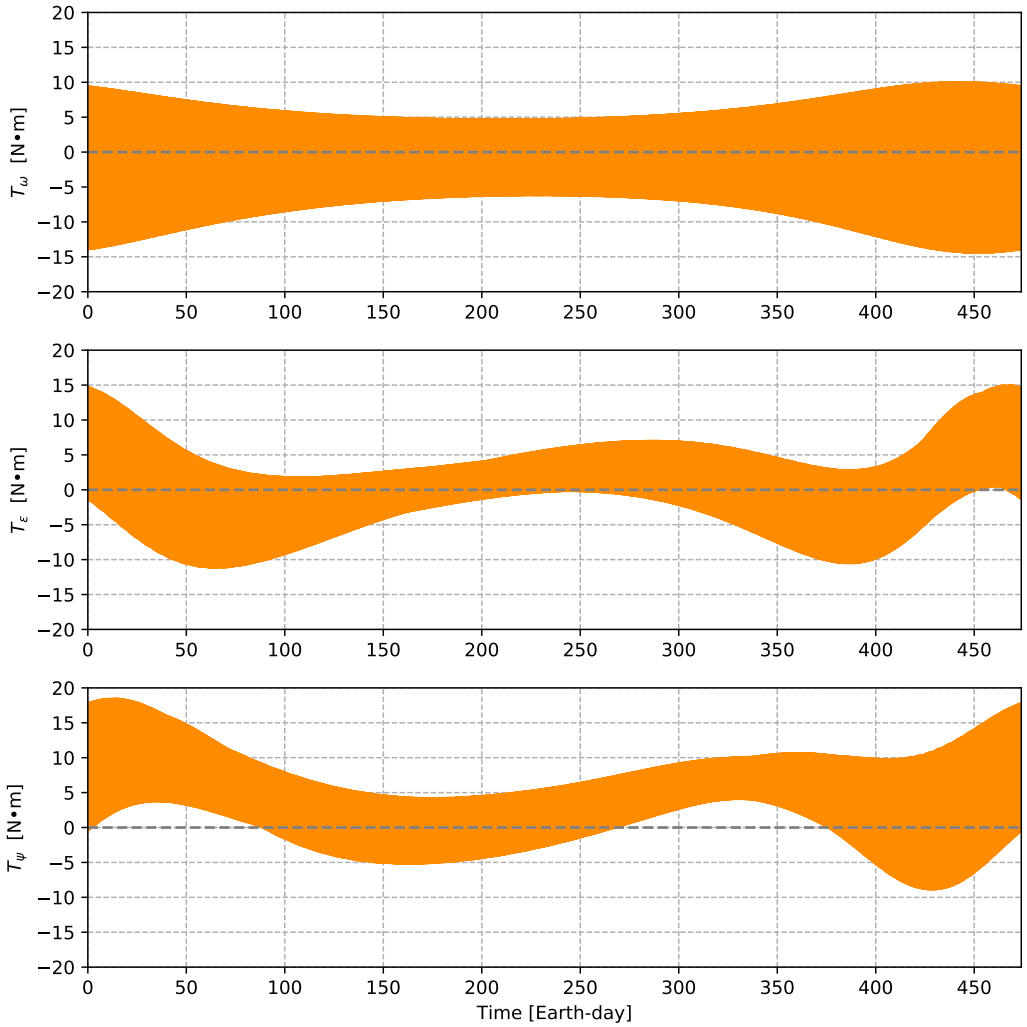

Figure 2.3: Seasonal variation in the components of the YORP torque $\boldsymbol{\tau}(\tau_\omega, \tau_\varepsilon, \tau_\psi)$ over a cycle of the revolution (Orbital period of Ryugu $\sim$ 474 Earth-days). The same SPC model with Figure 2.2 was used in this simulation.

Table 2.1: Year-averaged net torque $\bar{\boldsymbol{\tau}}(\bar{\tau}_\omega,\ \bar{\tau}_\varepsilon,\ \bar{\tau}_\psi)$ and corresponding increase/decrease in the spin parameters per million years $(\Delta\omega, \Delta\varepsilon, \Delta\psi)$ for the nominal shape model (SPC-based 49k model released on 2019-08-02).

$\bar{\tau}_\omega$ [N · m]	$\bar{\tau}_\varepsilon$ [N · m]	$\bar{\tau}_\psi$ [N · m]
-0.1254	0.1179	4.179
$\Delta\omega$ [deg/sec/Myr]	$\Delta\varepsilon$ [deg/Myr]	$\Delta\psi$ [deg/Myr]
-0.005609	23.07	817.4
Time scale of spin-down, t_{halve} [Myr]		
1.168		

2.4 Long-Term Spin Evolution of Ryugu

2.4.1 YORP-induced evolution

The spin rate ω (or period $P = 2\pi/\omega$) and the obliquity ε are essential parameters for simulating long-term evolution of Ryugu's spin state. We hereby demonstrate dependence of the YORP effect on these parameters and spin modification in millions of years. As the obliquity of the spin pole changes, variable sunshine conditions change the net torque over a cycle of revolution. Figure 2.4 shows rates of change in ω (dashed) and ε (solid) per million years as functions of ε in a manner of some previous studies (Bottke et al., 2006; Čapek and Vokrouhlický, 2004; Rubincam, 2000; Vokrouhlický and Čapek, 2002). You should note that the solid curve of $d\varepsilon/dt$ has three "asymptotic" nodes at $\varepsilon = 0°$, $90°$ and $180°$. The thermal torque works asymptotically towards one of these nodes depending on initial obliquity ε_0. In this case of the nominal shape model, boundaries at $\varepsilon = 36°$ and $144°$ dominate

destiny of spin evolution, whether the spin pole finally stands erect ($\varepsilon \to 0°$ or $180°$) or falls sideways on the orbital plane ($\varepsilon \to 90°$). The vertical dashed line in Figure 2.4 represents the current obliquity of Ryugu ($\varepsilon = 171.64°$), which was observed by Hayabusa2 (Watanabe et al., 2019). Given the observed shape, it is necessary for Ryugu to start with obliquity more than $144°$ in order to reach the current value since this range has positive rates of change in obliquity. Otherwise, if $36° < \varepsilon_0 < 144°$, the spin pole will fall onto the orbital plane and oscillate around $\varepsilon = 90°$. Given an initial obliquity smaller than $36°$, the YORP effect will set up the spin pole towards zero obliquity. On the other hand, the spin rate ω of the asteroid increases or decreases depending on obliquity at each occasion. The dashed line in Figure 2.4 shows that Ryugu decelerates its rotation at the three asymptotic states. Based on the ε-dependence of the YORP effect, Ryugu is considered to be currently in a spin-down phase with the obliquity approaching $180°$ in contrast to asteroid 101955 Bennu (i.e. a target body of NASA's OSIRIS-REx mission), which is accelerating its spin with obliquity of nearly $180°$ (Hergenrother et al., 2019; Nolan et al., 2019).

Nextly, we simulated evolution of Ryugu's spin state over millions of years. Figure 2.5 shows a change of the spin state in three million years after an initial period P_0 of 7 hours and different initial obliquities ε_0 were given. The upper and lower panels represent respectively the rotation period and the obliquity of the asteroid as functions of time. The nominal spin parameters of Ryugu, $P = 7.63262$ hours and $\varepsilon = 171.64°$ are shown by dashed lines in the panels. As shown in Figure 2.4, given initial obliquity smaller than $144°$, the spin pole falls down onto the orbital

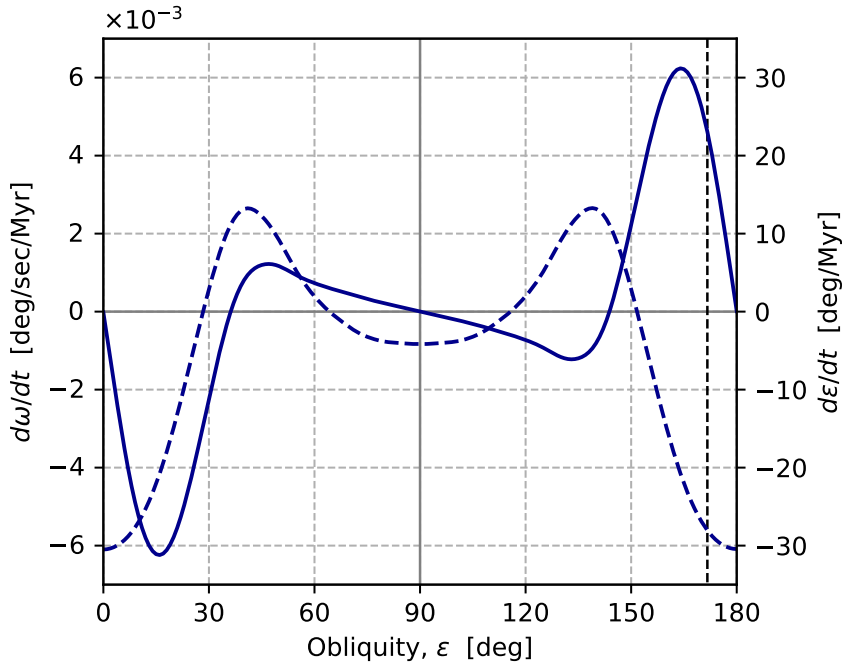

Figure 2.4: Rates of change in the obliquity ε (solid) and the spin rate ω (dashed) as functions of the obliquity. According to Equation 2.13, ε-related torque is hereby converted into the amount of change in ε using the current spin rate of Ryugu. The vertical dashed line presents the nominal obliquity observed by Hayabusa2 ($\varepsilon = 171.64°$).

plane and cannot reach the current spin state of Ryugu (orange and red curves in Figure 2.5). Otherwise, the obliquity will exceed the nominal value in a few million years or less and approach obliquity of 180° in 3 million years at maximum. On the other hand, rotation period tends to reach the nominal value sooner than the obliquity does since the initial period is close to the nominal value and the thermal torque strongly works to decelerate the spin in a large obliquity range. In this case, it is $\varepsilon_0 = 145^\circ$ that can satisfy the current period and obliquity of Ryugu at the same time ($\sim$ 2.3 million years after the initial spin state).

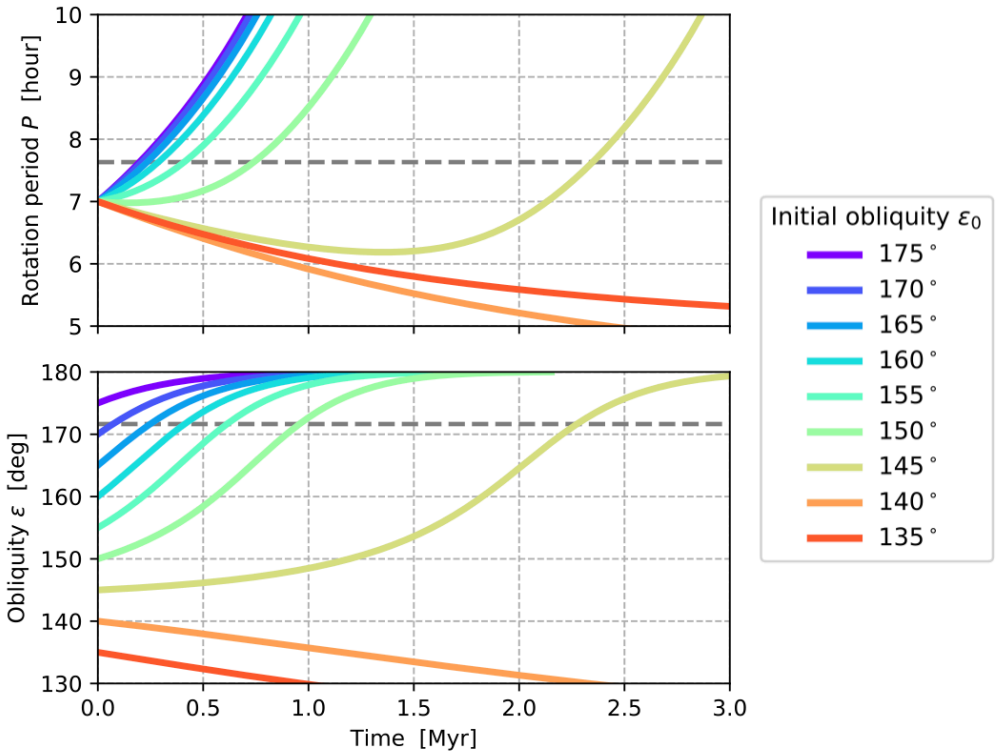

Figure 2.5: The rotation period P (upper) and the obliquity ε (lower) as functions of time based on the nominal shape model. The initial period P_0 is 7 hours in this simulation and curves of different colors present results of different initial obliquity ε_0. The horizontal dashed lines indicate the nominal period and obliquity observed by Hayabusa2.

Moreover, we surveyed various initial conditions for period and obliquity. Figure 2.6 compares profiles with shorter initial periods of 4, 5 and 6 hours. The faster the asteroid was spinning at the beginning of the simulation, the longer time taken to reach the current rotation period of Ryugu. It also takes longer time for obliquity to reach the current value because a rate of change in obliquity becomes smaller at a faster rotation according to Equation 2.13, $\dot{\varepsilon} = \tau_{\varepsilon}/(C\omega)$. For a fast rotation at an initial period of 4 hours, obliquity reach the nominal value before period does unlikely the cases of longer initial periods.

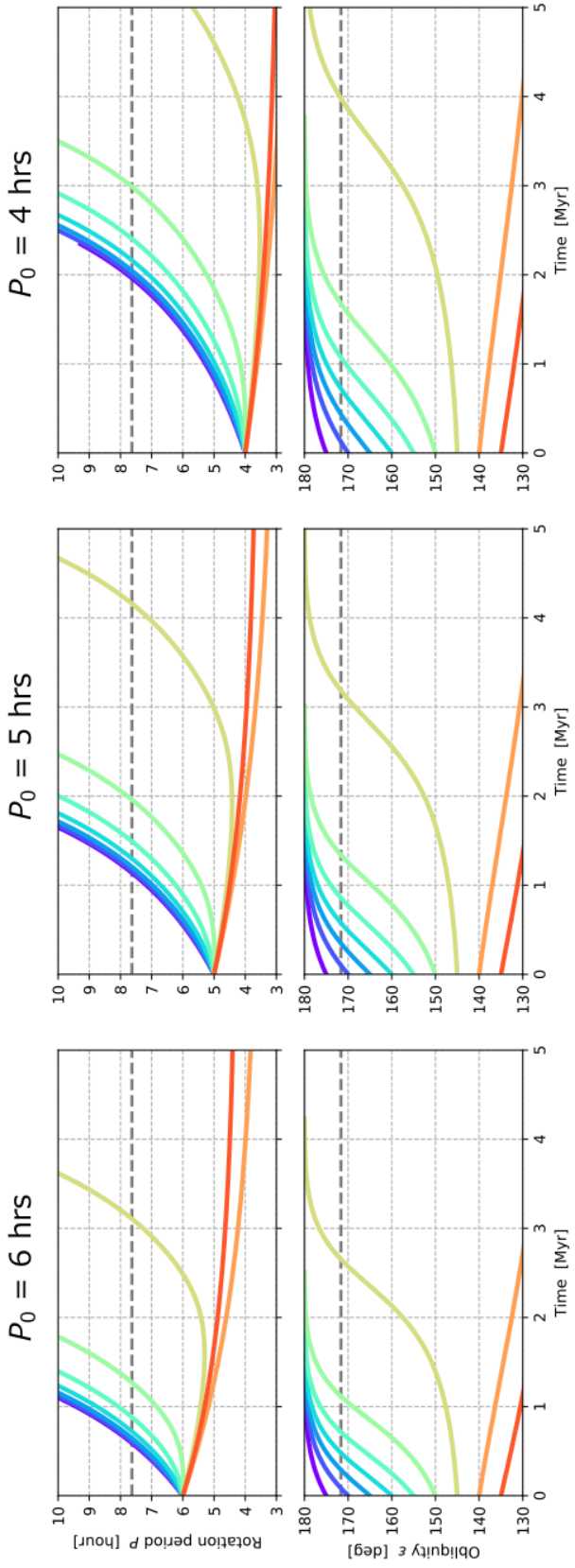

Figure 2.6: Spin evolution of Ryugu similar to Figure 2.5 but comparing between different initial periods.

Figure 2.7 summarizes the above parameter survey in terms of whether the rotation period and obliquity reach the nominal spin state of Ryugu at the same time. The upper panels show time it takes to reach the nominal period on the left (A) and the nominal obliquity on the right (B) as functions of initial spin states. Note that possible solutions to reconcile the two different timings are limited in this parameter space. You can see the signed relative differences between A and B in the lower panel, which means a set of initial conditions (P_0, ε_0) with a value close to zero can reach Ryugu's current state in terms of both period and obliquity. The bold lines divided the cells into positive and negative. A positive value means that a time scale in the panel A is shorter than that of B, that is, the obliquity is not yet enough when the period reaches the nominal value ($P = 7.63$ hours). A negative value means that the obliquity exceed the nominal value ($\varepsilon = 172°$) before the period does. The red cells are the most appropriate conditions for Ryugu's initial spin state to reach the current spin state. These appropriate conditions are located only in initial periods of $P_0 = 6.5$ to 7.5 hours and they correspond to time scales of about 0.25 to 2.3 million years in contrast to the geologic time scale of about 9 million years (Sugita et al., 2019). The parameter survey indicates that the spin state of Ryugu is dynamically "young" during the cycle of the YORP-induced spin alteration, which is still developing into a permanent spin-down phase with obliquity of $\varepsilon = 180°$. In other words, a disturbance of Ryugu's spin must have occurred at least in the last 2.3 million years. We can point out the following three disturbance sources of the angular momentum: (1) kinetic energy of an impactor, (2) topographic change by

crater formation and (3) gravitational torque when Ryugu approached a planet. A close flyby of Earth is a potential event to radically modify the spin state of a near-Earth asteroid (Benson et al., 2019; Scheeres et al., 2000). The spin modification by the gravity of the Earth strongly depends on the hyperbolic orbit and the spin pole direction of the asteroid with respect to the Earth, which are stochastic and unpredictable for the individual target. In the following Sections 2.4.2 and 2.4.3, we evaluate the direct change of Ryugu's angular momentum by a collisional event and the subsequent change in the YORP evolution by the crater formation.

2.4.2 Effect of impacts

An energetic impact will drastically change a spin state of a small body. Since the asteroid experiences multiple impacts during its dynamical lifetime, the spin state has evolved by a combined effect of collisions and YORP (Marzari et al., 2011). Collisions may change the rotation period and the spin pole direction by a stochastic process resembling a random walk, while the YORP effect may alter the spin state systematically during periods between collisional events. For example, given a spherical body with the same mean radius (448 m) and the same bulk density ($1{,}190$ kg/m^3) as Ryugu, a meter-sized impactor may possibly cause a significant change in the spin state of the body. Given that the impactor's radius, density and relative velocity were respectively 3.0 m, 3.0 g/cm^3 and 5.3 km/s (equal to the mean impact velocity in the main belt by Bottke et al. (1994)), we obtained the maximum changes of the rotation period by about -37 minutes or 44 minutes when

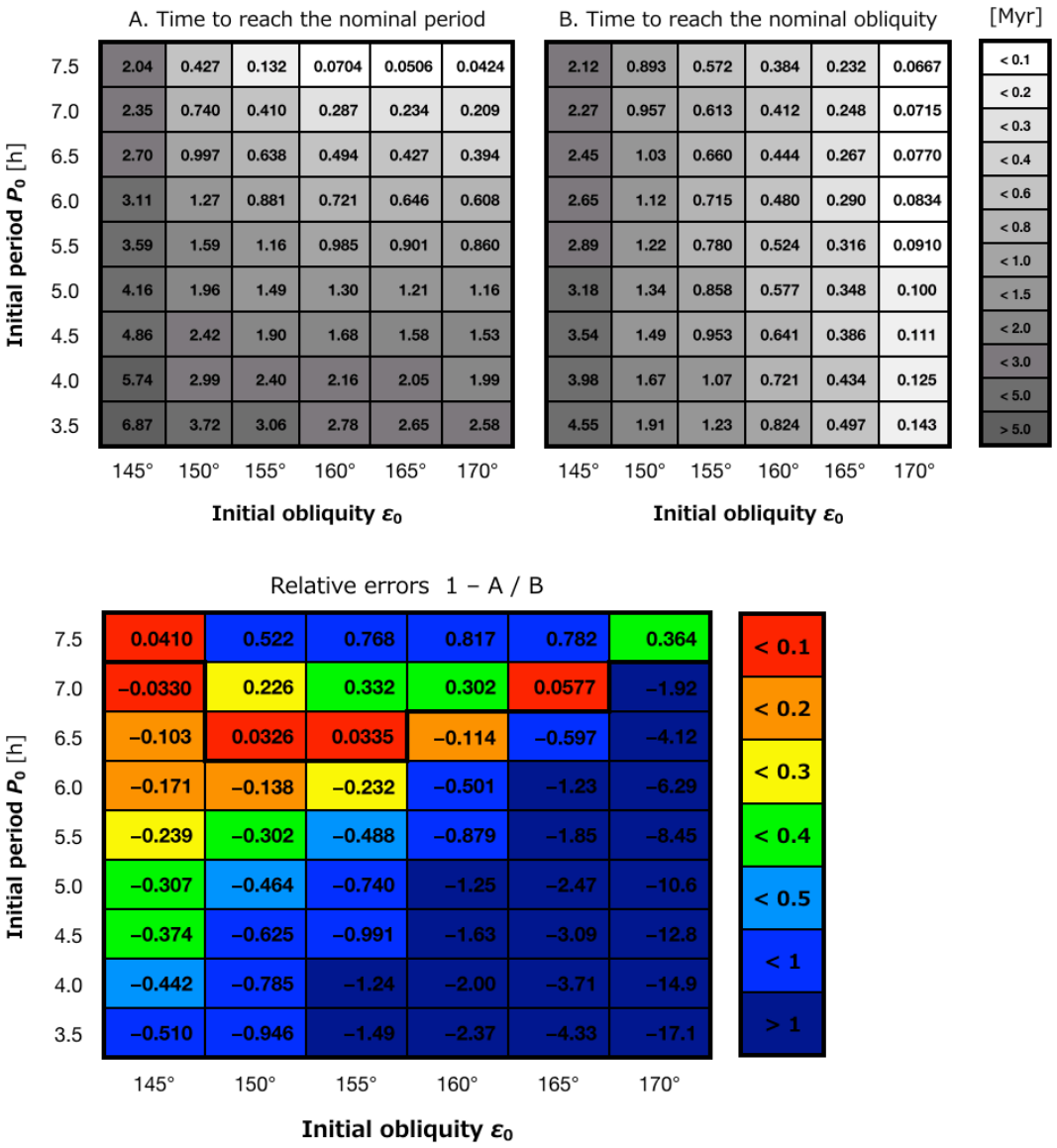

Figure 2.7: Time taken to reach the nominal period of 7.63 hours (A) and the nominal obliquity of $171.6°$ (B) as a function of an initial spin state (P_0, ε_0). Signed relative differences between A and B are shown in the lower panel. The red cells are the most appropriate conditions for Ryugu's initial spin.

the impact resulted in spinning-up or spinning-down the target body depending on the impact site. When the impactor collided at the polar regions of the asteroid, the maximum obliquity change was approximately 5 degrees. Note that energy loss by fragmentation and ejecta escaping from the target body is hereby neglected. We assumed that the angular velocity of the projectile is simply added to that of the target asteroid, as implemented in the Monte Carlo simulation by Marzari et al. (2011). For a smaller projectile with 1 m in radius ($\sim 1.3 \times 10^4$ kg) and the same velocity, the maximum changes of the spin parameters are reduced to about 1.5 minutes in period and 0.2 degrees in obliquity. Furthermore, a projectile with 0.1 m in radius corresponding to ~ 13 kg in mass will mostly not influence the spin state.

On the other hand, Hayabusa2 successfully deployed the Small Carry-on Impactor (SCI) and formed an artificial crater by shooting a copper projectile with 2 kg in mass and 2 km/s in velocity (Arakawa et al., 2017; Saiki et al., 2017). The newly formed crater was about 10 m in diameter and 2 – 3 m in depth. This cratering event can be used as an anchor point for the crater scaling law for Ryugu. In the gravity-dominated regime, where the strength of the surface material is not significant for crater formation, the scaling law for a crater radius R is expressed as follows (Housen and Holsapple, 2011).

$$\pi_R = k_1 \pi_2^{-\frac{\mu}{2+\mu}} \pi_4^{\frac{2+\mu-6\nu}{3(2+\mu)}} \tag{2.22}$$

where k_1 is a constant and $\mu = 0.41$ and $\nu = 1/3$ are given here. The non-

dimensional parameters π_R, π_2 and π_4 are expressed by parameters about the projectile and the target body.

$$\pi_R = R\left(\frac{\rho}{m}\right)^{\frac{1}{3}}, \quad \pi_2 = \frac{ga}{U^2}, \quad \pi_4 = \frac{\rho}{\delta} \tag{2.23}$$

where a, U, δ and m denote the radius, velocity, density and mass of the projectile, respectively. For the SCI impactor, $a = 0.065$ m, $U = 2$ km/s, $\delta = 2.3$ g/cm^3 and $m = 2$ kg were given (Arakawa et al., 2017). The physical parameters of Ryugu were used for the density and the gravity of the target body as $\rho = 1.19$ g/cm^3 and $g = 1.5 \times 10^{-4}$ m/s^2. Using the scaling law in the gravity regime, we estimated the maximum change of the spin state of Ryugu by impact events which resulted in craters of sizes equal to ones currently observed on the asteroid. Table 2.2 chooses 11 craters larger than 100 m in diameter from the catalogue by Hirata et al. (2020) and lists the estimated sizes of the projectiles and the corresponding maximum change of the rotation period and the obliquity. From the above, it is found that the major cratering events on Ryugu has not drastically affected the behavior of the spin evolution of the asteroid. Most cratering events in the equatorial and low latitude areas will not effectively tilt the spin pole. Therefore, it seems that Ryugu has never had any period with the spin pole falling down on the orbital plane since the impact energy cannot set the pole up to the threshold obliquity $\varepsilon = 144°$.

Table 2.2: The estimated maximum change of the spin state (ΔP, $\Delta\varepsilon$) when each major crater (> 100 m in diameter) observed on Ryugu was formed. The impactor's velocity U and density δ were assumed to be 5.3 km/s and 3.0 g/cm^3 for all cases.

ID	Nomenclature	Diameter [m]	Impactor's radius [m]	Max. ΔP [s]	Max. $\Delta\varepsilon$ [°]
1	Urashima	290	0.894	64	0.13
2	Cendrillon	224	0.655	25	0.052
3	Kolobok	221	0.645	24	0.050
4	Momotaro	183	0.514	12	0.025
5	–	173	0.480	9.8	0.020
6	Kintaro	154	0.417	6.4	0.013
7	–	145	0.388	5.2	0.011
8	Brabo	142	0.378	4.8	0.010
9	–	133	0.350	3.8	0.0079
10	Kibidango	131	0.343	3.6	0.0075
11	–	100	0.248	1.4	0.0028
SCI experiment ($U = 2$ km/s, $\delta = 2.3$ g/cm^3 and $m = 2$ kg)					
		~ 10	0.065	0.024	5.1×10^{-5}

2.4.3 Effect of topographic change

As mentioned previously, there is a possibility that small scaled topography will change the secular torque by the YORP effect (Statler, 2009). Over several million years, some impact craters must have been formed on the surface of Ryugu. We compared the nominal shape model with our newly-made models by filling major craters and examined how much effect can be expected by a crater-scaled topographic change. We chose two craters from a low latitude area of Ryugu: #04 Momotaro crater (183 m in diameter) and #10 Kibidango crater (131 m in diameter). Their ID numbers are in accordance with the crater catalog of Ryugu by Hirata et al. (2020). Especially, Kibidango is considered to be a relatively new crater from the viewpoint of its bluer spectrum (Sugita et al. (2019); Morota et al. in review). Using "MeshLab", a software for visualizing and editing 3D mesh data (Cignoni et al., 2008), we removed the surface facets inside the craters and closed the holes with new facets. The nominal shape model and our crater-filled models are illustrated in Figure 2.8. Table 2.3 summarizes the year-averaged thermal torque for each shape model with the current rotation period and obliquity of Ryugu. Changes in the ω-component of the YORP torque can be seen by about 5% and 11%. Note that the re-meshed parts of the shape models are covered with a small number of meshes and the artificial flat surface might bias the thermal torque. In addition, Figure 2.9 compares the original and crater-filled models in terms of the obliquity dependence of the YORP effect. It is found that a single 100-meter-scaled topographic change will not drastically alter the behavior of the YORP-induced spin evolution. In

545 other words, the YORP effect on Ryugu might be dominated by the global scaled anisotropy derived from the 3-dimensional shape.

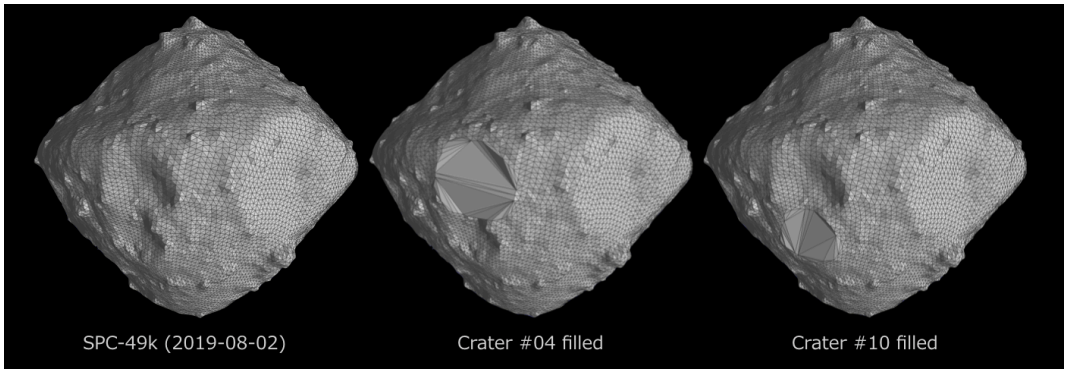

Figure 2.8: The nominal SPC-based 49k model (2019-08-02) and derivative models whose major craters are manually filled.

Table 2.3: A comparison of year-averaged torque between the nominal shape model and derivative models by filling major craters.

Shape model	$\bar{\tau}_\omega$ [N · m]	$\bar{\tau}_\varepsilon$ [N · m]	$\bar{\tau}_\psi$ [N · m]
Nominal shape	-0.1254	0.1179	4.179
Crater #04 filled	-0.1323	0.1199	4.169
Crater #10 filled	-0.1405	0.1205	4.172

2.5 Comparison with Different Shape Models

We demonstrated the YORP simulation using the two types of the shape model families, that is, the SPC- and SfM-based models. The net YORP torque derived from each model is summarized in Tables 2.4 and 2.5. We also compare different

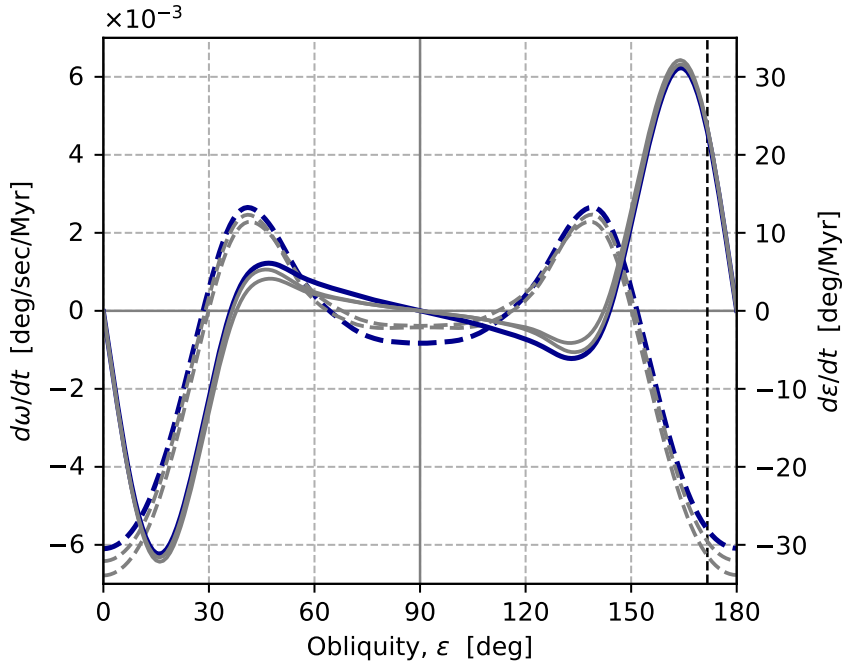

Figure 2.9: The nominal YORP effect (blue) in comparison with the crater-filling experiments (grey).

versions of the shape models between the latest versions released in 2019 and the initial products after the first global observation campaign by Hayabusa2 in summer 2018. Tables 2.4 and 2.5 also include the rate of change of the spin parameters per million years $(\Delta\omega, \Delta\varepsilon, \Delta\psi)$ and the corresponding time scales for the thermal torque to accelerate or decelerate the angular velocity of Ryugu (t_{double} or t_{halve}). Except for the early SPC model, the YORP effect decelerates the rotation of Ryugu in time scales of 0.3 to 2 million years. Though the shape models agree with each others within a meter scale (Watanabe et al., 2019), it turned out that the resultant torque can vary depending on the input models.

Table 2.4: Year-averaged YORP torque $\bar{\boldsymbol{\tau}}(\bar{\tau}_\omega,\ \bar{\tau}_\varepsilon,\ \bar{\tau}_\psi)$ on the SPC-based shape models of different numbers of surface meshes N_S. $\Delta\omega$, $\Delta\varepsilon$ and $\Delta\psi$ represent the rate of change of the angular velocity, obliquity and longitude of precession per million years, respectively. t_{double} or t_{halve} denotes the corresponding time scales of spin-up/down.

N_S	$\bar{\tau}_\omega$ [N · m]	$\bar{\tau}_\varepsilon$ [N · m]	$\bar{\tau}_\psi$ [N · m]	$\Delta\omega$ [deg/sec/Myr]	$\Delta\varepsilon$ [deg/Myr]	$\Delta\psi$ [deg/Myr]	t_{double} or t_{halve} [Myr]	State
SPC (ver. 2018-08-10)								
49,152	0.002464	0.1129	3.884	0.0001106	22.16	762.5	118.4	**Spin-up**
196,608	0.2062	0.06793	3.891	0.009252	13.33	763.7	1.416	**Spin-up**
786,432	0.3677	0.03348	3.894	0.01650	6.571	764.2	0.7941	**Spin-up**
3,145,728	0.4570	0.01469	3.892	0.02051	2.883	763.8	0.6389	**Spin-up**
SPC (ver. 2019-08-02)								
49,152	−0.1254	0.1179	4.179	−0.005609	23.07	817.4	1.168	**Spin-down**
196,608	−0.1250	0.1127	4.263	−0.005588	22.04	833.7	1.172	**Spin-down**
786,432	−0.09449	0.1031	4.325	−0.004225	20.16	845.7	1.550	**Spin-down**
3,145,728	−0.06851	0.09675	4.355	−0.003064	18.92	851.5	2.138	**Spin-down**

Table 2.5: Same with Table 2.4 but for the SfM-based shape models. A low-resolution model of 5,932 meshes was made from the 49,152-mesh SfM model (ver. 2018/08/10) by thinning out the meshes.

N_S	$\bar{\tau}_\omega$ [N · m]	$\bar{\tau}_\varepsilon$ [N · m]	$\bar{\tau}_\psi$ [N · m]	$\Delta\omega$ [deg/sec/Myr]	$\Delta\varepsilon$ [deg/Myr]	$\Delta\psi$ [deg/Myr]	$t_{\rm halve}$ [Myr]	State
Small model for test								
5,932	−0.009580	0.08876	3.854	−0.0004314	17.48	759.0	15.18	Spin-down
SfM (ver. 2018-08-04)								
49,152	−0.01480	0.1039	3.970	−0.0006651	20.42	780.2	9.849	**Spin-down**
196,608	−0.1659	0.1350	4.135	−0.007453	26.53	812.5	0.8789	**Spin-down**
786,432	−0.2491	0.1502	4.264	−0.01119	29.52	837.7	0.5853	**Spin-down**
3,145,728	−0.2850	0.1567	4.316	−0.01280	30.78	847.9	0.5116	**Spin-down**
SfM (ver. 2019-01-30)								
46,874	−0.3897	0.2028	4.211	−0.01744	39.68	824.0	0.3757	**Spin-down**
187,500	−0.4284	0.2027	4.290	−0.01917	39.65	839.1	0.3418	**Spin-down**
750,000	−0.4490	0.2039	4.354	−0.02009	39.90	851.8	0.3262	**Spin-down**
3,000,000	−0.4503	0.2029	4.373	−0.02015	39.70	855.4	0.3252	**Spin-down**
5,792,378	−0.4507	0.2029	4.376	−0.02016	39.69	856.0	0.3249	**Spin-down**

To understand the YORP effect on different shape models at a glance, Figure 2.10 plots the rates of change of the spin rate $\frac{d\omega}{dt}$ as a function of resolution of the shape models, characterized by the number of the surface facets N_S. Three of four shape model families show that Ryugu is decreasing its spin rate, excluding the early SPC models with a great spin-up. We cannot see behavior of convergence in the YORP effect even for the highest-resolution shape models. Breiter et al. (2009) checked that the magnitude of the YORP effect was highly sensitive to tiny features of the shape models and it became stronger as the number of the surface facets increased in most cases of asteroid Itokawa and Eros. Actually, we also conducted YORP simulations in cases of Itokawa and Eros for examining our calculation code and confirmed that the results are consistent with previous studies such as Čapek and Vokrouhlický (2004), Scheeres et al. (2007) and Breiter et al. (2009).

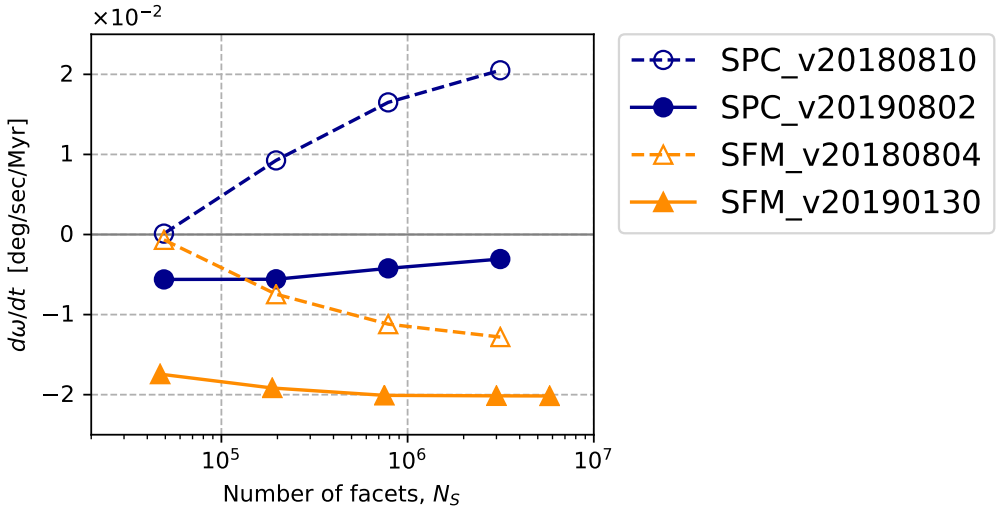

Figure 2.10: Rates of change of angular velocity for each shape model family as a function of the number of the surface facets.

Nextly, we checked how much the obliquity dependence of the YORP effect will change depending the input shape models. For a reason of computation costs, the results of the 49k and 200k models are shown here (See Figures 2.11 and 2.12). Though different types of shape models produce various strengths of the YORP effect, every model results in the asymptotic obliquities of 0° and 180°. In addition, the curves have nodes around $\varepsilon = 30^\circ$ and 150° which decide the subsequent spin evolution, except for the latest SfM model in the lower right panels. It is considered that the early SPC and SfM models in both resolutions will follow similar paths of spin evolution as our nominal model (the latest SPC model of 49k meshes).

2.6 Other Factors Affecting YORP

Thus far, we have simulated thermal torque on a spinning asteroid, but "self-shadowing" effect has not been considered in this section. When we consider thermal radiation from a surface of an irregularly-shaped body, local shadows, which are made by large boulders and hills especially near the terminator (i.e. the boundary region between the illuminated and dark hemispheres), could generate a great bias on the radiation from the body (Breiter et al., 2009). In addition, given a non-zero thermal conductivity of the surface, it is possible to change distributions of surface temperature and resultant thermal radiation (Čapek and Vokrouhlický, 2004). A re-absorption process of thermal emission from the heated surface has not yet been introduced into any YORP modeling because the computation cost increases

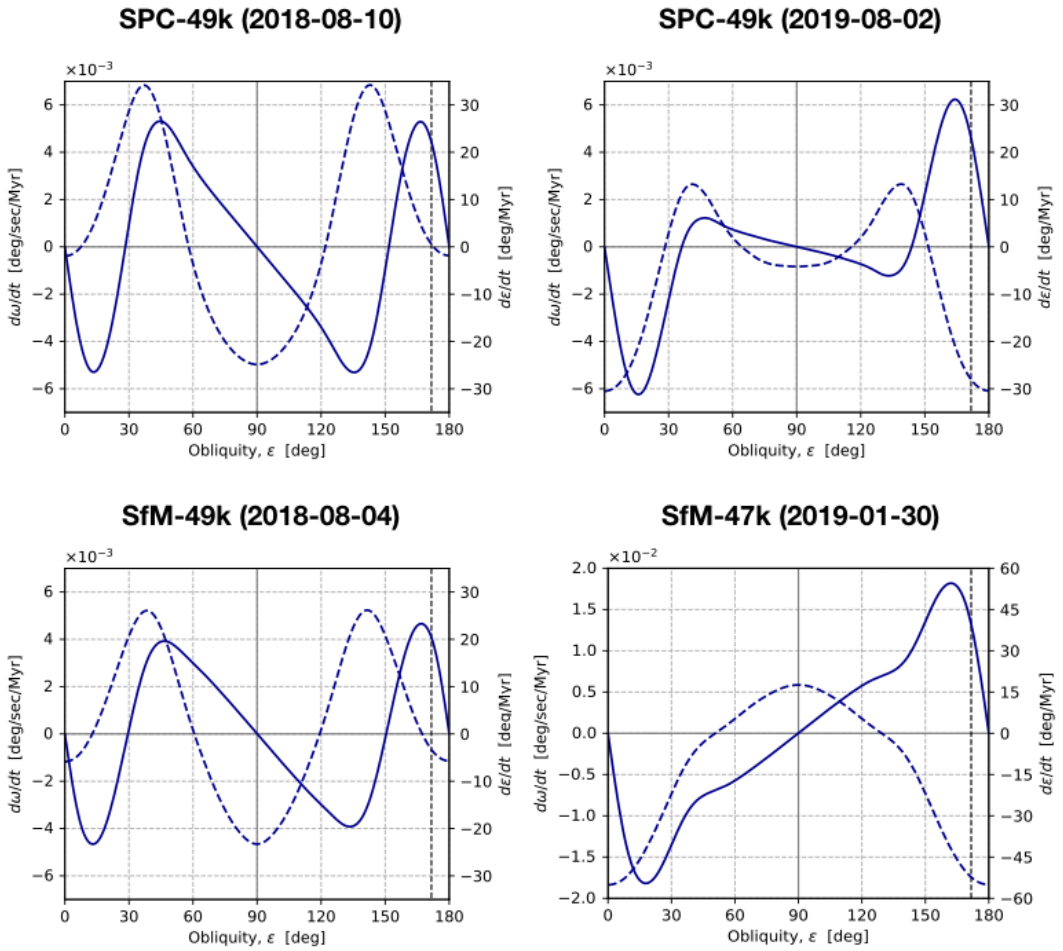

Figure 2.11: YORP effects on different kinds of shape models. The obliquity-dependence of the 49k-mesh models is shown here. The upper right panel is the same thing as our nominal case shown in Figure 2.4. The solid and dashed curves represent rates of change of the obliquity and the spin rate, respectively.

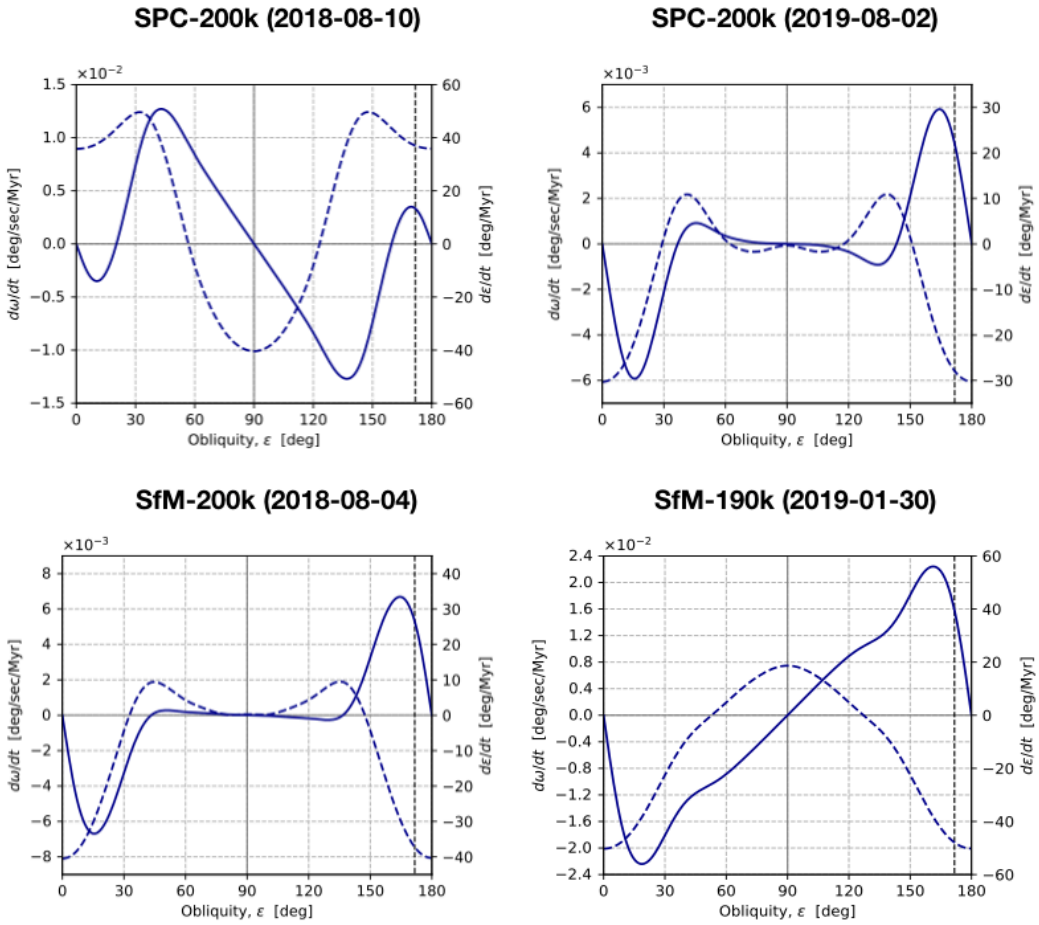

Figure 2.12: The same as in Figure 2.11 but for the higher-resolution shape models of 200k meshes.

exponentially ($\mathcal{O}(N_S^2)$) for the number of the surface elements) for iteration of processings for all surrounding elements around every surface element. However, a more accurate thermophysical model (TPM) has been developed to simulate the surface temperature distribution of Ryugu by the thermal infrared imager (TIR) team of Hayabusa2, taking the above additional effect into consideration (Takita et al., 2017). We compare our implementation for the YORP modeling with their TPM to evaluate how the Rubincam approximation works on Ryugu, where solar energy incident on the surface is directly converted to thermal radiation without a time lag in accordance with Equation 2.3.

From the thermophysical model, we obtained the distributions of the solar irradiation (including the self-shadowing effect) and the surface temperature over one rotation cycle on August 1, 2018 using the SfM-based 200k-mesh model (ver. 2018-08-04). The thermal inertia Γ was assumed to be 300 [$\mathrm{J \cdot m^{-2} \cdot s^{-1/2} \cdot K^{-1}}$], which corresponds to that of a porous rock. Figure 2.13 is a snapshot of the one-day thermal simulation. You can find local shadows of large boulders located near the terminator. The orange curves in the upper and lower panels in Figure 2.14 represent daily cycles of the torque component τ_ω to change the spin rate of Ryugu, respectively based on our model used until now and the Takita et al. (2017)'s TPM but directly converted to the thermal torque from the irradiation distribution. The former model generates the smooth profile of the YORP torque, on the other hand, the latter a fine irregularity because of the local shadows. The red curve shows the trend of the thermal torque based on the temperature distribution obtained from a 1-dimensional

heat diffusion equation in the TPM. The temperature-based profile tends to have a lower peak than the irradiation-based models because of lower contrast between the hemispheres of daytime and nighttime. Also, one can observe a phase lag of about a half hour because of the non-zero conductivity. The net torque $\bar{\tau}_\omega$ can be obtained by averaging over the whole day. Consequently, the net torque based on the Rubincam approximation ($\bar{\tau}_\omega = -0.3692$ [N $\cdot$ m]) agreed with that of the TPM within $\sim 10\%$. The local shadowing effect is considered to make the YORP on Ryugu stronger by about 10%. The phase lag between the models of zero and non-zero conductivity is turned out to be insignificant for the average rate of change of the angular velocity in this case. However, the non-zero conductivity is considered to be more effective on alteration of the spin pole direction (Čapek and Vokrouhlický, 2004)[2].

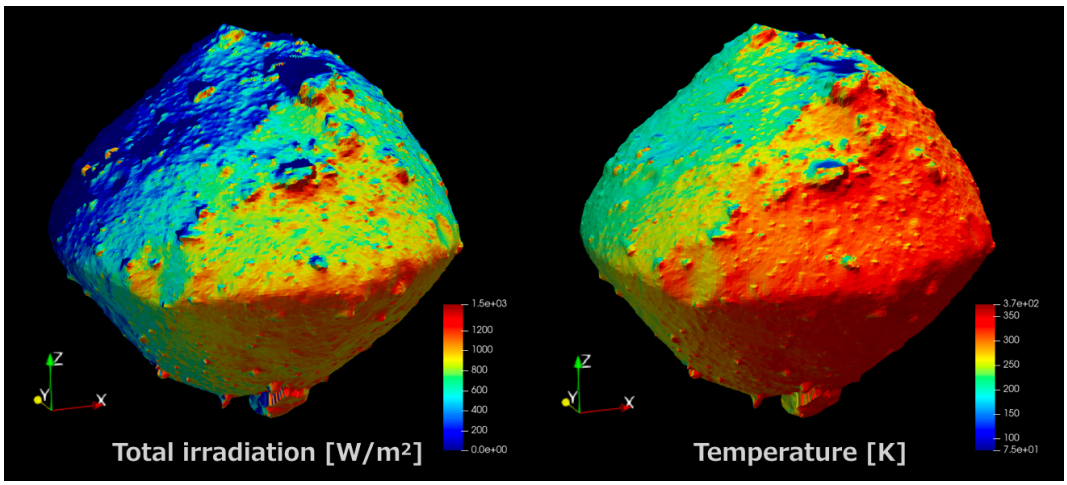

Figure 2.13: Distribution of radiation and temperature by means of the thermophysical model by Takita et al. (2017).

[2]Recently, the Thermal Infrared Imager (TIR) team of Hayabusa2 found a spatial distribution of the thermal conductivity of the surface materials. The slight difference in conductivity might vary the rate of the change of the obliquity rather than the spin rate.

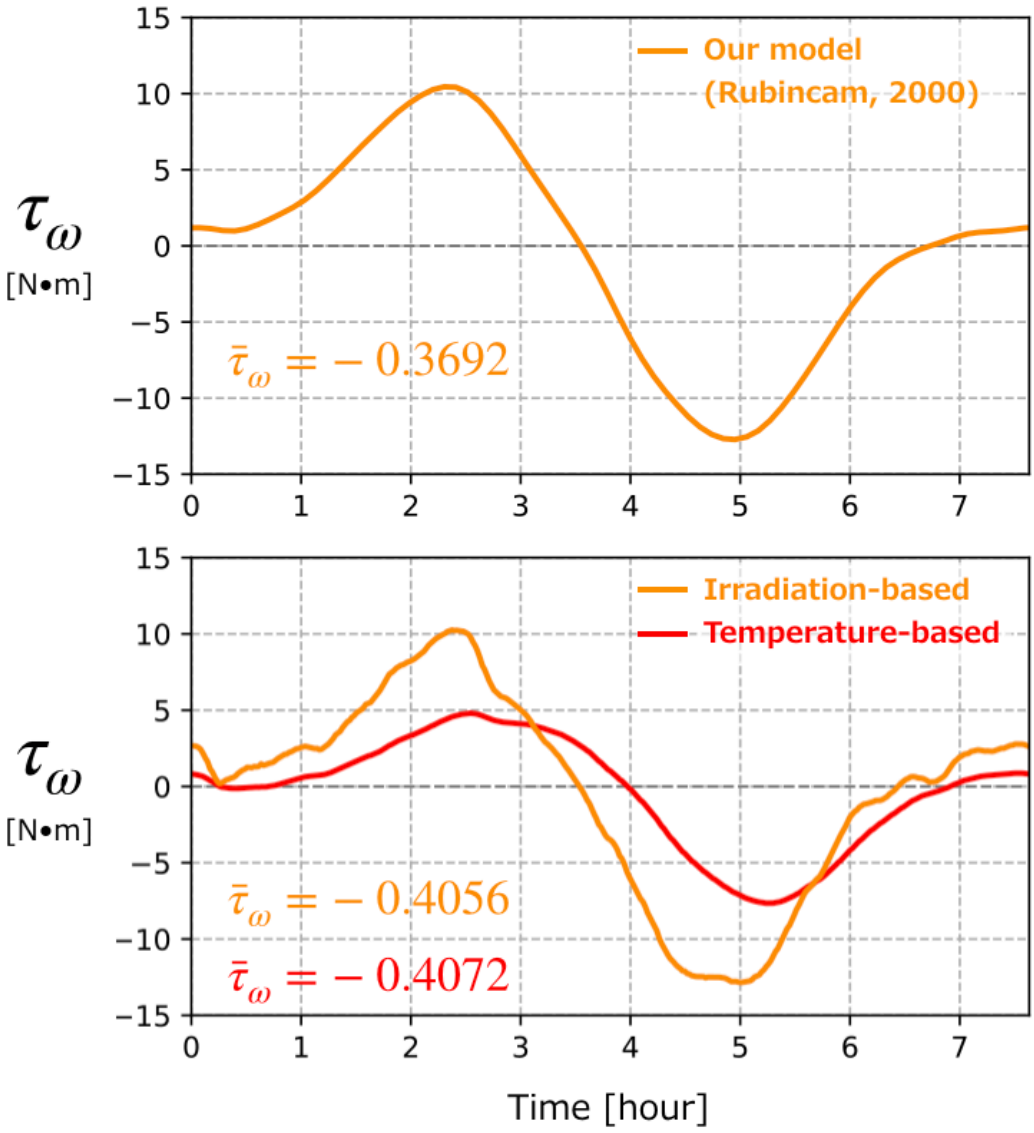

Figure 2.14: A comparison between thermal models. (*Upper*) Daily change of the ω-related torque of our implementation based on Rubincam (2000). (*Lower*) The same thing but based on the distributions of the solar irradiation (orange) and the surface temperature (red) obtained from the thermophysical model by Takita et al. (2017).

2.7 YORP Detectability during Rendezvous

The rotation period of Ryugu was monitored while the Hayabusa2 spacecraft stayed close to the asteroid. In Figure 2.15, we estimated a probable change in rotation period and a spin phase gap between cases with and without the YORP effect. We hereby used the year-averaged thermal torque derived from the 3-million-mesh model in each shape model family (See Tables 2.4 and 2.5). If the thermal torque is constantly working, the spin rate ω will linearly increase or decrease with time and the phase gap will quadratically spread as time goes by. The grey hatched area of the left panel is within an error of the SPC observation ($P = 27,477.43 \pm 0.07$ seconds from Watanabe et al. (2019)). In all cases shown here, it is quite difficult to detect a significant change in period during the rendezvous in a year or so. As a matter of fact, any significant signal of spin alteration has not been reported until now. Continuous observation campaigns are required for direct detection of the YORP effect on Ryugu, such as ground-based light curve observation or radar imaging at enough intervals.

2.8 Conclusion

In this chapter, we investigated the YORP-induced spin evolution of asteroid Ryugu. We also confirmed the simple thermal model based on Rubincam (2000) works well to a certain extent in the case of this asteroid. In the future, we are required to combine a realistic thermophysical model (e.g. non-zero thermal conductivity)

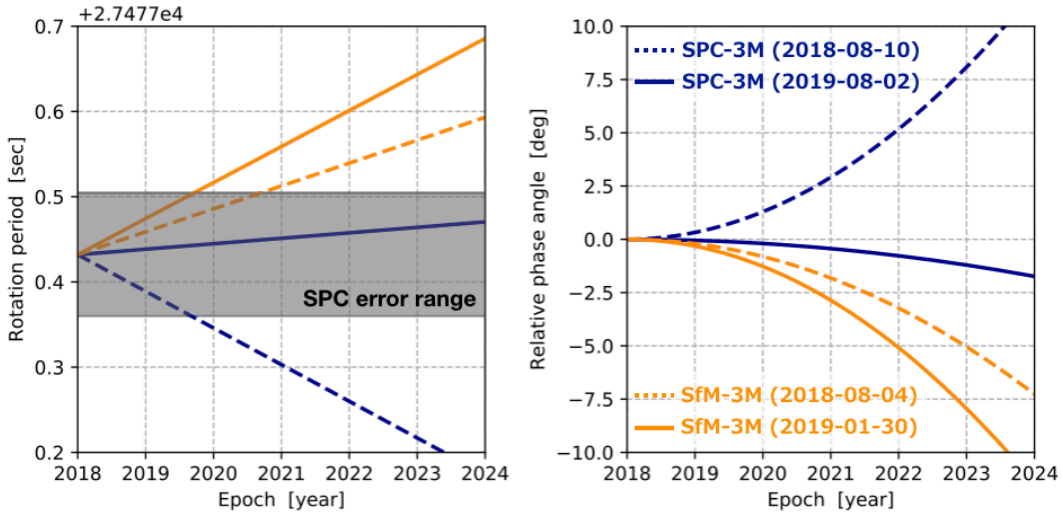

Figure 2.15: Probable change of the rotation period and the phase angle taking into account the YORP effect.

with a simulation of the long-term evolution of the spin state.

Chapter 3

Density Distribution Estimation for Small Bodies

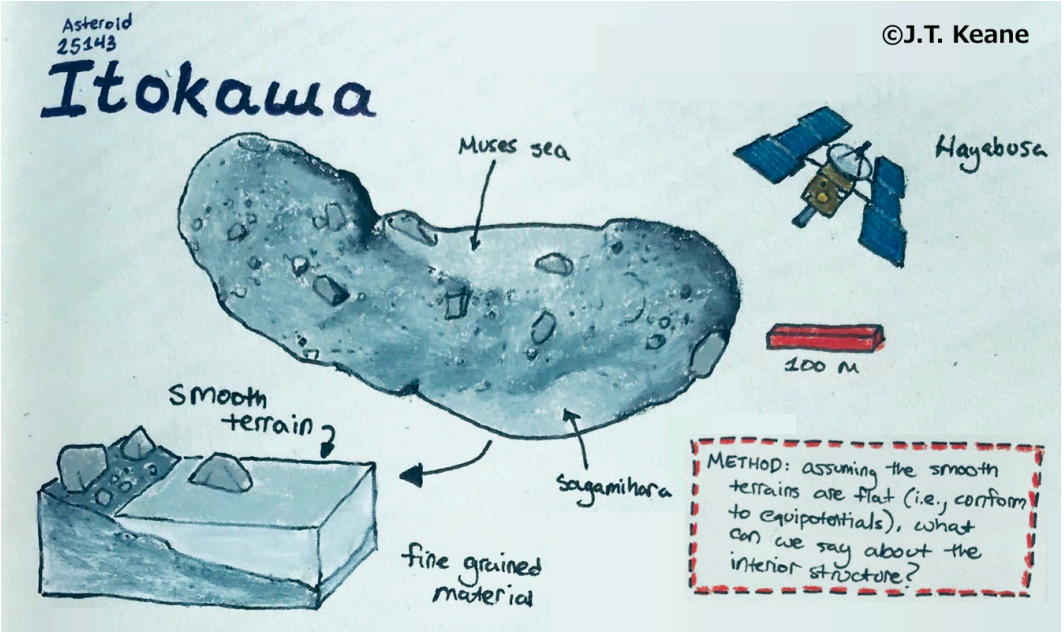

A new technique to make a constrain on the interior of small bodies, published from Kanamaru et al. (2019).

3.1 Interiors of Small Bodies

The interior structure of small solar system bodies tell us about how planetary objects formed and evolved. In spite of many ground-based observations and spacecraft missions, we have much less information about the interiors of asteroids than of their surface properties. The sizes, bulk densities and inferred porosities of asteroids are some of the most fundamental physical properties for investigating their internal structures and formation processes. Larger asteroids generally have more spherical shapes and higher bulk densities than smaller ones (Carry, 2012). Asteroids with sizes of a few hundred km could have experienced temperatures high enough for them to have fully or partially differentiated (Neumann et al., 2013). On the other hand, smaller asteroids tend to have irregular shapes and lower bulk densities. Their shapes and internal structures result from impact events and the disruption of their parent bodies and subsequent re-accumulation processes.

Asteroid 433 Eros is one of the asteroids that was observed in detail, by the Near Earth Asteroid Rendezvous (NEAR) spacecraft mission (Veverka et al., 2000). The bulk density of Eros is estimated to be 2,670 $\pm$ 30 $\mathrm{kg/m^3}$ by combining a measurement of its mass and volume (Yeomans et al., 2000). According to the gravity measurements derived from the spacecraft tracking data, the first degree and order terms of the gravity spherical harmonic coefficients (C_{11}, S_{11}, C_{10}) show that the center-of-mass (COM) is offset from the center-of-figure (COF) by only $(-9.7, 2.4, 32.6)$ m in each of the three principal axis directions (Miller et al.,

2002). The COM-COF offset is small for Eros' size of 34.4 $\times$ 11.2 $\times$ 11.2 km and it implies that there is no significant hemispherical density contrasts (Konopliv et al., 2002; Miller et al., 2002). Other gravity coefficients up to several degrees and orders are also consistent with a uniform interior density distribution (Konopliv et al., 2002; Miller et al., 2002). Asteroid Eros is commonly classified as a coherent and strength dominated object with interior fractures, whose porosity is estimated to be approximately 20% (Wilkison et al., 2002).

The Near-Earth asteroid 25143 Itokawa was visited by the Japanese spacecraft mission, Hayabusa (Fujiwara et al., 2006). Itokawa is a sub-kilometer sized asteroid (535 meters by 294 meters by 209 meters) with a low bulk density of 1,950 $\pm$ 140 $\mathrm{kg/m^3}$ and a bi-lobed shape. The distinctive shape of Itokawa is often compared to a shape of a sea otter and its two lobes are called the "head" and the "body". Based on estimates of its composition and bulk density, this object is believed to contain a porosity of about 40% (Abe et al., 2006,?; Tsuchiyama et al., 2011). It is an important and unique target for better understanding the formation processes of small rubble-pile asteroids that are common in the asteroid belt. The Hayabusa mission team estimated the mass of Itokawa from the spacecraft orbit during a descent operation with an uncertainty of 5% (Abe et al., 2006), but the gravity field at higher degree and order was not observed. Thus, based solely on the observed mass measurement, it is difficult to determine whether the interior density distribution is homogeneous or not.

The surface of Itokawa is composed of rough terrain that is comprised of boul-

ders, but about 20% of the surface is covered with centimeter-sized gravels that are commonly called "smooth terrain" (Demura et al., 2006; Fujiwara et al., 2006; Saito et al., 2006). This smooth terrain is associated with areas where the gravitational potential is low, and is considered to have formed by the downslope mass movement and accumulation of the fine gravels (Miyamoto et al., 2007). Over geologic time, it would be expected that the finest grained materials would approach the shape of an equi-potential surface (see Richardson and Bowling, 2014), analogous to other strengthless materials such as Earth's oceans.

The objective of this study is to develop a method to estimate the interior density distribution within a small solar system body. Our method is based on estimating the gravity field for the object using a topographic shape model and an *a priori* interior density structure. We then determine the heights of the surface above an equi-potential surface and vary the density structure such that the smooth terrains approximate locally equi-potential surfaces. We applied this estimation method to asteroid Itokawa, aiming to determine if there is a difference in density between its two lobes, the head and body, or if the adjoing "neck" is compressed. In Section 3.2, we describe how we simulate the gravity field of an asteroid with an arbitrary density distribution. The inversion technique to estimate the density distribution is then described in Section 3.3. In Section 3.4, we present the results of our inversion, and in Section 3.4.1 and 3.4.3, we discuss the implications our work.

3.2 Gravity Modeling of Small Bodies

The classical way to represent the gravity field of a celestial object is through the spherical harmonic expansion of its gravitational potential. With this approach, the gravitational potential can be expressed at a position of radius r, latitude θ and longitude λ as follows:

$$U(r,\theta,\lambda) = \frac{GM}{r}\left[1 + \sum_{l=1}^{\infty}\sum_{m=0}^{l}\left(\frac{R}{r}\right)^{l} P_{lm}(\sin\theta)\left(C_{lm}\cos m\lambda + S_{lm}\sin m\lambda\right)\right] \tag{3.1}$$

where G, M and R are the Newtonian constant of gravitation, the total mass of the body and the reference radius of the spherical harmonic coefficients, respectively. P_{lm} is the associated Legendre function of degree l and order m, and the spherical harmonic coefficients C_{lm} and S_{lm} reflect information on the shape and interior density distribution of the body. Using the gravity harmonic coefficients determined by spacecraft dynamics, the gravitational potential can be computed at any arbitrary position exterior to the smallest sphere that encloses the object, the so-called Brillouin sphere. The gravitational harmonic coefficients of an asteroid can also be calculated directly by integrating the density distribution throughout its entire body if the density distribution is known *a priori*. Given a polyhedral shape model of an asteroid, whose surface is covered with triangular facets, it is possible to calculate the spherical harmonic coefficients analytically (Werner, 1997). In some cases, it is possible to constrain the interior density distribution within a small body by a least squares fitting between simulated and measured gravitational coefficients (Scheeres

et al., 2000; Takahashi and Scheeres, 2014).

It is known that spherical harmonic expansions can diverge in the vicinity of an irregular shaped asteroid and that they are not always suitable to calculate the gravity field on the surface of an asteroid, particularly when the observational point is below the Brillouin sphere (as an example see Hirt and Kuhn (2017)). Direct integration of a constant-density polyhedron has been widely used to avoid this problem (Werner and Scheeres, 1996). The polyhedral approach is an analytic integration of the mass distribution within a polyhedron, based on the assumption that the density is uniform across the entire object. This method is free from divergence and is capable of calculating the gravity field at any point above or below the surface.

In this study, we adopted a method where the object is decomposed into connecting tetrahedral elements. Instead of calculating the gravitational potential of this polyhedron analytically, to save computational time, we placed a single point mass in the interior of each individual tetrahedron. This "mascon" (short for "mass concentration") method is easy to be implemented for an arbitrary density distribution, and the accuracy can be adjusted by changing the characteristic size of each tetrahedron. This technique is described in the following section.

3.2.1 Mascon gravity modeling

A polyhedral shape model of the asteroid Itokawa was constructed from Hayabusa spacecraft images by means of the stereophotoclinometry (SPC) method by Gaskell et al. (2006). The initial shape model contained only surface triangular facets, so the

shape model was imported into the Netgen Mesh Generator (Schöberl, 1997), which is a 3-dimensional Delaunay triangulation library, and the polyhedral shape model was divided into numerous volume elements. Every volume element has the shape of a tetrahedron, and facets that are exposed on the surface of the polyhedron are recognized as surface elements. We prepared numerical mesh models of Itokawa using four different resolutions, which are characterized by the number of volume and surface elements, N_V and N_S, respectively. These four shape models are listed in Table 3.1 along with the average sizes of the volume and surface elements, $\bar{D}_V$ and $\bar{D}_S$, respectively. The original shape model is made of 786,432 surface facets, which has an average horizontal spatial resolution of about 0.8 meters.

Table 3.1: Shape models of Itokawa using four different resolutions along with the original shape model constructed by Gaskell et al. (2006). The shape model resolution is characterized by the number of volume elements and surface elements, N_V and N_S, respectively. $\bar{D}_V$ denotes the mean diameter of a sphere of equivalent volume and $\bar{D}_S$ denotes the mean diameter of a circle of equivalent area of the surface elements. The highest resolution model of 3.6 million mascons are used in the later analysis.

	N_V	N_S	$\bar{D}_V$ [m]	$\bar{D}_S$ [m]
Original	—-	786,432	—-	0.8
(1)	282,987	60,774	3.2	2.3
(2)	1,083,253	142,252	2.0	1.5
(3)	1,693,335	149,062	2.3	1.5
(4)*	3,613,429	173,974	2.0	1.5

*Highest resolution model used for the later analysis.

A mascon model expresses the gravitational potential of an object by summing the gravitational potential of a number of point masses. For our approach, we

placed a single point mass at the centroid of each tetrahedral volume element. The gravitational potential U_{grav} can be calculated at an arbitrary location $\boldsymbol{r}$ using

$$U_{grav}(\boldsymbol{r}) = -G \sum_{i=1}^{N_V} \frac{\rho_i v_i}{|\boldsymbol{r_i} - \boldsymbol{r}|} \tag{3.2}$$

where ρ_i, v_i and $\boldsymbol{r_i}$ are the density, volume and the vector position of the ith volume element, respectively. Densities of volume elements will be assigned later according to a model of the object's density distribution, under the condition that the total mass is equal to the known mass of the asteroid.

In a reference frame attached to a rotating asteroid, the surface potential is affected by its rotation. After computing the gravitational potential as stated above, we added the corresponding rotational potential U_{rot} to the mascon solution. The sum of the gravitational and rotational potential is given as

$$\begin{aligned} U(\boldsymbol{r}) &= U_{grav} + U_{rot} \\ &= -G \sum_{i=1}^{N_V} \frac{\rho_i v_i}{|\boldsymbol{r_i} - \boldsymbol{r}|} - \frac{1}{2}\omega^2 r_\perp^2 \end{aligned} \tag{3.3}$$

where ω is the spin rate of the Itokawa's rotation, and $r_\perp = \sqrt{x^2 + y^2}$ is the distance perpendicular to the rotation axis. The rotation axis is aligned with the z-axis of the shape model, and the rotation period of Itokawa is 12.1324 hours (Fujiwara et al., 2006). The total gravity vector $\boldsymbol{g}$ is obtained by taking the space derivative of Eq.

(3.3).

$$\boldsymbol{g}(\boldsymbol{r}) = G \sum_{i=1}^{N_V} \frac{\rho_i v_i}{|\boldsymbol{r_i} - \boldsymbol{r}|^3} (\boldsymbol{r_i} - \boldsymbol{r}) - \omega^2 \boldsymbol{r}_\perp \tag{3.4}$$

In order to obtain a global map of the gravity field on the surface of the asteroid, it is only necessary to evaluate Eqs. (3.3) and (3.4) at locations $\boldsymbol{r}$, where $\boldsymbol{r}$ is taken as the centroid of every surface facet.

Given our approximation of treating tetrahedral elements by mascons, there is a risk that the point-mass approximation could give rise to a significant error, especially in the vicinity of the asteroid's surface. We evaluated the calculation error of the mascon modeling approach by comparing it to the polyhedral approach of Werner and Scheeres (1996). The relative error of the potential ε_U between the two techniques at a position $\boldsymbol{r}$ is defined as

$$\varepsilon_U(\boldsymbol{r}) = \left| \frac{U_{mascon}(\boldsymbol{r}) - U_{polyhedron}(\boldsymbol{r})}{U_{polyhedron}(\boldsymbol{r})} \right| \tag{3.5}$$

and the relative error of the magnitude of the gravitational acceleration, $\varepsilon_g(\boldsymbol{r})$ is defined in a similar manner.

Figure 3.1 shows the relative error of the potential (a) and acceleration (b) as a function of the number of the volume elements N_V utilized in the 3D shape model. We utilized shape models of Itokawa using four different resolutions (N_V = 282,987, 1,083,253, 1,693,335 and 3,613,429) as listed in Table 3.1. In these

plots, the central horizontal line of each grey box indicates the median of the errors calculated on every surface element of the shape model. The upper and lower limits of each box represent the first and third quartile, respectively, and the maximum and minimum errors are shown by the extent of the vertical lines. The minimum relative errors are about 10^{-10} for these models and they are so small that they have no influence on our analysis. In general, the accuracy of the mascon modeling improves as the number of the point masses increases. Furthermore, we note that the acceleration relative errors are always larger than the potential relative errors because the acceleration of each point-mass attenuates by the square of the distance and is more influenced by adjacent volume elements. For our later analysis, we utilized the highest resolution model of 3.6 million volume elements among four different resolutions as shown in Table 3.1 and Figure 3.1. For this shape model that contains N_V = 3,613,429 volume elements and N_S = 173,974 surface elements, the median relative errors of the gravitational potential and acceleration are 3.7×10^{-6} and 2.2×10^{-3}, respectively. The maximum relative errors are respectively 5.7×10^{-5} and 2.2×10^{-2}. The tests show that the results presented later are insensitive to reducing the number of volume elements by an order of magnitude from the maximum tested.

3.2.2 Elevation

Given a shape model of an asteroid, as well as an estimate of the gravitational potential and acceleration on the surface, we can compute the distance of each

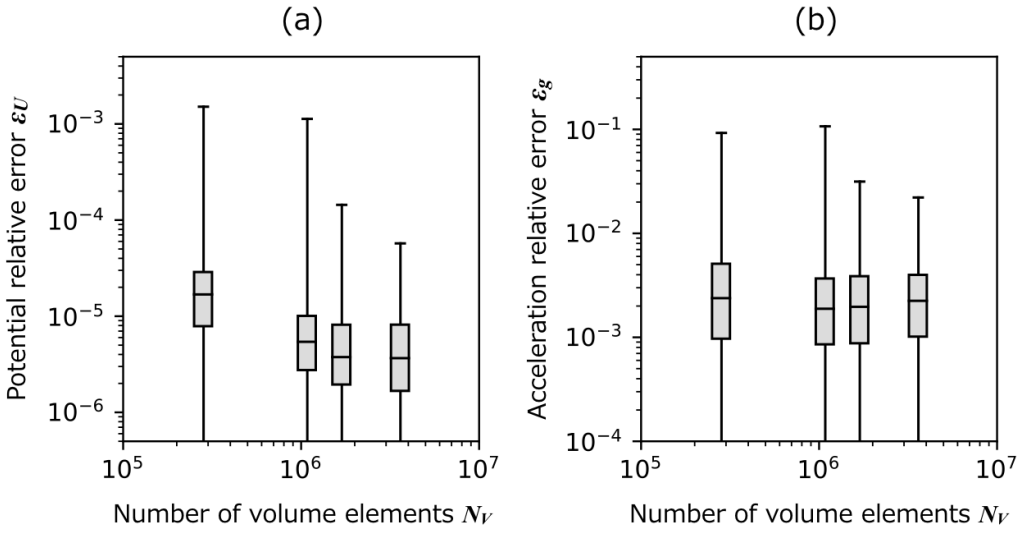

Figure 3.1: Relative errors of the potential (a) and the magnitude of the acceleration (b) as a function of the number of volume elements of the Itokawa shape model. Relative errors are defined as the difference between a mascon solution, where tetrahedral elements are approximated by point masses, and an analytical solution for the entire polyhedral shape. The central horizontal line represents the median, boxes represent the limits of the first and third quartiles, and the vertical lines denote the maximum and minimum relative errors.

surface element above or below a constant potential surface. This is commonly referred to as the dynamic height, h, and can be computed to first order using a Taylor series expansion of the potential with respect to an arbitrary reference value

$$U(r+h) = U(r) + \frac{dU(r)}{dr}h \tag{3.6}$$

where r is the reference radius and where the potential $U(r)$ is defined to be U_{ref}. Approximating the radial derivative of the potential as the gravitational acceleration on the surface g_s, this can be rearranged into the familiar form (e.g., Thomas (1993)):

$$h(\boldsymbol{r}) = \frac{U(\boldsymbol{r}) - U_{ref}}{g_s(\boldsymbol{r})} \tag{3.7}$$

For global mapping, the reference potential U_{ref} will be chosen to be equal to the average potential across the surface of the object. However, later, we will also make use of the average potential within a specific region. The potential $U(\boldsymbol{r})$ is calculated in the center of every surface element and average values are computed taking into account the area of each surface element. The elevation has a dimension of length and is simply how high or low a certain place is above or below the reference potential. Mass wasting processes generally move materials downslope, which corresponds to regions of decreasing dynamic elevations.

In Figure 3.2, we show the dynamic elevations that we computed for Itokawa. The global map of the dynamic elevations is visualized by Mayavi, 3D scientific data visualization tool (Ramachandran and Varoquaux, 2011). Here, we have used a shape

model with 3,613,429 volume elements and 173,974 surface elements, which is the highest resolution model in Table 3.1 and Figure 3.1, and have assumed a constant density of the body when computing the gravitational potentials and accelerations. The mean density of Itokawa is here assumed to be 2,020 $\mathrm{kg/m^3}$, derived from the mass measurement by Abe et al. (2006) and the volume of the above shape model. The elevations vary from -25 to 54 meters, and the lowest elevations are found to be located in MUSES-C Regio, which is a region that is extremely smooth and that lacks large boulders.

The greatest uncertainty in calculating the dynamic heights (for a given mass distribution model) concerns the calculation of the gravitational acceleration at the surface. Our sensitivity tests in Figure 3.1 show that the average uncertainty is less than 0.3% but that the uncertainty can be as high as 2% in some regions. Given that the largest dynamic elevations are about 54 meters, this suggests that the average uncertainty is about 0.16 meters, and that the maximum error is about 1 meter.

3.3 Method for Estimating Density Distribution

Itokawa has extensive regions that are composed of smooth terrains (Fujiwara et al., 2006). It has been noted previously that these correspond approximately to regions of low gravitational potential, and that mass-wasting processes would

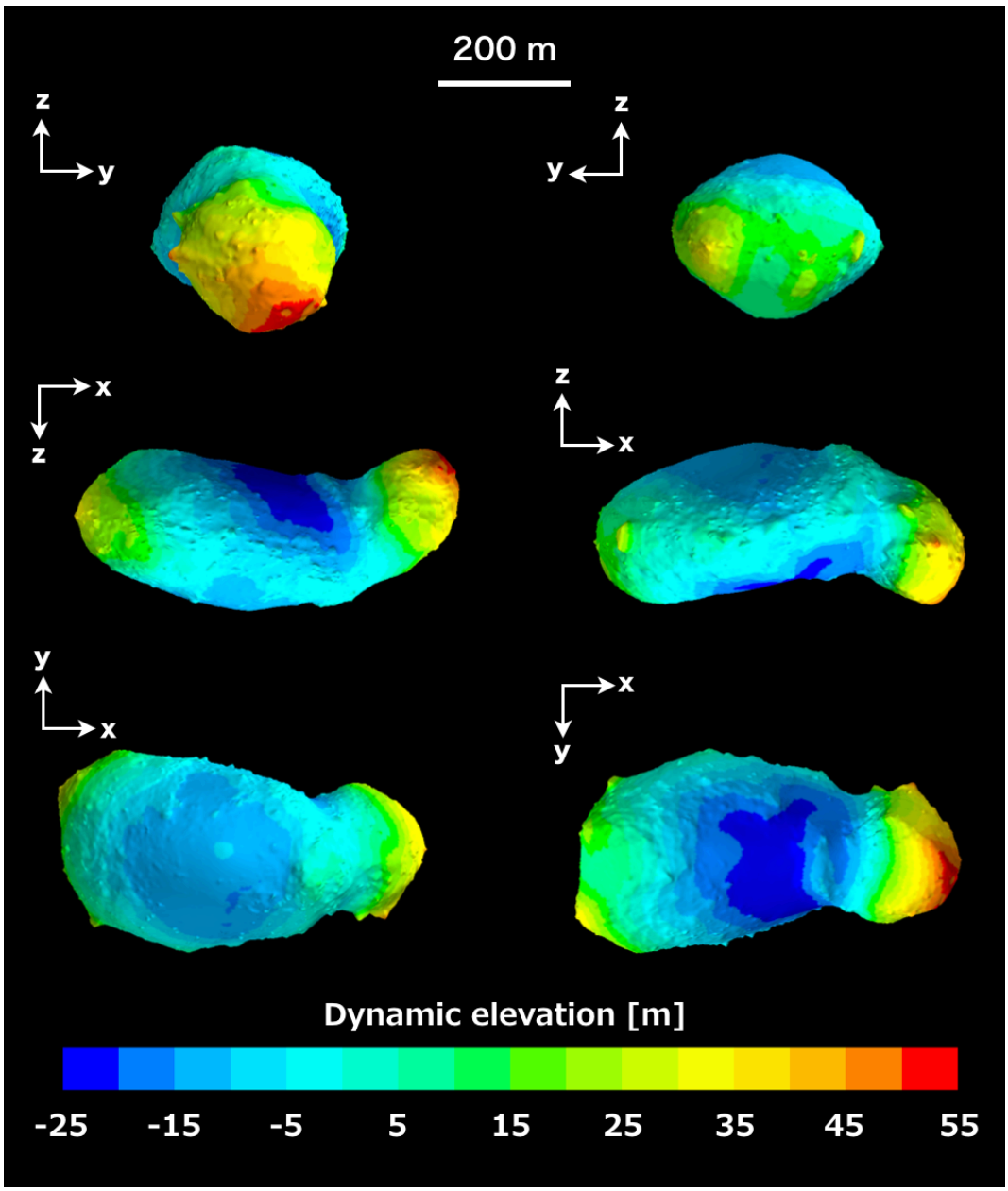

Figure 3.2: Global map of the dynamic elevations of Itokawa, viewed from $\pm x$, $\pm y$ and $\pm z$ axes. Here, we assumed a uniform density throughout the asteroid and defined the average potential across the surface as the reference potential.

have a tendency to move materials downslope into these regions (Miyamoto et al., 2007). In this study, we will make the assumption that these regions correspond to an equi-potential surface, which is the final equilibrium state of surfaces that undergo erosive processes. With the observed shape of the body, we then invert for the density distribution within the asteroid to find those solutions that best provides a flat surface in the regions of the smooth terrains. As a part of this analysis, we mapped the regions of the smooth terrain using both the shape model of Itokawa and visible imagery as described in Section 3.3.1. In Section 3.3.2, we describe the inversion technique of the interior density distribution and *a priori* density structures that will be tested in this paper.

3.3.1 Smooth terrain mapping

We used the Small Body Mapping Tool (SBMT) for mapping the smooth terrain on Itokawa, which is a 3D visualization tool for mapping geological features and is capable of projecting spacecraft images onto shape models (Ernst et al., 2018). A global mosaic map of Itokawa (3,600 $\times$ 7,200 pixels) constructed by Stooke (2012) was projected onto the same shape model used for computing the surface elevations. The shape model used for this purpose contains 173,974 surface elements, and the average of the equivalent circle diameter of each surface element is 1.5 meters. Since the cylindrical projection of the global mosaic was sometimes distorted, we used other visible images that were obtained by the Asteroid Multiband Imaging CAmera (AMICA) for identifying the smooth terrain (Nakamura et al., 2001; Saito

et al., 2006). The best images for mapping the smooth terrains of MUSES-C Regio are ST_2472657784_v and ST_247431509_v. We chose ST_2480981469_v, ST_2481442195_v and ST_2481672682_v for mapping other smooth terrains in the north polar region, including Sagamihara and Uchinoura Regio. The spatial resolutions of the projected images are approximately 0.4 to 0.5 meters per pixel.

In mapping the extent of smooth terrains on Itokawa, we utilized two criteria. First, we made use of the above images, and drew tentative boundaries around regions that were visibly smooth and had only a small number of obvious boulders. As a secondary criteria for identifying the smooth terrain, we also used the surface roughness derived from the shape model. The roughness parameter at a specific location is here defined as the standard deviation of the surface elevations within a circle of a specific scale (that is, a diameter of the circle). We used the surface roughness in 6 meter diameter circles to help define the boundaries of the smooth terrain. As shown in Figure 3.3, the surface roughness ranges from less than 0.1 meters to 2.1 meters across the surface of Itokawa, and it highlights the flatness of the smooth terrains with respect to the roughness of the other rocky regions. Finally, we combined the two tentative boundary maps and decided upon a single boundary that best fit both observations.

The mapped smoothed regions included MUSES-C Regio, Sagamihara Regio and Uchinoura Regio as shown in Figure 3.4. MUSES-C Regio is the largest smooth terrain on Itokawa, and is located in the south polar region. This region was divided into five pieces for ease of use with the SBMT for exporting the geometry of the

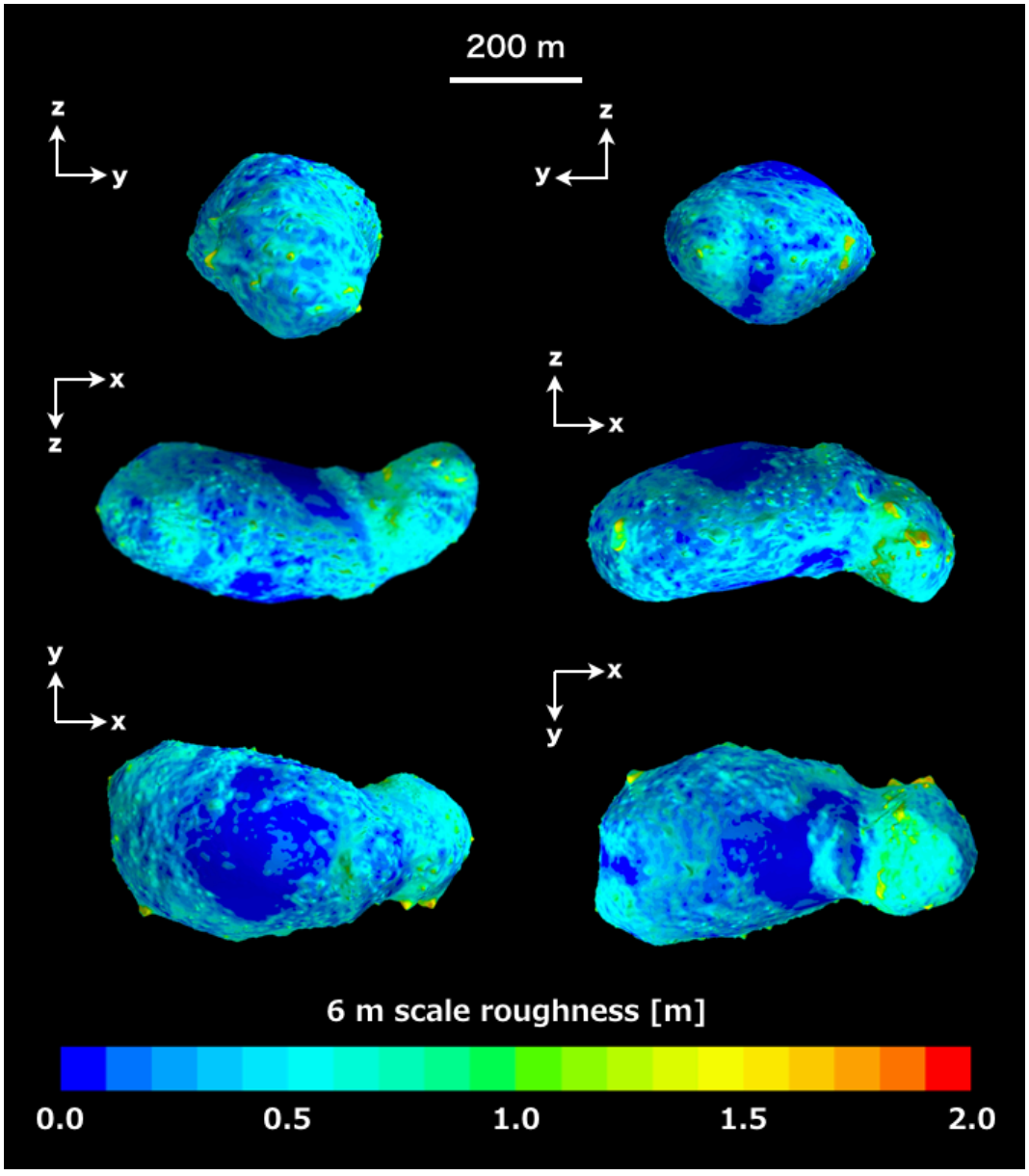

Figure 3.3: Global map of the surface roughness of Itokawa visualized by Mayavi. The surface roughness is here defined as the standard deviation of the dynamic elevations within a 6 meter diameter circle for every surface element.

surface elements (Region ID: 1-a to 1-e). Sagamihara Regio is the second largest smooth terrain on Itokawa in the north polar region (Region ID: 2). There exist many boulders in Sagamihara and its boundary is not as clear and distinct as for MUSES-C Regio. The third largest smooth terrain, Uchinoura is a circular depression with a flat floor that is adjacent to Sagamihara Regio (Region ID: 3) (Hirata et al., 2009). All extracted regions are summarized in Table 3.2.

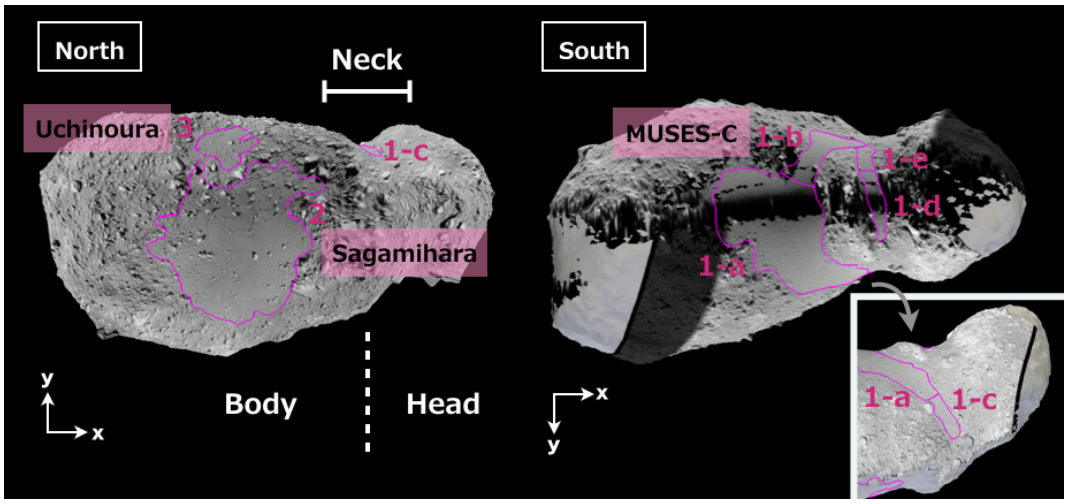

Figure 3.4: Smooth terrain mapped on Itokawa based on visible imagery and surface roughness. Some images are projected onto the 3D shape model of Itokawa by the Small Body Mapping Tool.

Table 3.2: Properties of the mapped smooth terrains. The mean elevation in each region is derived from the gravitational potential of a uniform density body according to Eq. (3.7), and the reference potential of the dynamic elevations is the mean potential over the surface of Itokawa. The surface roughness is defined as the elevation standard deviation within 6 meter diameter circles.

ID number	Location $(^\circ N, ^\circ E)$	Area [m^2]	Mean elevation [m]	Mean roughness [m]	Descriptions
1-a	(-57, 56)	17,747	-21.8	0.096	MUSES-C Regio.
1-b	(-32, 321)	3,913	-21.0	0.11	MUSES-C Regio.
1-c	(17, 28)	1,321	-13.8	0.27	MUSES-C Regio.
1-d	(-29, 4)	1,692	-16.6	0.15	A part of MUSES-C in the neck region between the two lobes.
1-e	(-23, 339)	1,088	-18.5	0.12	A part of MUSES-C with a larger concentration of boulders.
2	(67, 225)	24,653	-13.8	0.077	Sagamihara Regio. Numerous boulders exist in this region.
3	(46, 110)	3,261	-12.3	0.075	Uchinoura Regio. A circular depression with a smooth floor.

3.3.2 Inversion technique

Richardson and Bowling (2014) were the first to investigate a method to estimate the bulk density of a small body by minimizing the variance of the gravity potential on its surface. This method assumes that over geologic time, mass-wasting processes will act to redistribute materials such that the surface will tend toward an equi-potential surface. If there exists loose regolith on the asteroid, seismic shaking induced by meteorite bombardments would help to trigger mass movement from high standing regions to low standing regions. In addition, the mass movement on small bodies may be influenced by volatile activities on comets and alteration of the surface gravity field due to YORP spin-up/-down. The YORP effect is a change of an asteroid's spin state by the solar radiation and thermal emission (Rubincam, 2000). The surface gravity field of an asteroid depends on both the gravitational potential and the rotational potential, with the former depending upon the assumed density. Though the bulk density can be estimated by minimizing the difference between the observed shape of the asteroid and an equi-potential surface, they found that the method did not work well for Itokawa. Applied globally, they obtained a bulk density of 330 $\mathrm{kg/m^3}$, which is far lower than the known value. When applied to the region of Sagamihara, a more realistic value was obtained, but with large uncertainties. In any case, their study did not consider the possibility of different densities for the head, body or neck regions that we consider here.

In different studies, Motooka and Kawaguchi (2012) and Kanamaru and Sasaki (2019) attempted to fit the global shape of Itokawa to a single equi-potential surface.

In contrast to Richardson and Bowling (2014), they investigated how modifying the densities of the head and body affected the global fit. However, given the two lobe structure of the asteroid, and the presence of both smooth and rough terrains, it is unlikely that the global shape would approximate a single equi-potential. In this study, we instead hypothesize that the smooth terrain is formed by the accumulation of fine gravels and that it is only these surfaces that should approximate flat surfaces. Under this hypothesis, the remaining regions have sufficient strength to retain the bi-lobed structure of the asteroid over geologic time. These are reasonable hypotheses if the relaxation time of loose materials towards an equilibrium state or a low-slope state is shorter than other time scales of dynamical changes on the asteroid surface, such as a significant change of the spin rate by the YORP effect. The characteristic timescale of YORP-induced rotational variations varies from hundreds of thousands of years to millions of years, depending on the asteroid size, shape and orbital semi-major axis (Bottke et al., 2006).

For our inversions that solve for the density distribution, we introduce a measure of the misfit σ_h, which measures the departure of a smooth terrain unit from an equi-potential surface. In particular, the misfit σ_h is defined to be the weighted root-mean-square difference between the observed and average dynamic elevations over a smooth terrain unit:

$$\sigma_h = \sqrt{\sum_{i=1}^{n_S} A_i (h_i - h_{mean})^2 \Big/ \sum_{i=1}^{n_S} A_i} \tag{3.8}$$

where h_i and A_i are the dynamic elevation and area of the ith surface element in each region that is composed of n_S surface elements. The mean dynamic elevation h_{mean} is the weighted average of the smooth terrain elevations by the areas of each surface element.

$$h_{mean} = \sum_{i=1}^{n_S} A_i h_i \Big/ \sum_{i=1}^{n_S} A_i \tag{3.9}$$

The best fitting model is the model that possesses the smallest standard deviation $\sigma_{h,\,min}$.

Given that we have no constraints on the gravity field of Itokawa (besides its total mass), and that the inversion for the internal density structure of a body is inherently non-unique, we have decided to parameterize the density structure of Itokawa in a simple manner. In particular, based on the morphology of the body, we will consider models where the density of the two lobes of Itokawa differ, and where the density of the neck region is different from the two lobes. For these models, each component will be treated as having a constant density. This simplifies our gravity calculations enormously, as we only need to calculate the gravity field of each component a single time using a density of 1.0: the gravity for an arbitrary density is then obtained by multiplying the obtained values by the actual density.

For our inversions, we assumed three types of density maps as demonstrated in Figure 3.5.

- The compressed head model: In this model, the head and body of Itokawa have different densities as shown in the left panel of Figure 3.5. The boundary

of the two lobes is here defined at x = 150 m in the body fixed frame, with the center being defined as the center-of-figure of the asteroid. By choosing the density of one lobe, the density of the other can be obtained using the known total mass.

- The compressed neck model: In this model, the contact of the two lobes is considered to be a finite width neck that has a different density than the head and body. The extent of the neck is here defined from x = 120 m to x = 180 m as shown in the right panel of Figure 3.5. For this model, we consider the densities of the head and body to be the same, and the densities of the lobes and the neck are constrained by the total mass of the asteroid.

- The compressed neck with different density head and body model: This model differs from the previous one in that we allow the densities of the head, body and neck to vary. In practice, we pick the densities of two of the components and then solve for the third using the known total mass.

In the above models, we make use of the total mass of Itokawa 3.58×10^{10} kg, which was estimated by the Hayabusa GM measurement (Abe et al., 2006). The shape model used in this study has a volume of 1.77×10^{7} m^3, which corresponds to a mean bulk density of $2,020$ kg/m^3. This value is consistent with the bulk density of 1,950 $\pm$ 140 kg/m^3 estimated by Abe et al. (2006).

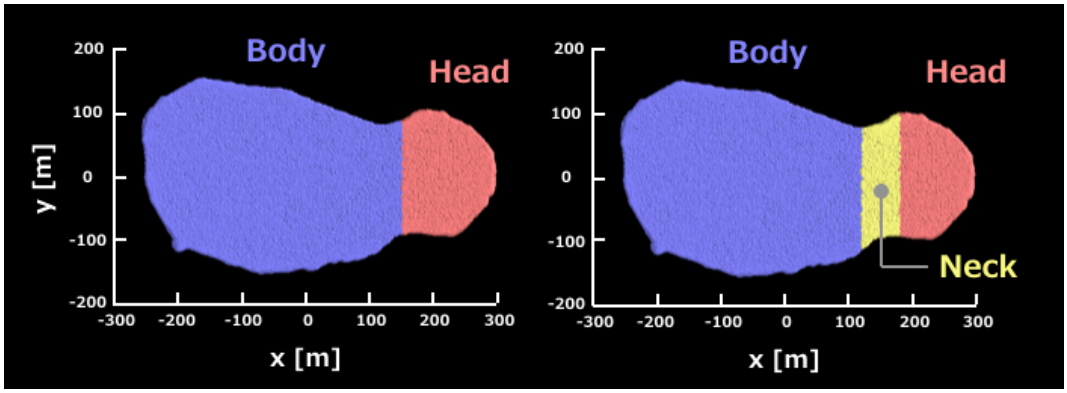

Figure 3.5: Density distributions considered for Itokawa. These images represent a cross-section of the global shape model along the x-y plane viewed from the +z axis. The origin corresponds to the center-of-figure of the shape model. (Left) The geometry of the compressed head model, where the boundary of the two lobes is defined at x = 150 m. For this model. the densities of the body and head are treated as being different. (Right) The geometry for both the second and the third density model, whose neck region is defined between x = 120 to x = 180 m. For the second model, the densities of the two lobes are the same, but different from the neck density. For the third model, the densities of all three components are treated as being different.

3.4 Case of Asteroid Itokawa

3.4.1 Inversion results for Itokawa

For our first inversion in the case of Itokawa, we made use of a simple model where the density of the head portion of the asteroid is different from the body part. We varied the densities of the two lobes and calculated the standard deviations of the dynamic elevations in each of the three region; MUSES-C, Sagamihara and Uchinoura. Given a specific density of the head, the density of the remaining body is uniquely determined using the total mass constraint. Figure 3.6 shows the standard deviations of the smooth terrain elevations as a function of the density of the head of Itokawa. The elevation standard deviations in all three extracted regions are

minimized when the head of Itokawa has a higher density than the mean density 2,020 $\mathrm{kg/m^3}$.

The blue solid line shows the results for the MUSES-C Regio including only the region 1-a to 1-c, whereas the combination of all five regions from 1-a to 1-e is shown with the blue dashed line. Of all investigated regions, the MUSES-C region is the most sensitive to variations in the density distribution, in part because this region is located closer to the mass concentration in the head than the other extracted regions. The elevation standard deviations for the Sagamihara and Uchinoura regions similarly indicated a mass concentration in the head. However, the flatness of the misfit curves shows that these two regions are less sensitive to the density variation in the x-axis direction. For example, whereas the standard deviation for MUSES-C varies from about 2 to 4 meters over the range of investigated values, the misfit for these two regions only varies by less than 0.5 meters. Finally, the black solid line combines all three regions together, which is a weighted average of the misfit values by the area of each region. This shows that the best fitting density of the head is 2,450 $\mathrm{kg/m^3}$, and the corresponding density of the body is 1,930 $\mathrm{kg/m^3}$. This best fitting model corresponds to a center-of-mass/center-of-figure offset of 9.9 meters in the direction of the head.

For our second model, we considered the case where there is a compressed neck between the two lobes of the head and body located between x = 120 to 180 m. For this model, we here consider the case where the two lobes have the same density. Figure 3.7 shows misfit curves using data for the same smooth terrains as

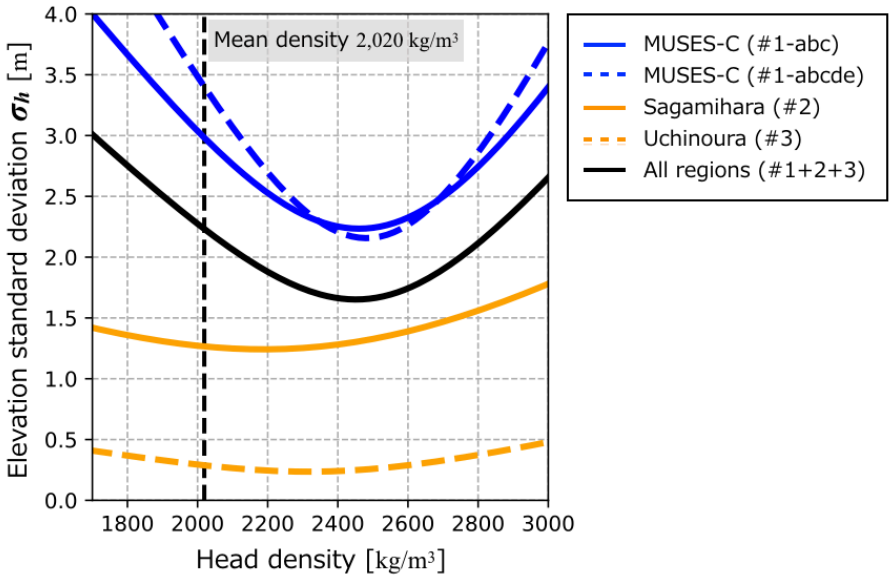

Figure 3.6: Standard deviations of the smooth terrain elevations as a function of the density of the head. The vertical line at 2,020 $\mathrm{kg/m^3}$ corresponds to the mean density of Itokawa. For the best fitting model that combines the three smooth regions (black solid line), the densities of the head and body are 2,450 $\mathrm{kg/m^3}$ and 1,930 $\mathrm{kg/m^3}$, respectively.

investigated in Figure 3.4 as a function of the density of the neck. The best fitting result for each of the three regions implies that the density of the neck is larger than the density of the two lobes.

Analogous to the simulations in Figure 3.6, the misfit is considerably more sensitive for the MUSES-C region than for the other two regions. This is simply because the mass concentration of the neck is closest to the MUSES-C, which is itself adjacent to the small head. The best fitting model that considers all three regions combined has a neck density of 2,660 $\mathrm{kg/m^3}$, whereas the density of the two lobes is 1,960 $\mathrm{kg/m^3}$. We note that the minimum misfit for this mass distribution model is comparable to, but slightly smaller than the previous model that considered only variations in density between the head and body. Based solely on model fitting,

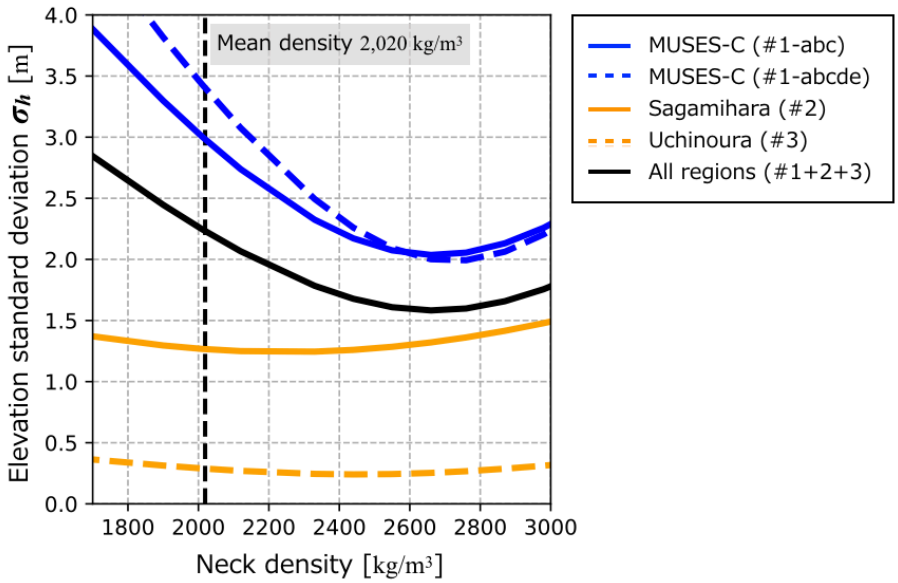

Figure 3.7: Standard deviations of the smooth terrain elevations as a function of the density of the neck. The vertical line at 2,020 $\mathrm{kg/m^3}$ corresponds to the bulk density of Itokawa. We here define the neck region of Itokawa as being located between x = 120 and x = 180 in the asteroid body-fixed frame. For the best fitting model that combines MUSES-C, Sagamihara and Uchinoura (black solid line), the density of the neck is 2,660 $\mathrm{kg/m^3}$ in contrast to a lower density of 1,960 $\mathrm{kg/m^3}$ for the remaining two lobes, the head and body.

the compressed neck model should be favored over the model that considered only different densities for the head and body.

Finally, we consider the case where the densities of the head, neck and body all vary. For these simulations, the density of the neck and head were first chosen, and then the density of the body was computed using the total mass. As there are three parameters that are being varied, we present our results which combine all three smooth terrains together, using 2-dimensional misfit plots in the upper two panels of Figure 3.8. The upper left panel shows the misfit σ_h as a function of the neck and head density, whereas the upper right panel shows the misfit as a function of the body and head density. For these simulations, we used minimum and maximum densities for each region that lie between 1,300 and 3,200 $\mathrm{kg/m^3}$, which corresponds to approximately 60% and 0% porosity, respectively. We also calculated the center-of-mass position of Itokawa using the same density distribution as the upper panels. Figure 3.9 show the center-of-mass/center-of-figure offset of Itokawa in the x-axis direction, Δx. The white crosses denote a uniform density of 2,020 $\mathrm{kg/m^3}$ for every part of Itokawa, whereas the magenta dots represent the density distribution of the minimum misfit at 1,400, 3,200 and 2,000 $\mathrm{kg/m^3}$ for the head, neck and body, respectively. The COM-COF offsets Δx of 21 and 9 meters correspond to the best fit and 1-sigma lower limit independently estimated by Lowry et al. (2014), respectively (see discussion in Section 3.4.3).

These models show that the minimum misfit is obtained when the density of the neck is higher than the average density of Itokawa. The neck density, however, trades

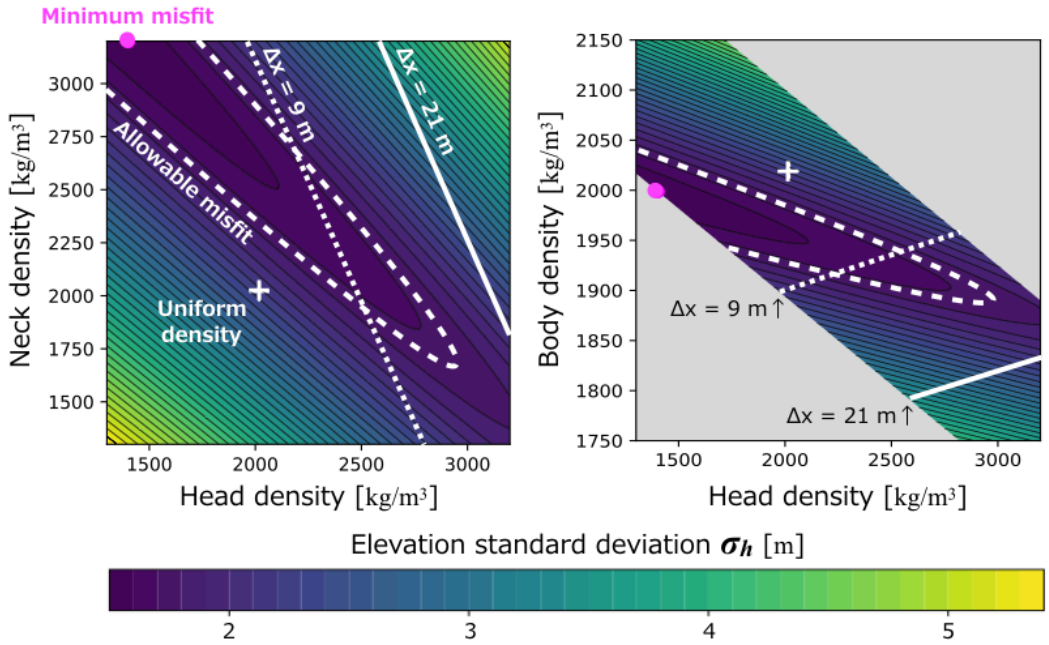

Figure 3.8: Two-dimensional misfit plots for the density model where we allow the densities of the three components of Itokawa to vary. The colors represent the standard deviations of the smooth terrain elevations in meters as a function of the densities of the neck and head (left) and the densities of the body and head (right). Grey regions in the right panels correspond to values that are unallowable given the total mass of the asteroid. White crosses represent the case where all three components have the same density of 2,020 $\mathrm{kg/m^3}$, and the white dashed curves enclose the parameter space allowable for an uncertainty of 0.2 meters. The straight lines denoted by Δx represent the locus of acceptable points for a given center-of-mass/center-of-figure offset in the x-axis direction, where the values of 21 and 9 meters are the best fit and 1-sigma limits of Lowry et al. (2014).

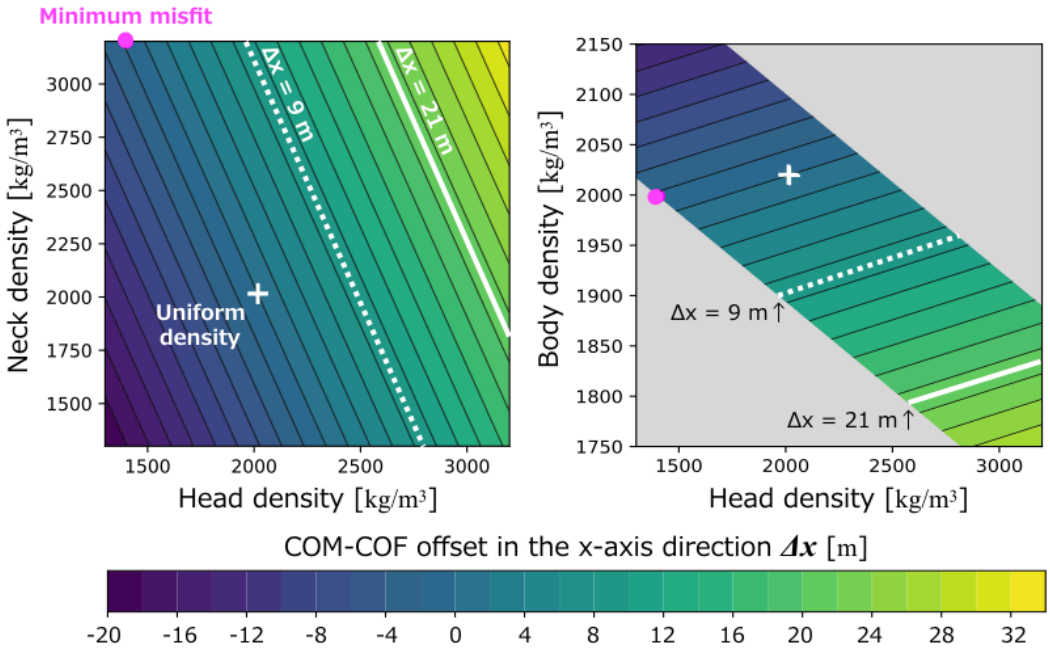

Figure 3.9: The corresponding COM-COF offset Δx in the x-axis direction as a function of the neck and head density (left) and the body and head density (right).

off strongly with the densities of the head and body, but the best fitting value (given our range of investigated densities) is 3,200 $\mathrm{kg/m^3}$. For this value, the density of the head and body are respectively 1,400 an 2,000 $\mathrm{kg/m^3}$. For this model, the minimum misfit is equal to 1.53 m, which is lower than the previous models that considered two variable densities.

The uncertainties of our density estimates are difficult to quantify as the density distribution within Itokawa was assumed *a priori*. The defining boundaries of the head, neck and body are subjective, and different choices would give rise to different inversion results. Nevertheless, a few sources of systematic uncertainty can be assessed. First, the residuals of the shape model estimation is likely to be 0.2 meters (Gaskell et al., 2006). Second, as a result of our mascon approach for calculating

the dynamical heights, these elevations could be uncertain by a maximum of about 1 m, but on average less than 0.17 m in the smooth terrains. Lastly, the smooth terrains are not completely smooth, and do contain isolated boulders that are not easily neglected. Based on our roughness calculations in Table 3.2, the smooth terrains typically have an intrinsic variability less than 0.15 m over 6 meter scales (excluding the small region 1-c).

Based on the above considerations, we will estimate the uncertainty on the inversion parameters by allowing misfits that are 0.2 meters greater than the minimum value (white dashed curves in Figure 3.8). For our inversion that considered separate densities for the head, neck and body, we obtain the following ranges of acceptable densities for each region. For the neck region, densities are constrained to lie between, the maximum value of 3,200 and 1,690 $\mathrm{kg/m^3}$. For the body, densities are tightly constrained to lie between 1,890 and 2,040 $\mathrm{kg/m^3}$. The head density is less constrained and can lie anywhere between the minimum value of 1,300 and about 2,940 $\mathrm{kg/m^3}$. Finally, we note that the COM-COF offset Δx can vary from -5 to 15 meters. Given a density structure model with fewer free parameters, we can more tightly constrain the density of each region. In the compressed head model, we obtained the best fitting density of 2,450 $\mathrm{kg/m^3}$ for the head with an allowable range from 2,220 to 2670 $\mathrm{kg/m^3}$, which are significantly higher than the density for the remaining body part. In the compressed neck model, the allowable range of the neck density is estimated to vary from 2,440 to 2,980 $\mathrm{kg/m^3}$. The inversion results for each density structure model are summarized in Table 3.3.

Table 3.3: Best fitting density in each structure model, the residual misfit of the dynamic elevations and the corresponding center-of-mass/center-of-figure offset (the second to fourth rows). The first row represents a uniform density for all regions of Itokawa. The bottom two rows show density distributions based on the COM-COF offset estimated by Lowry et al. (2014) using $\Delta x = 21 \pm 12$ m. The density ranges in parentheses represents the estimated 1-sigma limits.

Density model	Best fitting density [$\mathrm{kg/m^3}$]			Minimum misfit [m]	COM-COF offset [m]
	Head	Neck	Body	σ_h	Δx
Uniform density	2,020	2,020	2,020	2.23	0.1
Compressed head	2,450 (2,220–2,670)	—	1,930 (1,880–1,980)	1.65 (1.65–1.85)	9.9 (4.7–15.0)
Compressed neck	1,960 (1,930–1,980)	2,660 (2,440–2,980)	1,960 (1,930–1,980)	1.58 (1.58–1.78)	4.5 (3.0–6.7)
Three parts vary	1,400 (1,300–2,940)	3,200 (1,690–3,200)	2,000 (1,890–2,040)	1.53 (1.53–1.73)	−1.6 (−5.4–15.2)
Compressed head (Lowry et al., 2014)	2,930 (2,410–3,460)	—	1,820 (1,710–1,930)	—	21 (9–33)
Compressed neck (Lowry et al., 2014)	1,740 (1,570–1,890)	5,070 (3,320–6,810)	1,740 (1,570–1,890)	—	21 (9–33)

3.4.2 Density, porosity and formation mechanisms

Our inversions that consider only two regions with different densities show that Itokawa has a higher density in either the head or neck region than the average bulk density of the asteroid. For the inversion where the densities of the head and body were varied, the best fitting density of the head was found to be about 2,450 $\mathrm{kg/m^3}$, which is 27% larger than the body. For the inversion where the density of the neck was varied, the best fitting density was found to be about 2,660 $\mathrm{kg/m^3}$, which is 36% larger than the rest of the body. In both cases, the bulk density of the main body was found to be not too different than the average value of the asteroid as the head and neck regions are volumetrically small. Such a density inhomogeneity displaces the center-of-mass (COM) of Itokawa from the center-of-figure (COF) by about 3 to 15 meters (see Table 3.3).

The visible and near-infrared spectra acquired for Itokawa suggests that the composition of the surface is everywhere the same, and this composition is consistent with being composed of LL-chondritic materials that have a grain density of 3,190 $\mathrm{kg/m^3}$ (Abe et al., 2006). The variations in density that we find in our study are thus most easily explained by variations in porosity of a uniform composition asteroid. In the simple density structure model where the head and body have different densities, our best fitting densities of the two lobes correspond to bulk porosities of approximately 23% for the head and about 39% for the body. The porosity of about 20% for the head is representative of a coherent asteroid such as asteroid Eros, which is mildly fractured but is a strength-dominated structure (Wilkison et al.,

2002). On the other hand, the porosity of about 40% for the body is commonly observed for a porous structure of rubble-piles or gravitational aggregates. The head of Itokawa thus may have a more coherent and monolithic structure than the body. As evidence for this, an area of steep slope of approximately 40 degrees is located near the head and neck, and is considered to be bedrock that is exposed on the surface (Barnouin-Jha et al., 2008).

For our model that allows all three regions to vary in density, the neck density is always found to be considerably greater than the head and body. For our assumed geometry of the neck, the density of the neck is constrained to lie between 3,200 and 1,690 $\mathrm{kg/m^3}$, which corresponds to 0% to 47% porosity. This model allows a large range of possible solutions, and will be interpreted separately in the following section that employs additional independent constraints on the COM-COF offset of Itokawa.

There are several possible interpretations of our inversion results that bear on the origin and evolution of asteroid Itokawa. One model that fits the data has equal densities for the head and body, and a compressed density of the neck. This scenario would be consistent with both the head and body having formed from the same materials and with the same initial bulk porosities. The higher density of the neck region in this model is simply the result of the two bodies colliding and compacting the material at the interface between the two lobes. The impact of porous asteroids has been modeled by Davison et al. (2010). Though they do not report the final porosities of their simulations, they did find that significant heating can occur at

the impact point as a result of the compaction of porosity. This compaction related heating was limited to a small region comparable in size to the neck in our models. In contrast, impact simulations by Jutzi and Benz (2017) that involve disruption and subsequent accumulation into a bi-lobed object with a low relative velocity predict that the porosity should decrease with depth within each pre-impact lobe. The connecting neck in their model would have a slightly lower density (and higher porosity) than the average value, which is inconsistent with our findings.

A second model that fits the data equally well is the case where the small head has a higher density (and lower porosity) than the body. Such a situation could arise in two ways. One possibility is that the head is simply a coherent block of material initially derived from a larger parent body, and that the body is a rubble pile asteroid formed by catastrophic disruption and re-accumulation. In this scenario, the head would represent a more pristine object that has undergone less processing by impacts and that later accreted to the main body. Alternatively, it is possible that the impact of the body and head compacted the porosity out of both the head and neck region. Given that the body is considerably larger in size, its initial porosity far from the impact point would have been relatively unaffected by the impact.

Asteroid 1999 KW4 is an interesting target for understanding dynamics of a binary system, which may be applicable to interpreting our results for Itokawa. This object is a binary system, where the main body has a size of 1.32 km and the satellite has a smaller size of 0.45 km. From constraints on the orbital motion and shape modeling of each component based on ground-based radar observations by Ostro

et al. (2006) and Scheeres et al. (2006), the density of the primary is constrained to be 1,970 (1,730–2,210) $\mathrm{kg/m^3}$, whereas the density of the satellite is found to have a higher density of 2,810 (2,180–3,630) $\mathrm{kg/m^3}$. The density difference between the two lobes of Itokawa inferred in this study can be explained by an eventual collapse of a binary system similar to that of 1999 KW4 (Scheeres et al., 2007; Scheeres and Gaskell, 2008). It remains to be seen if the density of the satellite of other binary systems is larger than the density of the primary object.

3.4.3 Comparison with YORP spin-up observations

The detection of a YORP spin-up/down of an asteroid can be used to model the large-scale density distribution in the body. The YORP effect is the change of the rotation rate of an irregularly shaped body that results from the torques related to the solar radiation and thermal emission (Rubincam, 2000). The YORP effect on an asteroid was initially observed as an increase in spin rate for a near-Earth asteroid, 54509 YORP (2000 PH5) (Lowry et al., 2007; Taylor et al., 2007). The magnitude of this effect is sensitive to the interior density heterogeneity or the COM-COF offset of the body as well as its shape and optical properties (Scheeres and Gaskell, 2008). Based on the current shape model and rotation pole for Itokawa, a simulation of the YORP effect predicts that the rotation rate of Itokawa should be decelerating (Scheeres et al., 2007). However, Lowry et al. (2014) detected an acceleration of Itokawa's rotation and estimated the COM-COF offset to be $\Delta r = 14 \pm 7$ m in the x-y plane or $\Delta x = 21 \pm 12$ m if the offset is assumed to be in the direction of

the x axis. Given the symmetrical density structures investigated in our study, the COM-COF offset in the direction of the y axis for our models is always less than 0.5 meters for an arbitrary density distribution. Therefore, we will consider only the Δx offset as reported by Lowry et al. (2014).

To explain the observed YORP spin-up, Lowry et al. (2014) proposed two types of density distributions in Itokawa. Their models are similar to ours where the density of the head is higher than that for the body, or where there exists a compressed neck region. Using their Δx estimate along with our shape model based on Gaskell et al. (2006), the COM-COF offset of 21 ± 12 m corresponds to a density of 2,930 (2,410 to 3,460) $\mathrm{kg/m^3}$ for the head and 1,820 (1,930 to 1,710) $\mathrm{kg/m^3}$ for the body (see Table 3.3). Our best fitting densities and our predicted COM-COF offset of 9.9 m in the compressed head model is within the uncertainty of their estimation. Our model where the density of the neck differs from the rest of the asteroid is less consistent with the COM-COF offset of Lowry et al. (2014). In particular, our best fitting model gives an offset of only 4.5 m, with a 1-sigma upper limit of 6.7 m, which is only marginally consistent with the 1-sigma lower limit of $\Delta x = 9$ m from Lowry et al. (2014).

We next use the COM-COF offset of Lowry et al. (2014) to constrain our inversion that considered separate densities for the head, neck and body. We noted previously that this inversion provided a wide range of possibilities as a result of trade-offs between the three densities. As previously discussed, Figure 3.8 plots our misfit as a function of the density of the three components. The white dashed curve gives

our estimate of the 1-sigma uncertainty, showing that there is a strong correlation between the density of the head and neck. In this same plot, we plot solid and dotted white lines corresponding the best fit and 1-sigma lower limit of the Lowry et al. (2014) COM-COF offset. This shows that there is only a small region of the parameter space that overlaps at the 1-sigma level. In particular, the two techniques constrain the density of the head to lie between 2,200 and 2,940 $\mathrm{kg/m^3}$, which is always greater than the average density of the asteroid. The density of the neck is constrained to lie between 1,690 and 2,650 $\mathrm{kg/m^3}$, allowing for either moderate compaction of the neck region, or even a moderate increase in porosity. The density of the body is well constrained between the limits of 1,890 and 1,940 $\mathrm{kg/m^3}$, which is slightly lower than the mean bulk density of 2,020 $\mathrm{kg/m^3}$ in this study. Thus, the best constrained result using both techniques is that the head of Itokawa has a higher density than the rest of the asteroid.

3.5 Case of Comet 67P

The comet 67P/Churyumov-Gerasimenko is another great target of our density distribution estimation technique. This comet was visited by the European spacecraft Rosetta. The comet nucleus of 67P has a bilobed shape and a smooth region called Hapi as shown in Figure 3.10.

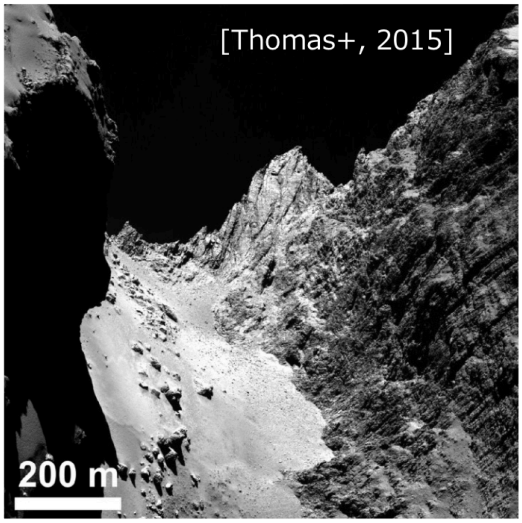

Figure 3.10: The smooth Hapi region is located between the two lobes, surrounded by steep cliffs and covered with finer particles.

3.5.1 Smooth terrain mapping

We utilized a shape model of 67P developed by Gaskell et al. (2017). The original shape model has 96,834 surface elements. We generated volume elements within the polyhedral shape model using a tetrahedral mesh generator, TetGen (Hang, 2018). As the original surface meshes were preserved, 218,266 volume elements were generated. Table 3.4 summarizes the number of elements and their average size.

Table 3.4: Shape model statistics used in the case of 67P. The Gaskell's shape model was re-meshed by TetGen mesh generator (Hang, 2018). N_S and N_V denote the number of volume elements and surface elements, respectively. $\bar{D}_S$ denotes the mean diameter of a circle of equivalent area of the surface elements and $\bar{D}_V$ denotes the mean diameter of a sphere of equivalent volume of the volume elements.

	N_S	$\bar{D}_S$ [m]	N_V	$\bar{D}_V$ [m]
Original	96,834	24.8	—-	—-
Meshed shape	96,834	24.8	218,266	36.9

We identified the smooth terrain on 67P based on the roughness parameter because of difficulties in image projection onto the shape model (lack of geometric information of positions and sight directions corresponding to the specific version of the shape model). We calculated the roughness parameters as the previous definition in Section 3.3.1. Figure 3.11 shows the distribution of 40-, 60- and 80-meter scale roughness around the Hapi region. We extracted the geometry of meshes inside the boundary of the smooth area as shown by the magenta lines.

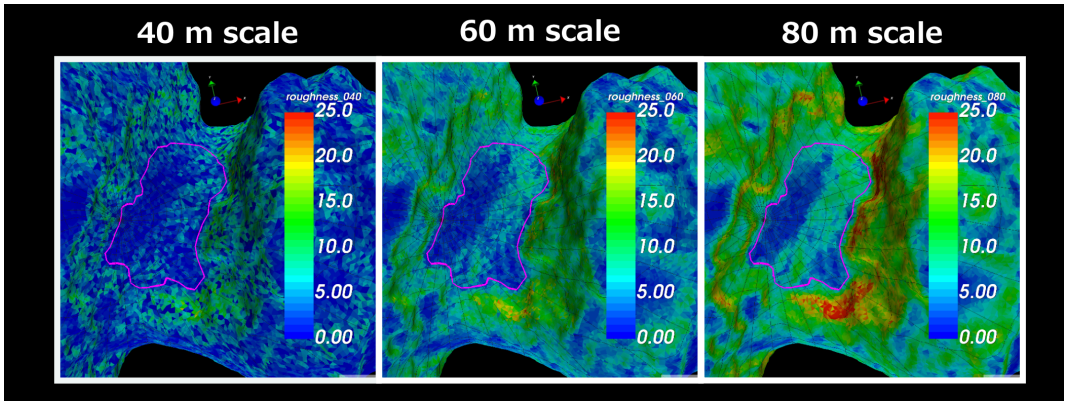

Figure 3.11: Roughness map to identify the boundary of the smooth region, Hapi. Three panels show roughness parameters in 40-, 60- and 80-meter scales, respectively.

We hereby assumed a density map shown in Figure 3.12. We divided the 67P nucleus into three parts: the smaller lobe "head", the bigger lobe "body" and the concave area between two lobes "neck", and then densities of the three parts were varied so that the total mass of the nucleus is constant. We assumed that the thickness of the neck was 300 meters along to an axis which was rotated by -34 degrees around the z-axis of the shape model.

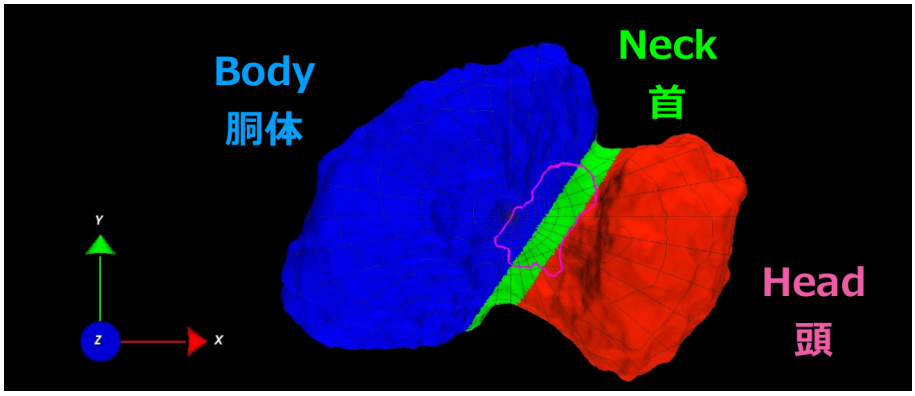

Figure 3.12: Density map assigned for comet 67P/Churyumov-Gerasimenko. The thickness of the neck part is hereby assumed to be 300 meters.

3.5.2 Inversion results for 67P

We calculated the misfit criteria or the standard deviation of the dynamic elevations in the Hapi region as a function of densities of the head, neck and body. The white crosses in Figure 3.13 denote the homogeneous density distribution where the density of every part of the nucleus is equal to the mean bulk density 532 $\mathrm{kg/m^3}$. The magenta dots denote the best fitting density to minimize the discrepancy between the smooth region and an equi-potential surface. In contrast to the case of Itokawa, the homogeneous structure and the best fitting density agree very well with each other. Given a similar density with the mean bulk density to the two lobes, the Hapi region approaches to a single equi-potential surface. On the other hand, our misfit criteria is less sensitive to the neck density.

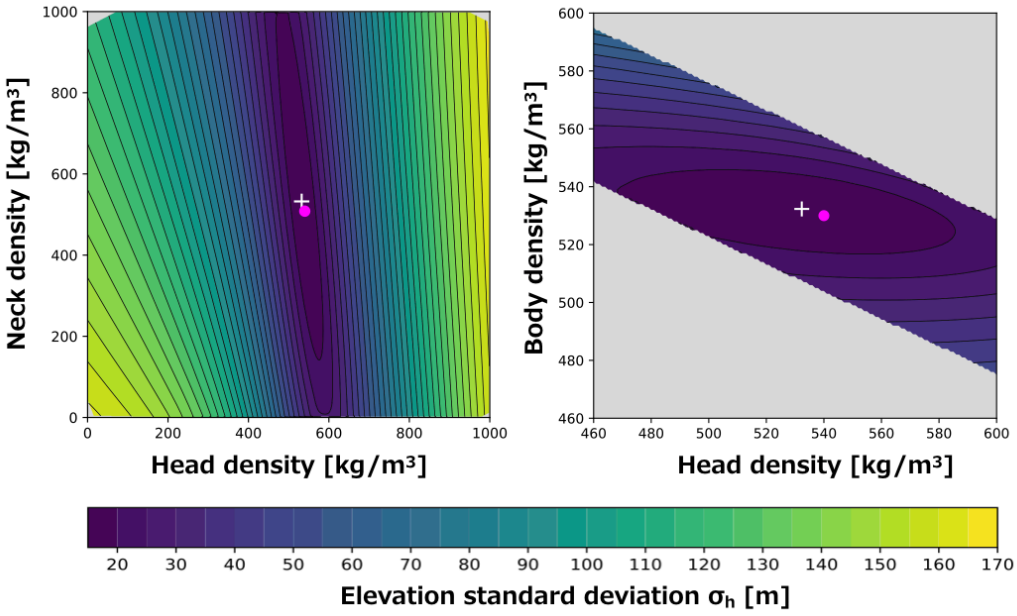

Figure 3.13: The misfit criteria in Hapi as a function of the densities of the head, neck and body of 67P nucleus. The white crosses and magenta dots denote the constant density distribution over the nucleus and the best fitting density, respectively.

3.5.3 Implications for the structure and formation

For 67P nucleus, the misfit criteria at Hapi was minimized when the two lobes have the same density (Figure 3.13). This homogeneous density distribution is consistent with the gravity harmonic coefficients observed up to the second degree and order, derived from the tracking data of the Rosetta spacecraft at a distance of 100 km to 10 km (Pätzold et al., 2016). They report that these observed coefficients agree well with the simulated coefficients within the error range, which are calculated from shape models assuming a constant density.

Figure 3.14 visualizes the equi-potential surface with the cross section of the comet nuclei. The cross section is displayed on the z-x plane rotated by -20 degrees around the z-axis of the shape model. The Hapi region is enlarged and displayed in

the right panel. The gravitational potential was derived from the mascon technique with a constant density assumption and combined with the centrifugal potential corresponding to the rotation period of 12.4 hours. The Hapi region well approximates the equi-potential surface even if there is no density variation. If one lobe has a higher density than another, the equi-potential surface can't help being inclined against the surface of the smooth terrain.

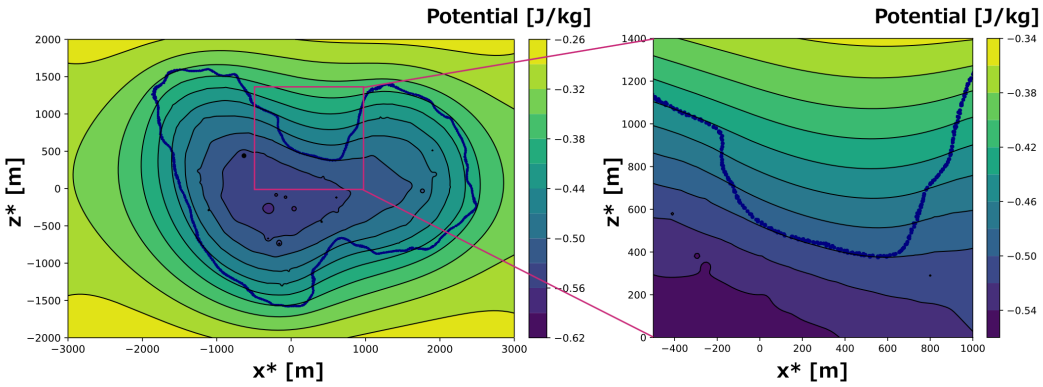

Figure 3.14: Comparison between the equi-potential surface and the shape of 67P nucleus. The cross section is displayed on the z*-x* plane, which rotates the z-x plane of the shape model by -20 degrees around the z-axis. The right panel magnifies the Hapi region.

How can a bilobed shape nucleus with the same density be created? A possible formation mechanism is proposed as "sub-catastrophic" disruption and subsequent re-accumulation (Jutzi and Benz, 2017). In this scenario, an ellipsoidal icy planetesimal is broken into two parts by a lower-energy collision than a catastrophic disruption, and afterward they collide into each other to merge by the self-gravity. Another explanation is that the shape and homogeneous structure of 67P were formed as a result of anisotropic sublimation and mass loss (Vavilov et al., 2019). This scenario requires a positive feedback to excavate the neck region.

3.6 Conclusion

This study developed a technique to estimate the interior density distribution within the asteroid Itokawa based on the elevations of the smooth terrains with respect to an equi-potential surface. By changing the interior density distribution, we searched for solutions that made these surfaces as flat as possible. This study indicates that Itokawa has an important density heterogeneity between the two lobes, where the head is found to have a higher density than the body. Models with a compressed neck can also fit the data, but are not required when considering the independent COM-COF offset inferred from the observed YORP spin-up of the asteroid by Lowry et al. (2014). Our results imply that the head has a lower porosity than the remainder of the body (23% vs. 39%). This could arise either if the head is composed of a coherent block of material derived from a larger parent body, or if a portion of the porosity of the head was compacted out when the head and body collided to form the presently observed asteroid.

Our technique of using smooth terrains to constrain the density distribution in a small body can be applied to investigate any arbitrary density distribution such as the presence of a central core-like structure with a lower porosity at the center of an asteroid. Additionally, this technique can be applied to any irregularly shaped small body which possesses a flat region that could be approximated as the equi-potential surface. Possible small bodies that could be investigated include Comet 103P/Hartley 2 as well as Ultima Thule (the Kuiper Belt object officially named 2014

MU69). Given that the outflow of volatile materials should erode the topography of a comet nucleus towards an equi-potential surface, this type of analysis could be effective for estimating the density distribution and bulk density of comets as well. Both Hartley 2 and 67P/C-G have two-lobe structures and smooth surface areas are observed in their neck regions connecting the two lobes (A'Hearn et al., 2011; Thomas et al., 2015). The bulk density of Hartley 2 has been estimated to be approximately 200 to 400 $\mathrm{kg/m^3}$ by minimizing the difference between their observed shape and a global equi-potential surface (Richardson and Bowling, 2014; Thomas et al., 2013). Our estimation technique will be a useful for constraining the effects of collisions in the asteroid belt and can be used as constraints for impact simulations of porous planetesimals. Improved modeling of collisions in the asteroid belt are required to better understand how the collisions affect the porosities of the bodies.

Appendix A

Parameters of Small Bodies

We hereby summarize orbital elements and physical properties of small bodies necessary for our numerical simulations.

Table A.1: Orbital elements and physical parameters of asteroid 433 Eros (Miller et al., 2002).

Parameter	Notation	Value	Unit
Orbital elements			
Semi-major axis	a	1.458112258549551	AU
Eccentricity	e	0.2227357205256897	–
Inclination	I	10.82856732664407	deg
Lon. of the ascending node	Ω	304.3062624764607	deg
Argument of perihelion	ω	178.8213598069167	deg
Time of perihelion passage	t_p	2458516.110717880348	sec
		(2019-Feb-01.61071788)	
Rotation pole			
Right ascension (RA)	α	11.3692 ± 0.003	deg
Declination (Dec)	δ	17.2273 ± 0.006	deg
Ecliptic longitude	λ	17.24	deg
Ecliptic latitude	β	11.35	deg
Obliquity	ε	85.48	deg
Rotation period	P	5.270	hours
Physical properties			
GM	GM	$(4.4631 \pm 0.0003) \times 10^5$	$\mathrm{m}^3/\mathrm{s}^2$
Mass	M	$(6.6904 \pm 0.003) \times 10^{15}$	kg

Table A.2: Properties of asteroid 25143 Itokawa (Abe et al., 2006; Demura et al., 2006). See also JPL Small-Body Database (https://ssd.jpl.nasa.gov/sbdb.cgi?sstr=2025143).

Parameter	Notation	Value	Unit
Orbital elements			
Semi-major axis	a	1.324142657689103	AU
Eccentricity	e	0.2801450933746131	–
Inclination	I	1.621354096841838	deg
Lon. of the ascending node	Ω	69.08061990311242	deg
Argument of perihelion	ω	162.824299065736	deg
Time of perihelion passage	t_p	2458710.454172357169	sec
		(2019-Aug-14.95417236)	
Rotation pole			
Right ascension (RA)	α	90.53	deg
Declination (Dec)	δ	-66.30	deg
Ecliptic longitude	λ	128.5	deg
Ecliptic latitude	β	-89.66	deg
Obliquity	ε	178.5	deg
Rotation period	P	12.1324	hours
Physical properties			
GM	GM	2.39 ± 0.12	$\mathrm{m}^3/\mathrm{s}^2$
Mass	M	3.58×10^{10}	kg

Table A.3: Properties of asteroid 162173 Ryugu published by Watanabe et al. (2019).

Parameter	Notation	Value	Unit
Orbital elements			
Semi-major axis	a	1.18956373	AU
Eccentricity	e	0.190279210	–
Inclination	I	5.8840222	deg
Lon. of the ascending node	Ω	251.589203	deg
Argument of perihelion	ω	211.435963	deg
Time of perihelion passage	t_p	-142941729.4	sec
Rotation pole			
Right ascension (RA)	α	96.40	deg
Declination (Dec)	δ	-66.40	deg
Ecliptic longitude	λ	179.3	deg
Ecliptic latitude	β	-87.44	deg
Obliquity	ε	171.64 ± 0.03	deg
Rotation period	P	7.63262	hours
Physical properties			
GM	GM	30.0	$\mathrm{m}^3/\mathrm{s}^2$
Mass	M	4.50×10^{11}	kg
Volume	V	0.377 ± 0.005	km^3
Density	ρ	$1{,}190 \pm 20$	kg/m^3

Appendix B

Shape models

B.1 Shape Model List

We hereby list shape models of small bodies and their fundamental property available for our study.

Table B.1: Shape models of asteroid Itokawa.

$N_{node}^{orig.}$	$N_{facet}^{orig.}$	N_{node}	N_V	N_S
Gaskell's shapes				
25,350	49,152	–	–	–
99,846	196,608	–	–	–
396,294	786,432	–	–	–
1,579,014	3,145,728	–	–	–
Re-meshed models by NetGen				
25,350	49,152	5,928	25,136	6,158
25,350	49,152	21,777	79,855	30,228
25,350	49,152	26,068	125,578	18,014
25,350	49,152	417,708	2,410,174	123,194
396,294	786,432	64,161	282,987	60,774
396,294	786,432	221,165	1,083,253	142,252
396,294	786,432	325,686	1,693,335	149,062
396,294	786,432	655,144	3,613,429	173,974
Re-meshed models by TetGen				
25,350	49,152	32,759	124,232	49,152
396,294	786,432	2,166,444	8,387,333	3,145,728

Table B.2: Shape models of asteroid Eros.

$N_{node}^{orig.}$	$N_{facet}^{orig.}$	N_{node}	N_V	N_S
Gaskell's shapes				
25,350	49,152	–	–	–
99,846	196,608	–	–	–
396,294	786,432	–	–	–
1,579,014	3,145,728	–	–	–
Re-meshed models by Netgen				
25,350	49,152	1,926	5,982	3,096
25,350	49,152	3,231	11,973	4,320
25,350	49,152	6,657	29,457	6,178
25,350	49,152	35,889	177,736	21,790
25,350	49,152	360,152	1,918,949	129,142
396,294	786,432	5,627	18,161	8,722
396,294	786,432	11,015	42,620	13,730
396,294	786,432	26,039	118,639	22,240
396,294	786,432	51,755	262,070	27,400
396,294	786,432	59,474	266,646	54,108
396,294	786,432	71,476	405,700	27,250
396,294	786,432	114,199	571,411	65,386
396,294	786,432	121,105	648,275	39,046
396,294	786,432	196,489	1,091,433	38,792
396,294	786,432	440,788	2,418,982	109,948
396,294	786,432	984,609	5,292,246	322,392

Table B.3: Shape models of comet 67P/C-G.

$N_{node}^{orig.}$	$N_{facet}^{orig.}$	N_{node}	N_V	N_S
Gaskell's shapes				
48,420	96,834	–	–	–
99,729	199,452	–	–	–
Re-meshed models by TetGen				
48,420	96,834	61,265	218,266	96,834
99,729	199,452	–	–	–

Table B.4: Shape models of asteroid Ryugu used for our simulation. A small model in low resolution was made from the 49k-mesh SfM model (ver. 2018-08-10). N_{node} and N_S represent the number of nodes and surface facets. V, S and $\bar{D}_S$ denote volume, surface area and mean size of the surface facets, respectively.

N_{node}	N_S	V [m^3]	S [m^2]	$\bar{D}_S$ [m]
SPC (ver. 2018-08-10)				
25,350	49,152	377701692	2688669	8.283114
99,846	196,608	377802710	2698353	4.148179
396,294	786,432	377828987	2703868	2.075907
1,579,014	3,145,728	377836719	2706728	1.03834
SPC (ver. 2019-08-02)				
25,350	49,152	379443541	2738452	8.388575
99,846	196,608	379539619	2758166	4.20877
396,294	786,432	379566067	2769083	2.108326
1,579,014	3,145,728	379573215	2773579	1.05495
SfM (ver. 2018-08-04)				
25,350	49,152	377266831	2741014	8.378159
99,846	196,608	377387744	2768265	4.206988
396,294	786,432	377419583	2783201	2.107751
1,579,014	3,145,728	377427307	2789137	1.054437
SfM (ver. 2019-01-30)				
23,439	46,874	379241142	2742611	8.411322
93,752	187,500	379308711	2764458	4.235453
375,002	750,000	379329116	2777895	2.123263
1,500,002	3,000,000	379332856	2782221	1.064302
2,896,191	5,792,378	379332611	2782703	0.7497634
Small model for test				
2,976	5,932	376881305	2697490	23.7

Appendix C

Supplementary Materials of YORP

To validate our calculation code of the YORP effect, we demonstrated simulation using shapes of small bodies other than asteroid Ryugu and compared them with results of previous studies.

C.1 Asteroid 433 Eros

We simulated the YORP effect on asteroid 433 Eros. The orbital elements, the spin parameters and other physical parameters used for this simulation is listed in Table A.1. We utilized the Gaskell's shape model in resolution of 49,152 to 3,145,728 surface meshes and another two models of 3,968 and 8,370 meshes, downsized from the 49,152-mesh model. We calculated the thermal torque on Eros at 264-second intervals, which correspond to 1/72 of 5.27-hours rotation period, over a whole cycle of the orbital period of 643 Earth-days (totally 210,872 steps). Daily and seasonal variation in thermal torque on Eros are presented in Figure C.1

and C.2, respectively. Table C.1 shows the year-averaged torque for each resolution of the shape models.

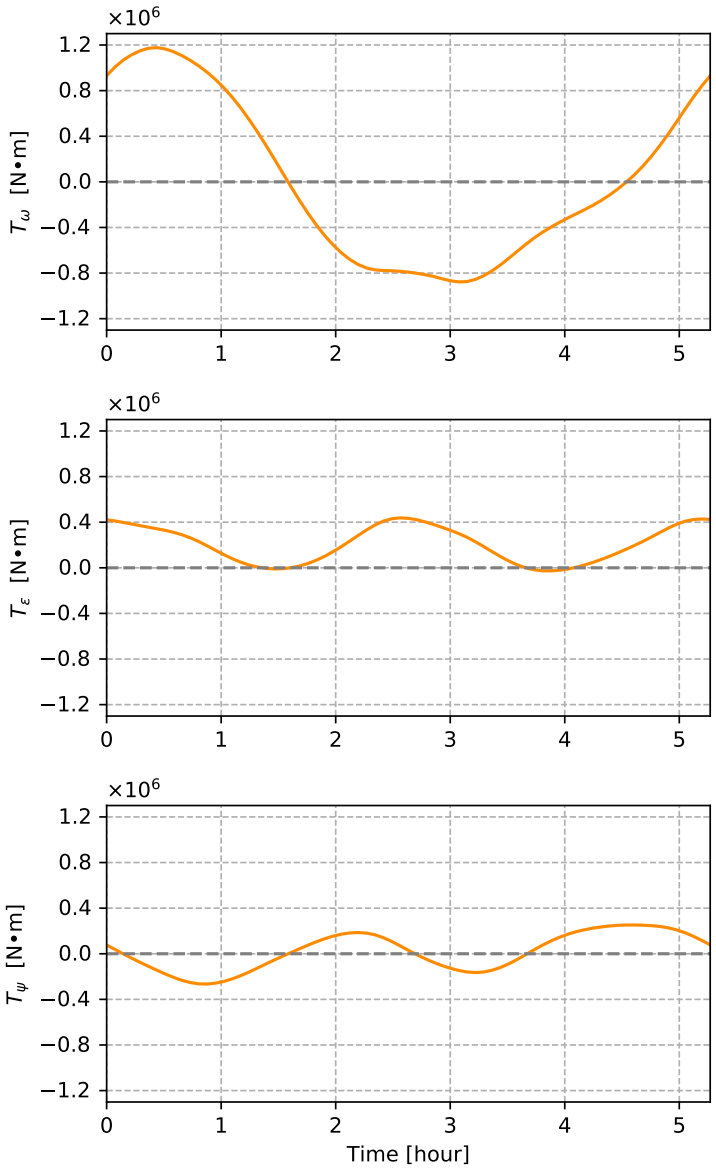

Figure C.1: Time variation in the thermal torque over a cycle of the rotation (Eros' rotation period $P \sim 5.27$ hours). Three panels indicate the each component of the torque as function of time in hour: (*upper*) the component parallel to the spin pole τ_ω increasing or decreasing the spin rate, (*middle*) the component tilting the spin pole τ_ε, and (*bottom*) the component exciting the precession. The 3D shape model of Eros used in this simulation was the Gaskell's model of 49,152 meshes.

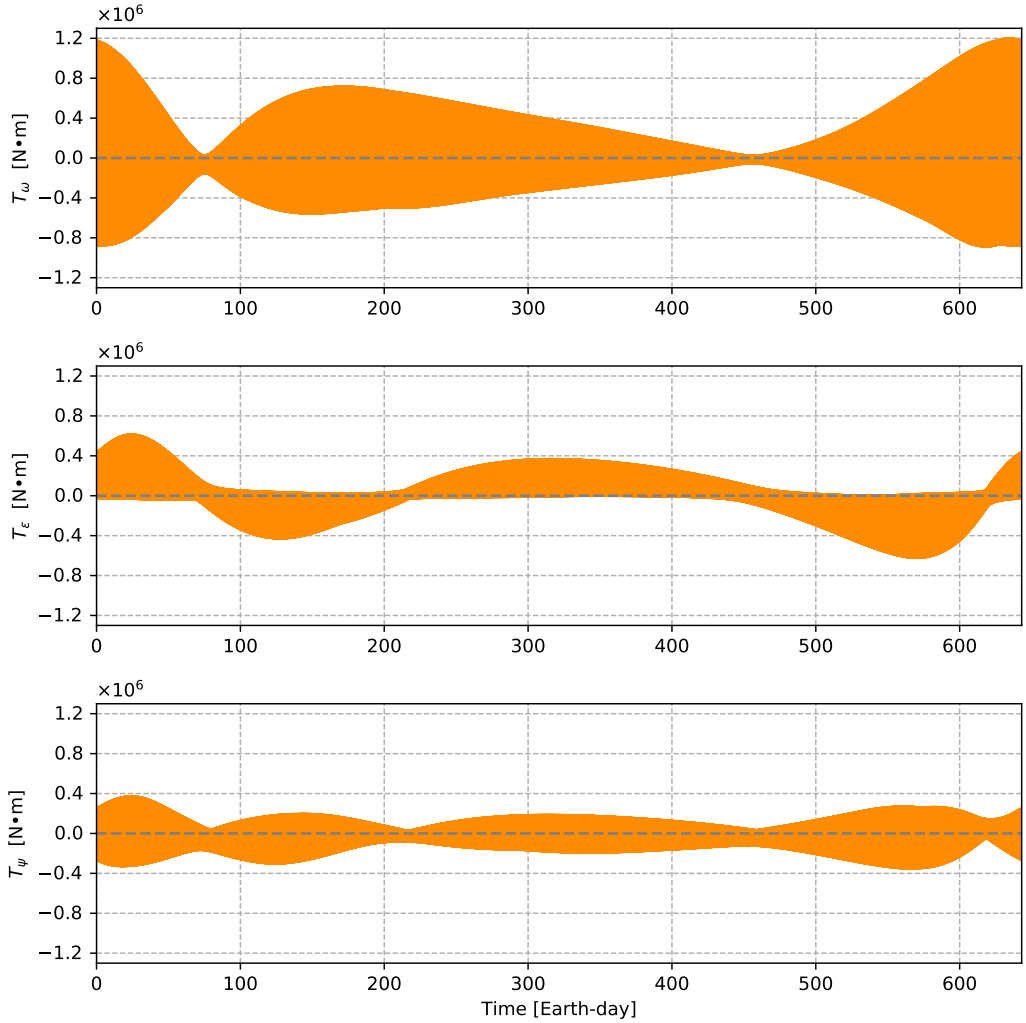

Figure C.2: Seasonal variation in the components of the YORP torque $\boldsymbol{\tau}(\tau_\omega, \tau_\varepsilon, \tau_\psi)$ over a cycle of the revolution (Orbital period of Eros ~ 643 Earth-days). The same SPC model with Figure C.1 was used in this simulation.

Table C.1: Mean YORP torque $\bar{\tau}$ on asteroid Eros and the corresponding YORP time scales. Smaller shape models are derived from the 49,152-mesh model.

N_S	$\bar{\tau}_\omega$ [N · m]	$\bar{\tau}_\varepsilon$ [N · m]	$\bar{\tau}_\psi$ [N · m]	$\frac{d\omega}{dt}$ [deg/sec/Myr]	$\frac{d\varepsilon}{dt}$ [deg/Myr]	$\frac{d\psi}{dt}$ [deg/Myr]	t_{halve} [Myr]	State
Small models for test								
3,968	−7,627	889.6	−15,41	-2.782×10^{-5}	9.797×10^{-3}	−0.1698	341.1	**Spin-down**
8,370	−7,595	876.5	−15,18	-2.764×10^{-5}	9.630×10^{-3}	−0.1668	343.3	**Spin-down**
Gaskell's shape								
49,152	−6,952	791.8	−14,97	-2.526×10^{-5}	8.687×10^{-3}	−0.1643	375.6	**Spin-down**
196,608	−6,632	756.8	−14,58	-2.409×10^{-5}	8.300×10^{-3}	−0.1600	393.8	**Spin-down**
786,432	−6,630	757.9	−14,32	-2.408×10^{-5}	8.312×10^{-3}	−0.1571	394.0	**Spin-down**
3,145,728	−6,693	765.7	−14,19	-2.431×10^{-5}	8.397×10^{-3}	−0.1556	390.3	**Spin-down**

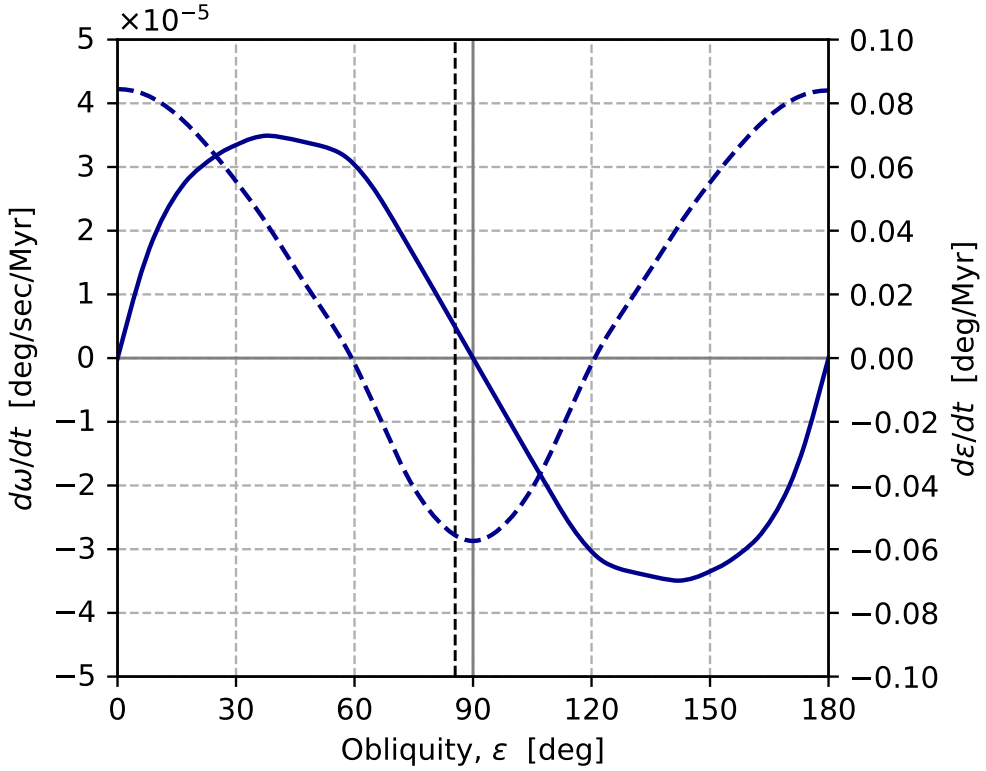

Figure C.3: The YORP effect on asteroid Eros depending on obliquity in the same manner as Figure 2.4. According to Equation 2.13, ε-related torque is hereby converted into the amount of change in ε using the current spin rate of Eros. The vertical dashed line presents the nominal obliquity observed by NEAR-Shoemaker ($\varepsilon = 85.48°$).

C.2 Asteroid 25143 Itokawa

We hereby show the results of YORP simulation for asteroid Itokawa. The orbital elements, the spin parameters and other physical parameters used for this simulation is listed in Table A.2. Each time step of the simulation corresponds to 607 seconds, that is, 1/72 of 12.1324 hour period. We utilized the Gaskell's shape

model in resolution of 49,152 to 3,145,728 surface meshes and another two models downsized from the 49,152-mesh model (Gaskell et al., 2006). Figure C.4 and C.5 present time variation in thermal torque over the cycles of 12.1324-hours rotation period and 557-days orbital period (totally 79,268 time steps). Table C.2 shows the year-averaged torque for each resolution of the shape models.

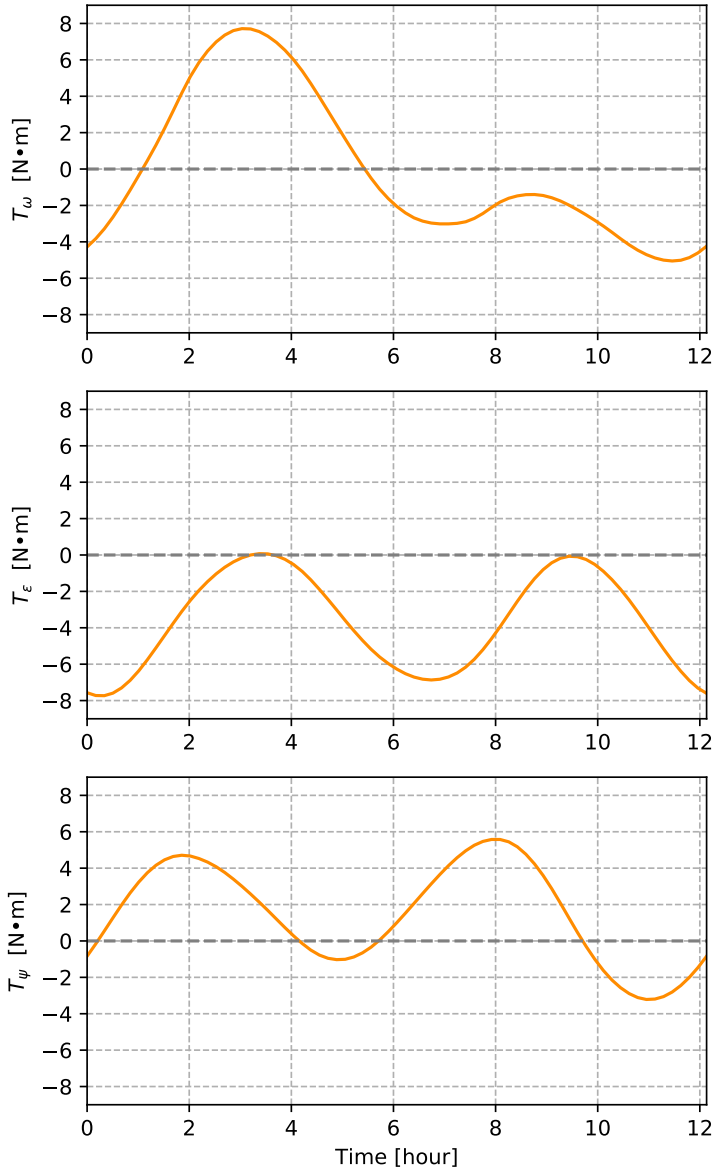

Figure C.4: Time variation in the thermal torque over a cycle of the rotation (Itokawa' rotation period $P = 12.1324$ hours). Three panels indicate the each component of the torque as function of time in hour: (*upper*) the component parallel to the spin pole τ_ω increasing or decreasing the spin rate, (*middle*) the component tilting the spin pole τ_ε, and (*bottom*) the component exciting the precession. The 3D shape model of Eros used in this simulation was the Gaskell's model of 49,152 meshes.

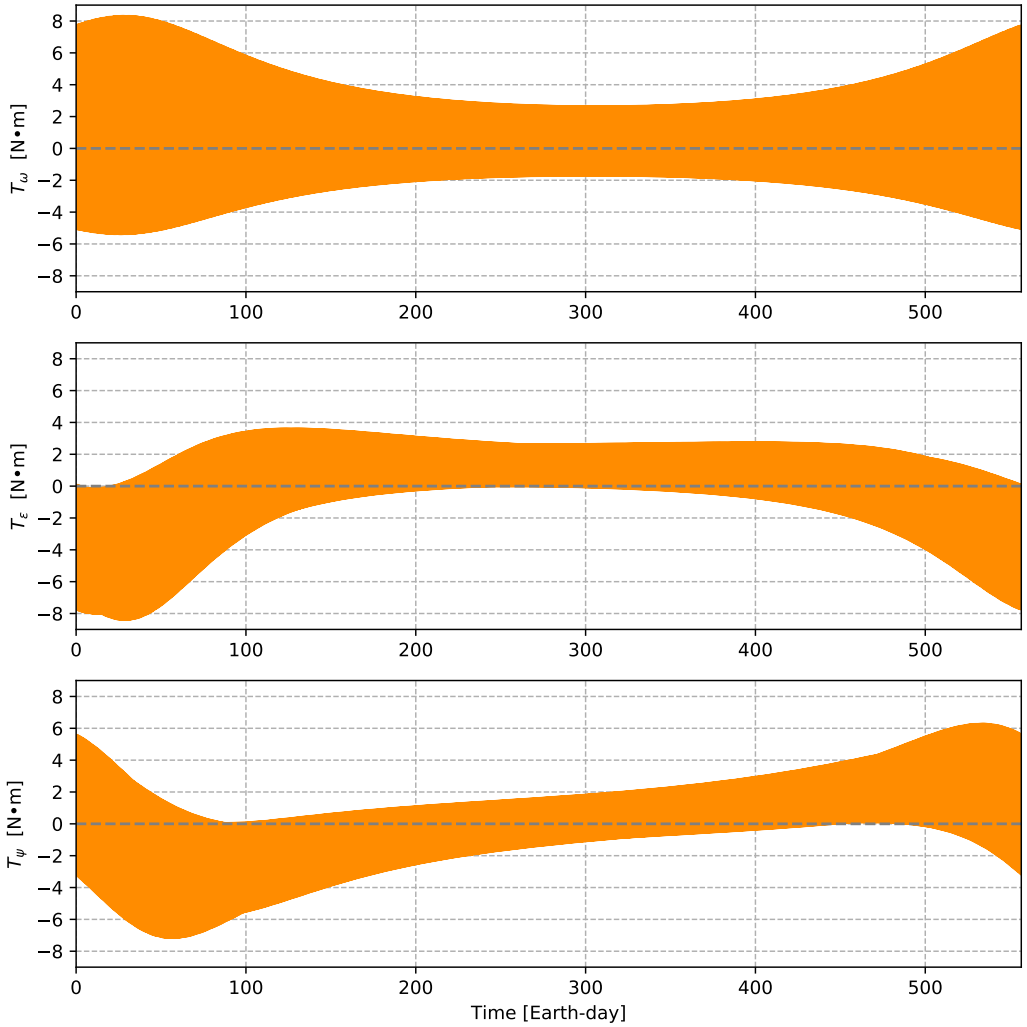

Figure C.5: Seasonal variation in the components of the YORP torque $\boldsymbol{\tau}(\tau_\omega, \tau_\varepsilon, \tau_\psi)$ over a cycle of the revolution (Orbital period of Itokawa $\sim$ 557 Earth-days). The same SPC model with Figure C.4 was used in this simulation.

Table C.2: Mean YORP torque $\bar{\tau}$ on asteroid Itokawa and the corresponding YORP time scales. Smaller shape models are derived from the 49,152-mesh model.

N_S	$\bar{\tau}_\omega$ [N · m]	$\bar{\tau}_\varepsilon$ [N · m]	$\bar{\tau}_\psi$ [N · m]	$\frac{d\omega}{dt}$ [deg/sec/Myr]	$\frac{d\varepsilon}{dt}$ [deg/Myr]	$\frac{d\psi}{dt}$ [deg/Myr]	t_{halve} [Myr]	State
Small models for test								
5,430	−0.009278	−0.002987	0.05801	−0.02089	−46.74	907.8	0.1973	**Spin-down**
9,092	−0.006060	−0.003373	0.05697	−0.01363	−52.72	890.6	0.3024	**Spin-down**
Gaskell's shape								
49,152	−0.01646	−0.002637	0.05773	−0.03699	−41.18	901.5	0.1114	**Spin-down**
196,608	−0.01518	−0.002691	0.05784	−0.03425	−42.22	907.5	0.1203	**Spin-down**
786,432	−0.01591	−0.002629	0.05822	−0.03594	−41.28	914.0	0.1147	**Spin-down**
3,145,728	−0.01964	−0.002403	0.05856	−0.04436	−37.73	919.3	0.09291	**Spin-down**

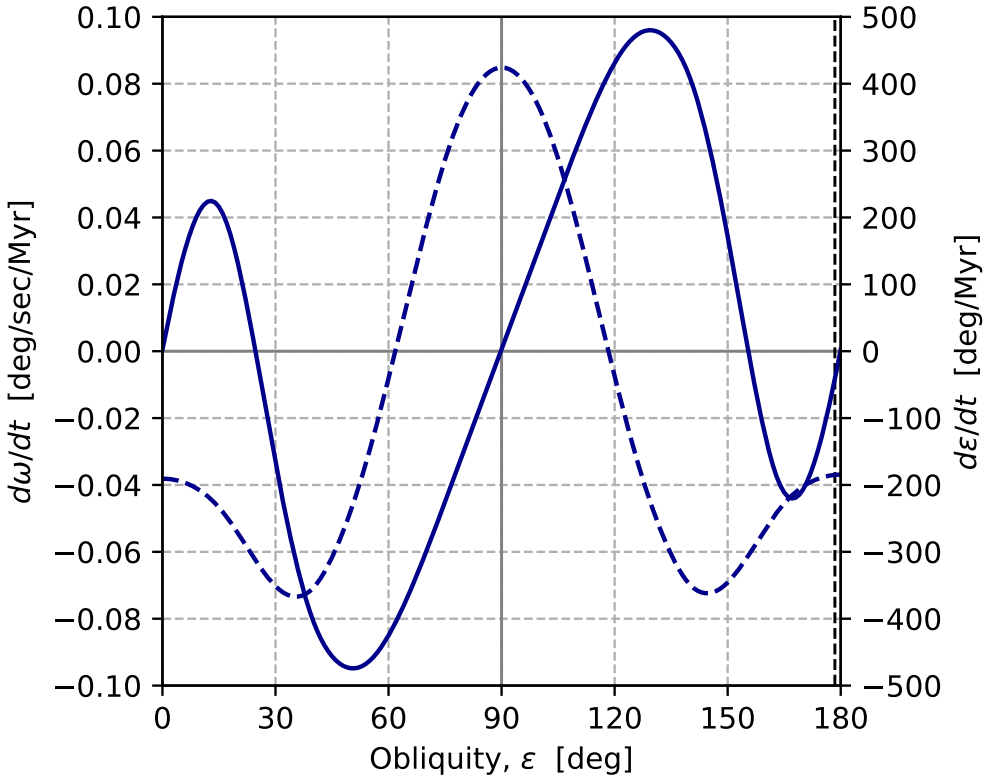

Figure C.6: The YORP effect on asteroid Itokawa depending on obliquity in the same manner as Figure 2.4. The 49k-mesh model was used for this calculation. According to Equation 2.13, ε-related torque is hereby converted into the amount of change in ε using the current spin rate of Itokawa. The vertical dashed line presents the nominal obliquity observed by Hayabusa ($\varepsilon = 178.5°$).

Appendix D

Gravitational Field Calculation

D.1 Representation of Gravity

We need to obtain the gravitational field on the surface of an irregularly shaped body for the purpose of understanding geological phenomena of the body. There are three ways to represent the gravity field of a celestial body: harmonics, mascon and polyhedron. Since each method has both merits and demerits, we need to choose one according to the intended use and the required accuracy.

D.1.1 Harmonics

Harmonics is the most classical way in wide use to represent the gravitational field. The exterior gravity field of a celestial body can be expanded in a harmonic series. For example, the potential U is expressed in consideration of the motion of

a spacecraft around a gravity celestial body as follows.

$$U(r,\theta,\lambda) = \frac{GM}{r}\left[1 + \sum_{l=1}^{\infty}\sum_{m=0}^{l}\left(\frac{R}{r}\right)^{l} P_{lm}(\sin\theta)\left(C_{lm}\cos m\lambda + S_{lm}\sin m\lambda\right)\right] \tag{D.1}$$

where G is the gravitational constant. M and R are the reference mass and radius of the body, respectively. A radius r, latitude θ and longitude λ indicate the position of the spacecraft in a spherical coordinate system. P_{lm} is the Legendre function of degree l and order m. C_{lm} and S_{lm} are series coefficients of the spherical harmonic function, which are evaluated as volume integrals within the body.

This expression is well known to often diverge within a circumscribing sphere of the body. It is difficult to represent the gravity field accurately in the vicinity of an irregularly shaped body, and much less accurate on the surface of the body.

D.1.2 Mascon

The mascon model is a kind of approximation to calculate the gravitation for a celestial object. Putting point masses on the spaced grid and reproducing the figure of the body, we can easily obtain the gravity field by calculating the gravitation of each point mass and add together contributions from all point masses. The advantage of the mascon modeling is the simplicity of the calculation. However, it has a certain margin of error depending on resolution of the particle setting.

D.1.3 Polyhedron

A polyhedron model enables us to obtain an analytical expression of the gravity field in a closed form. This approach requires the following assumption for a target body (Werner and Scheeres, 1996).

1. The body is a polyhedron.

2. The polyhedron's density is constant.

Many 3D shape models of small bodies are currently available for the polyhedron calculation owing to ground-based radar observations and spacecraft missions. Though this method is computationally expensive in comparison with the mascon model, we can calculate the gravity field accurately even on the surface of the body. In addition, we can deal with the surface of the small body as the polyhedron surface. The polyhedron model is the most suitable for calculating the asymmetric gravity field of an irregularly shaped body though it requires a constant density assumption.

Given a polyhedral shape model of an asteroid or a comet nucleus, whose surface consists of polygonal facets and edges of straight lines, we can express the gravitational potential, acceleration, gradient matrix and Laplacian at an arbitrary field point as follows (Werner and Scheeres, 1996).

$$U = \frac{1}{2}G\rho \sum_{e}^{edges} \boldsymbol{r}_e \cdot \boldsymbol{E}_e \cdot \boldsymbol{r}_e \cdot L_e - \frac{1}{2}G\rho \sum_{f}^{faces} \boldsymbol{r}_f \cdot \boldsymbol{F}_f \cdot \boldsymbol{r}_f \cdot \omega_f \tag{D.2}$$

$$\nabla U = -G\rho \sum_{e}^{edges} \boldsymbol{E}_e \cdot \boldsymbol{r}_e \cdot L_e + G\rho \sum_{f}^{faces} \boldsymbol{F}_f \cdot \boldsymbol{r}_f \cdot \omega_f \tag{D.3}$$

$$\nabla\nabla U = G\rho \sum_{e}^{edges} \boldsymbol{E}_e \cdot L_e - G\rho \sum_{f}^{faces} \boldsymbol{F}_f \cdot \omega_f \tag{D.4}$$

$$\nabla^2 U = -G\rho \sum_{f}^{faces} \omega_f = \begin{cases} 0 & (\text{outside the polyhedron}) \\ -4\pi G\rho & (\text{inside the polyhedron}) \end{cases} \tag{D.5}$$

G is the gravitational constant and ρ is the constant density of the polyhedron. The Gauss divergence theorem and Green's theorem allow us to convert a volume integral of mass distribution to integrals through the surface of the polygon. The first terms in Equation D.2 to D.4 are "edge terms", derived from line integrals through all edges of the polyhedron, and the second terms are "face terms", derived from surface integrals through all facets of the polyhedron.

The edge term is expressed as a product of a vector $\boldsymbol{r}_e$ from the field point to an arbitrary point on the edge, an edge dyad $\boldsymbol{E}_e$ and a line integral along the edge, L_e. The edge dyad of a 3×3 matrix is defined for each edge sandwiched between two facets. For example, a dyad of an edge P_1P_2 shared by facet A and facet B is

defined as:

$$\boldsymbol{E}_{12} \equiv \hat{\boldsymbol{n}}_A \hat{\boldsymbol{n}}_{12}^A + \hat{\boldsymbol{n}}_B \hat{\boldsymbol{n}}_{21}^B \tag{D.6}$$

$$= \begin{pmatrix} \hat{n}_{Ax}\hat{n}_{12x}^A & \hat{n}_{Ax}\hat{n}_{12y}^A & \hat{n}_{Ax}\hat{n}_{12z}^A \\ \hat{n}_{Ay}\hat{n}_{12x}^A & \hat{n}_{Ay}\hat{n}_{12y}^A & \hat{n}_{Ay}\hat{n}_{12z}^A \\ \hat{n}_{Az}\hat{n}_{12x}^A & \hat{n}_{Az}\hat{n}_{12y}^A & \hat{n}_{Az}\hat{n}_{12z}^A \end{pmatrix} + \begin{pmatrix} \hat{n}_{Bx}\hat{n}_{21x}^B & \hat{n}_{Bx}\hat{n}_{21y}^B & \hat{n}_{Bx}\hat{n}_{21z}^B \\ \hat{n}_{By}\hat{n}_{21x}^B & \hat{n}_{By}\hat{n}_{21y}^B & \hat{n}_{By}\hat{n}_{21z}^B \\ \hat{n}_{Bz}\hat{n}_{21x}^B & \hat{n}_{Bz}\hat{n}_{21y}^B & \hat{n}_{Bz}\hat{n}_{21z}^B \end{pmatrix}$$

where $\hat{\boldsymbol{n}}_A$ and $\hat{\boldsymbol{n}}_B$ are normal vectors to facet A and facet B, respectively (Figure D.1). The normal vector $\hat{\boldsymbol{n}}_{12}^A$ is perpendicular to the common edge P_1P_2 lying in the same plane with facet A. Similarly, $\hat{\boldsymbol{n}}_{21}^B$ is a edge normal vector lying in the same plane with facet B. Dyads for other edges are likewise defined. L_e means the potential of a straight "wire". Previous studies showed that the 1-dimensional integral L_e is expressed in terms of the distances r_i and r_j from the field point to two ends of the edge and the length of the edge, e_{ij} (MacMillan, 1930; Werner, Robert, 1994).

$$L_e \equiv \int_{edge} \frac{1}{r} ds = \int_{P_i}^{P_j} \frac{1}{r} ds = \ln \frac{r_i + r_j + e_{ij}}{r_i + r_j - e_{ij}} \tag{D.7}$$

The face term is likewise expressed as a product of a vector $\boldsymbol{r}_f$ from the field point to an arbitrary point lying on the facet, the face dyad $\boldsymbol{F}_f$ and a kind of surface integral ω_f (Figure D.2). The face dyad for a surface facet whose normal vector is

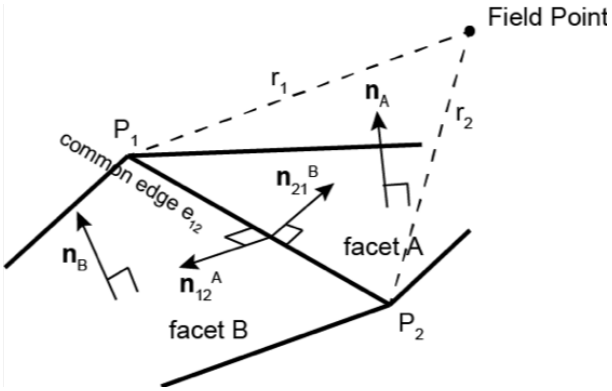

Figure D.1: An common edge P_1P_2 is shared by facet A and facet B. Each edge has an edge dyad defined in terms of normal vectors perpendicular to the facets and the common edge. $\hat{\boldsymbol{n}}_A$ and $\hat{\boldsymbol{n}}_B$ are normal vectors to the two facets A and B. The edge normal $\hat{\boldsymbol{n}}_{12}^A$ and $\hat{\boldsymbol{n}}_{21}^B$ are perpendicular to the edge and lie in the same plane with facet A and facet B, respectively.

$\hat{\boldsymbol{n}}_f$ is defined as follows.

$$\boldsymbol{F}_f \equiv \hat{\boldsymbol{n}}_f \hat{\boldsymbol{n}}_f = \begin{pmatrix} \hat{n}_{fx}\hat{n}_{fx} & \hat{n}_{fx}\hat{n}_{fy} & \hat{n}_{fx}\hat{n}_{fz} \\ \hat{n}_{fy}\hat{n}_{fx} & \hat{n}_{fy}\hat{n}_{fy} & \hat{n}_{fy}\hat{n}_{fz} \\ \hat{n}_{fz}\hat{n}_{fx} & \hat{n}_{fz}\hat{n}_{fy} & \hat{n}_{fz}\hat{n}_{fz} \end{pmatrix} \tag{D.8}$$

The face factor ω_f is recognized as a solid angle when the surface polygonal facet is viewed from the field point, thus,

$$\omega_f \equiv \iint_{face} \frac{\Delta z}{r_f^3} dS = \iint_{face} \frac{\boldsymbol{r}_f \cdot \hat{\boldsymbol{n}}_f}{r_f^3} dS = \iint_{face} \frac{\hat{\boldsymbol{r}}_f \cdot \hat{\boldsymbol{n}}_f}{r_f^2} dS \tag{D.9}$$

where $\boldsymbol{r}_f$ is the vector from the field point to an arbitrary point fixed on the facet plane, and Δz is equal to the distance from the field point to the plane. $\boldsymbol{r}_f \cdot \hat{\boldsymbol{n}}_f dS$ means a polygonal facet projected onto a spherical surface, where the center is the field point and the radius is r_f. If the surface facet is a triangle, we can write down

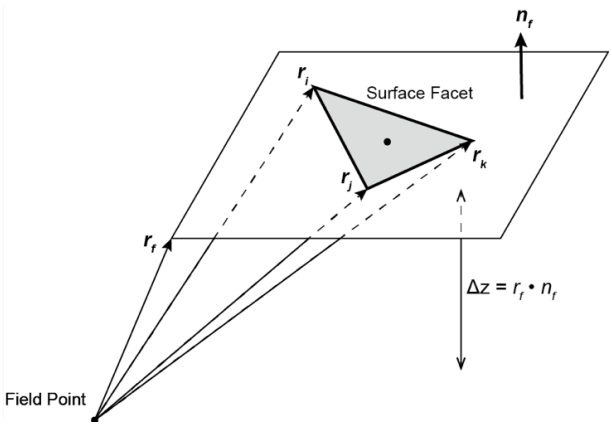

Figure D.2: A face dyad $\boldsymbol{F}_f$ is defined for each surface facet of the polyhedron in terms of a normal vector to the plane, $\hat{\boldsymbol{n}}_f$. The integral ω_f regarding the solid angle of the surface facet is expressed by three vectors from the field point to vertices of the triangular facet. $\boldsymbol{r}_f$ is a position vector to an arbitrary point lying in the same plane with the facet. For this vector, you can choose one among vertices of the triangle, $\boldsymbol{r}_i$, $\boldsymbol{r}_j$ and $\boldsymbol{r}_k$.

the solid angle ω_f in terms of three vectors $\boldsymbol{r}_i$, $\boldsymbol{r}_j$ and $\boldsymbol{r}_k$ from the field point to vertices of the triangular facet as follows (Werner and Scheeres, 1996).

$$\omega_f = 2\tan^{-1}\frac{\boldsymbol{r}_i \cdot (\boldsymbol{r}_j \times \boldsymbol{r}_k)}{r_i r_j r_k + r_i(\boldsymbol{r}_j \cdot \boldsymbol{r}_k) + r_j(\boldsymbol{r}_k \cdot \boldsymbol{r}_i) + r_k(\boldsymbol{r}_i \cdot \boldsymbol{r}_j)} \tag{D.10}$$

where r_i, r_j and r_k are the vector lengths of $\boldsymbol{r}_i$, $\boldsymbol{r}_j$ and $\boldsymbol{r}_k$, respectively.

In the end, we note the meaning of a polyhedral Laplacian. The gravitational potential is known to fulfill Poisson's equation.

$$\nabla^2 U(\boldsymbol{r}) = -4\pi G\rho(\boldsymbol{r}) \tag{D.11}$$

Therefore, the second-order differential potential becomes zero in a space where any mass does not exist (Laplace's equation $\nabla^2 U = 0$). On the other hand, $\nabla^2 U$

can be easily calculated as a summation of ω_f through all facets of the polyhedron according to Equation D.5. Therefore, Laplacian allows us to determine whether the field point is inside or outside the polyhedron. If the value of summation $\sum \omega_f$ vanishes, the field point is inside the polyhedron. This way of calculation is helpful, for example, when we conduct trajectory predictions of impact ejecta around a small body. This will make it easier to decide whether a mass point comes into contact with the irregularly shaped object or not.

Bibliography

Abe, M., Y. Takagi, K. Kitazato, S. Abe, T. Hiroi, F. Vilas, B. E. Clark, P. A. Abell, S. M. Lederer, K. S. Jarvis, T. Nimura, Y. Ueda, and A. Fujiwara (2006). Near-infrared spectral results of asteroid Itokawa from the Hayabusa spacecraft. *Science 312*(5778), 1334–1338.

Abe, S., T. Mukai, N. Hirata, O. S. Barnouin-Jha, A. F. Cheng, H. Demura, R. W. Gaskell, T. Hashimoto, K. Hiraoka, T. Honda, T. Kubota, M. Matsuoka, T. Mizuno, R. Nakamura, D. J. Scheeres, and M. Yoshikawa (2006). Mass and local topography measurements of Itokawa by Hayabusa. *Science 312*(5778), 1344–1347.

A'Hearn, M. F., M. J. S. Belton, W. A. Delamere, L. M. Feaga, D. Hampton, J. Kissel, K. P. Klaasen, L. A. McFadden, K. J. Meech, H. J. Melosh, P. H. Schultz, J. M. Sunshine, P. C. Thomas, J. Veverka, D. D. Wellnitz, D. K. Yeomans, S. Besse, D. Bodewits, T. J. Bowling, B. T. Carcich, S. M. Collins, T. L. Farnham, O. Groussin, B. Hermalyn, M. S. Kelley, M. S. Kelley, J.-Y. Li, D. J. Lindler, C. M. Lisse, S. A. McLaughlin, F. Merlin, S. Protopapa, J. E. Richardson, and J. L. Williams (2011, jun). EPOXI at Comet Hartley 2. *Science 332*(6036), 1396

LP – 1400.

Arakawa, M., K. Wada, T. Saiki, T. Kadono, Y. Takagi, K. Shirai, C. Okamoto, H. Yano, M. Hayakawa, S. Nakazawa, N. Hirata, M. Kobayashi, P. Michel, M. Jutzi, H. Imamura, K. Ogawa, N. Sakatani, Y. Iijima, R. Honda, K. Ishibashi, H. Hayakawa, and H. Sawada (2017). Scientific Objectives of Small Carry-on Impactor (SCI) and Deployable Camera 3 Digital (DCAM3-D): Observation of an Ejecta Curtain and a Crater Formed on the Surface of Ryugu by an Artificial High-Velocity Impact.

Barnouin-Jha, O. S., A. F. Cheng, T. Mukai, S. Abe, N. Hirata, R. Nakamura, R. W. Gaskell, J. Saito, and B. E. Clark (2008). Small-scale topography of 25143 Itokawa from the Hayabusa laser altimeter. *Icarus 198*(1), 108–124.

Benson, C. J., D. J. Scheeres, and N. A. Moskovitz (2019). Spin state evolution of asteroid (367943) Duende during its 2013 earth flyby. *Icarus*, 113518.

Bottke, W. F., M. Brož, D. P. O'Brien, A. C. Bagatin, A. Morbidelli, and S. Marchi (2015). The collisional evolution of the main asteroid belt. In *Asteroids IV*, pp. 701–724.

Bottke, W. F., D. D. Durda, D. Nesvorný, R. Jedicke, A. Morbidelli, D. Vokrouhlický, and H. Levison (2005a). The fossilized size distribution of the main asteroid belt. *Icarus 175*(1), 111–140.

Bottke, W. F., D. D. Durda, D. Nesvorný, R. Jedicke, A. Morbidelli, D. Vokrouhlický,

and H. F. Levison (2005b). Linking the collisional history of the main asteroid belt to its dynamical excitation and depletion. *Icarus 179*(1), 63–94.

Bottke, W. F., A. Morbidelli, R. Jedicke, J. M. Petit, H. F. Levison, P. Michel, and T. S. Metcalfe (2002). Debiased orbital and absolute magnitude distribution of the near-Earth objects. *Icarus 156*(2), 399–433.

Bottke, W. F., M. C. Nolan, R. Greenberg, and R. A. Kolvoord (1994). Velocity Distributions among Colliding Asteroids. *Icarus 107*(2), 255–268.

Bottke, W. F., D. Vokrouhlický, D. P. Rubincam, and D. Nesvorný (2006, may). THE YARKOVSKY AND YORP EFFECTS: Implications for Asteroid Dynamics. *Annual Review of Earth and Planetary Sciences 34*(1), 157–191.

Breiter, S., P. Bartczak, M. Czekaj, B. Oczujda, and D. Vokrouhlický (2009). The YORP effect on 25 143 Itokawa. *Astronomy and Astrophysics 507*(2), 1073–1081.

Čapek, D. and D. Vokrouhlický (2004). The YORP effect with finite thermal conductivity. *Icarus 172*(2), 526–536.

Carry, B. (2012). Density of asteroids. *Planetary and Space Science 73*(1), 98–118.

Cignoni, P., M. Callieri, M. Corsini, M. Dellepiane, F. Ganovelli, and G. Ranzuglia (2008). MeshLab: an Open-Source Mesh Processing Tool. *Sixth Eurographics Italian Chapter Conference*, 129–136.

Davison, T. M., G. S. Collins, and F. J. Ciesla (2010). Numerical modelling of heating in porous planetesimal collisions. *Icarus 208*(1), 468–481.

DeMeo, F. E. and B. Carry (2014). Solar System evolution from compositional mapping of the asteroid belt.

Demura, H., S. Kobayashi, E. Nemoto, N. Matsumoto, M. Furuya, A. Yukishita, N. Muranaka, H. Morita, K. Shirakawa, M. Maruya, H. Ohyama, M. Uo, T. Kubota, T. Hashimoto, J. Kawaguchi, A. Fujiwara, J. Saito, S. Sasaki, H. Miyamoto, and N. Hirata (2006). Pole and global shape of 25143 Itokawa. *Science 312*(5778), 1347–1349.

Ernst, C. M., O. S. Barnouin, R. T. Daly, and t. S. B. M. T. Team (2018). The Small Body Mapping Tool (SBMT) For Accessing, Visualising, and Analyzing Spacecraft Data in Three Dimensions. In *49th Lunar and Planetary Science Conference 2018*.

Eugster, O. (2003). Cosmic-ray exposure ages of meteorites and lunar rocks and their significance.

Eugster, O., G. F. Herzog, K. Marti, and M. Caffee (2006). Irradiation Records , Cosmic-Ray Exposure Ages , and Transfer Times of Meteorites. *Meteorites and the Early Solar System II* (1990), 829–851.

Fujiwara, A., J. Kawaguchi, D. K. Yeomans, M. Abe, T. Mukai, T. Okada, J. Saito, H. Yano, M. Yoshikawa, D. J. Scheeres, O. Barnouin-Jha, A. F. Cheng, H. Demura, R. W. Gaskell, N. Hirata, H. Ikeda, T. Kominato, H. Miyamoto, A. M. Nakamura,

R. Nakamura, S. Sasaki, and K. Uesugi (2006). The rubble-pile asteroid Itokawe as observed by Hayabusa. *Science 312*(5778), 1330–1334.

Gaskell, R., O. Barnouin-Jha, D. Scheeres, T. Mukai, N. Hirata, S. Abe, J. Saito, M. Ishiguro, T. Kubota, T. Hashimoto, J. Kawaguchi, M. Yoshikawa, K. Shirakawa, and T. Kominato (2006). Landmark Navigation Studies and Target Characterization in the Hayabusa Encounter with Itokawa. *AIAA/AAS Astrodynamics Specialist Conference and Exhibit*.

Gaskell, R., L. Jorda, C. Capanna, S. Hviid, and P. Gutierrez (2017). RO-C-MULTI-5-67P-SHAPE-V2.0.

Gaskell, R. W., O. S. Barnouin-Jha, D. J. Scheeres, A. S. Konopliv, T. Mukai, S. Abe, J. Saito, M. Ishiguro, T. Kubota, T. Hashimoto, J. Kawaguchi, M. Yoshikawa, K. Shirakawa, T. Kominato, N. Hirata, and H. Demura (2008). Characterizing and navigating small bodies with imaging data. *Meteoritics & Planetary Science 43*(6), 1049–1061.

Gladman, B. (1997). Destination: Earth. Martian meteorite delivery. *Icarus 130*(2), 228–246.

Gomes, R., H. F. Levison, K. Tsiganis, and A. Morbidelli (2005). Origin of the cataclysmic Late Heavy Bombardment period of the terrestrial planets. *Nature 435*(7041), 466–469.

Hang, S. (2018). TetGen.

Hartmann, W. K., P. Farinella, D. Vokrouhlický, S. J. Weidenschilling, A. Morbidelli, F. Marzari, D. R. Davis, and E. Ryan (1999). Reviewing the Yarkovsky effect: New light on the delivery of stone and iron meteorites from the asteroid belt. *Meteoritics & Planetary Science 34*(S4), A161–A167.

Hergenrother, C. W., C. K. Maleszewski, M. C. Nolan, J. Y. Li, C. Y. Drouet d'Aubigny, F. C. Shelly, E. S. Howell, T. R. Kareta, M. R. Izawa, M. A. Barucci, E. B. Bierhaus, H. Campins, S. R. Chesley, B. E. Clark, E. J. Christensen, D. N. DellaGiustina, S. Fornasier, D. R. Golish, C. M. Hartzell, B. Rizk, D. J. Scheeres, P. H. Smith, X. D. Zou, D. S. Lauretta, D. E. Highsmith, J. Small, D. Vokrouhlický, N. E. Bowles, E. Brown, K. L. Donaldson Hanna, T. Warren, C. Brunet, R. A. Chicoine, S. Desjardins, D. Gaudreau, T. Haltigin, S. Millington-Veloza, A. Rubi, J. Aponte, N. Gorius, A. Lunsford, B. Allen, J. Grindlay, D. Guevel, D. Hoak, J. Hong, D. L. Schrader, J. Bayron, O. Golubov, P. Sánchez, J. Stromberg, M. Hirabayashi, C. M. Hartzell, S. Oliver, M. Rascon, A. Harch, J. Joseph, S. Squyres, D. Richardson, J. P. Emery, L. McGraw, R. Ghent, R. P. Binzel, M. M. Al Asad, C. L. Johnson, L. Philpott, H. C. Susorney, E. A. Cloutis, R. D. Hanna, H. C. Connolly, F. Ciceri, A. R. Hildebrand, E. M. Ibrahim, L. Breitenfeld, T. Glotch, A. D. Rogers, B. E. Clark, S. Ferrone, C. A. Thomas, H. Campins, Y. Fernandez, W. Chang, A. Cheuvront, D. Trang, S. Tachibana, H. Yurimoto, J. R. Brucato, G. Poggiali, M. Pajola, E. Dotto, E. M. Epifani, M. K. Crombie, C. Lantz, M. R. Izawa, J. de Leon, J. Licandro, J. L. Garcia, S. Clemett, K. Thomas-Keprta, S. Van wal, M. Yoshikawa,

J. Bellerose, S. Bhaskaran, C. Boyles, S. R. Chesley, C. M. Elder, D. Farnocchia, A. Harbison, B. Kennedy, A. Knight, N. Martinez-Vlasoff, N. Mastrodemos, T. McElrath, W. Owen, R. Park, B. Rush, L. Swanson, Y. Takahashi, D. Velez, K. Yetter, C. Thayer, C. Adam, P. Antreasian, J. Bauman, C. Bryan, B. Carcich, M. Corvin, J. Geeraert, J. Hoffman, J. M. Leonard, E. Lessac-Chenen, A. Levine, J. McAdams, L. McCarthy, D. Nelson, B. Page, J. Pelgrift, E. Sahr, K. Stakkestad, D. Stanbridge, D. Wibben, B. Williams, K. Williams, P. Wolff, P. Hayne, D. Kubitschek, J. D. Deshapriya, S. Fornasier, M. Fulchignoni, P. Hasselmann, F. Merlin, A. Praet, E. B. Bierhaus, O. Billett, A. Boggs, B. Buck, S. Carlson-Kelly, J. Cerna, K. Chaffin, E. Church, M. Coltrin, J. Daly, A. Deguzman, R. Dubisher, D. Eckart, D. Ellis, P. Falkenstern, A. Fisher, M. E. Fisher, P. Fleming, K. Fortney, S. Francis, S. Freund, S. Gonzales, P. Haas, A. Hasten, D. Hauf, A. Hilbert, D. Howell, F. Jaen, N. Jayakody, M. Jenkins, K. Johnson, M. Lefevre, H. Ma, C. Mario, K. Martin, C. May, M. McGee, B. Miller, C. Miller, G. Miller, A. Mirfakhrai, E. Muhle, C. Norman, R. Olds, C. Parish, M. Ryle, M. Schmitzer, P. Sherman, M. Skeen, M. Susak, B. Sutter, Q. Tran, C. Welch, R. Witherspoon, J. Wood, J. Zareski, M. Arvizu-Jakubicki, E. Asphaug, E. Audi, R. L. Ballouz, R. Bandrowski, K. J. Becker, T. L. Becker, S. Bendall, C. A. Bennett, H. Bloomenthal, D. Blum, W. V. Boynton, J. Brodbeck, K. N. Burke, M. Chojnacki, A. Colpo, J. Contreras, J. Cutts, C. Y. Drouet d'Aubigny, D. Dean, D. N. DellaGiustina, B. Diallo, D. Drinnon, K. Drozd, H. L. Enos, R. Enos, C. Fellows, T. Ferro, M. R. Fisher, G. Fitzgibbon, M. Fitzgibbon, J. Forelli, T. Forrester, I. Galinsky, R. Gar-

cia, A. Gardner, D. R. Golish, N. Habib, D. Hamara, D. Hammond, K. Hanley, K. Harshman, C. W. Hergenrother, K. Herzog, D. Hill, C. Hoekenga, S. Hooven, E. S. Howell, E. Huettner, A. Janakus, J. Jones, T. R. Kareta, J. Kidd, K. Kingsbury, S. S. Balram-Knutson, L. Koelbel, J. Kreiner, D. Lambert, D. S. Lauretta, C. Lewin, B. Lovelace, M. Loveridge, M. Lujan, C. K. Maleszewski, R. Malhotra, K. Marchese, E. McDonough, N. Mogk, V. Morrison, E. Morton, R. Munoz, J. Nelson, M. C. Nolan, J. Padilla, R. Pennington, A. Polit, N. Ramos, V. Reddy, M. Riehl, B. Rizk, H. L. Roper, S. Salazar, S. R. Schwartz, S. Selznick, N. Shultz, P. H. Smith, S. Stewart, S. Sutton, T. Swindle, Y. H. Tang, M. Westermann, C. W. Wolner, D. Worden, T. Zega, Z. Zeszut, A. Bjurstrom, L. Bloomquist, C. Dickinson, E. Keates, J. Liang, V. Nifo, A. Taylor, F. Teti, M. Caplinger, H. Bowles, S. Carter, S. Dickenshied, D. Doerres, T. Fisher, W. Hagee, J. Hill, M. Miner, D. Noss, N. Piacentine, M. Smith, A. Toland, P. Wren, M. Bernacki, D. P. Munoz, S. I. Watanabe, S. A. Sandford, A. Aqueche, B. Ashman, M. Barker, A. Bartels, K. Berry, B. Bos, R. Burns, A. Calloway, R. Carpenter, N. Castro, R. Cosentino, J. Donaldson, J. P. Dworkin, J. E. Cook, C. Emr, D. Everett, D. Fennell, K. Fleshman, D. Folta, D. Gallagher, J. Garvin, K. Getzandanner, D. Glavin, S. Hull, K. Hyde, H. Ido, A. Ingegneri, N. Jones, P. Kaotira, L. F. Lim, A. Liounis, C. Lorentson, D. Lorenz, J. Lyzhoft, E. M. Mazarico, R. Mink, W. Moore, M. Moreau, S. Mullen, J. Nagy, G. Neumann, J. Nuth, D. Poland, D. C. Reuter, L. Rhoads, S. Rieger, D. Rowlands, D. Sallitt, A. Scroggins, G. Shaw, A. A. Simon, J. Swenson, P. Vasudeva, M. Wasser, R. Zellar, J. Grossman, G. Johnston,

M. Morris, J. Wendel, A. Burton, L. P. Keller, L. McNamara, S. Messenger, K. Nakamura-Messenger, A. Nguyen, K. Righter, E. Queen, K. Bellamy, K. Dill, S. Gardner, M. Giuntini, B. Key, J. Kissell, D. Patterson, D. Vaughan, B. Wright, R. W. Gaskell, L. Le Corre, J. Y. Li, J. L. Molaro, E. E. Palmer, M. A. Siegler, P. Tricarico, J. R. Weirich, X. D. Zou, T. Ireland, K. Tait, P. Bland, S. Anwar, N. Bojorquez-Murphy, P. R. Christensen, C. W. Haberle, G. Mehall, K. Rios, I. Franchi, B. Rozitis, C. B. Beddingfield, J. Marshall, D. N. Brack, A. S. French, J. W. McMahon, D. J. Scheeres, E. R. Jawin, T. J. McCoy, S. Russell, M. Killgore, W. F. Bottke, V. E. Hamilton, H. H. Kaplan, K. J. Walsh, J. L. Bandfield, B. C. Clark, M. Chodas, M. Lambert, R. A. Masterson, M. G. Daly, J. Freemantle, J. A. Seabrook, O. S. Barnouin, K. Craft, R. T. Daly, C. Ernst, R. C. Espiritu, M. Holdridge, M. Jones, A. H. Nair, L. Nguyen, J. Peachey, M. E. Perry, J. Plescia, J. H. Roberts, R. Steele, R. Turner, J. Backer, K. Edmundson, J. Mapel, M. Milazzo, S. Sides, C. Manzoni, B. May, M. Delbo', G. Libourel, P. Michel, A. Ryan, F. Thuillet, and B. Marty (2019). The operational environment and rotational acceleration of asteroid (101955) Bennu from OSIRIS-REx observations. *Nature Communications 10*(1).

Hirabayashi, M., E. Tatsumi, H. Miyamoto, G. Komatsu, S. Sugita, S.-i. Watanabe, D. J. Scheeres, O. S. Barnouin, P. Michel, C. Honda, T. Michikami, Y. Cho, T. Morota, N. Hirata, N. Hirata, N. Sakatani, S. R. Schwartz, R. Honda, Y. Yokota, S. Kameda, H. Suzuki, T. Kouyama, M. Hayakawa, M. Matsuoka, K. Yoshioka, K. Ogawa, H. Sawada, M. Yoshikawa, and Y. Tsuda (2019). The Western Bulge of

162173 Ryugu Formed as a Result of a Rotationally Driven Deformation Process. *The Astrophysical Journal 874*(1), L10.

Hirata, N., O. S. Barnouin-Jha, C. Honda, R. Nakamura, H. Miyamoto, S. Sasaki, H. Demura, A. M. Nakamura, T. Michikami, R. W. Gaskell, and J. Saito (2009). A survey of possible impact structures on 25143 Itokawa. *Icarus 200*(2), 486–502.

Hirata, N., T. Morota, Y. Cho, M. Kanamaru, S. ichiro Watanabe, S. Sugita, N. Hirata, Y. Yamamoto, R. Noguchi, Y. Shimaki, E. Tatsumi, K. Yoshioka, H. Sawada, Y. Yokota, N. Sakatani, M. Hayakawa, M. Matsuoka, R. Honda, S. Kameda, M. Yamada, T. Kouyama, H. Suzuki, C. Honda, K. Ogawa, Y. Tsuda, M. Yoshikawa, T. Saiki, S. Tanaka, F. Terui, S. Nakazawa, S. Kikuchi, T. Yamaguchi, N. Ogawa, G. Ono, Y. Mimasu, K. Yoshikawa, T. Takahashi, Y. Takei, A. Fujii, H. Takeuchi, T. Okada, K. Shirai, and Y. ichi Iijima (2020). The spatial distribution of impact craters on Ryugu. *Icarus 338*.

Hirt, C. and M. Kuhn (2017). Convergence and divergence in spherical harmonic series of the gravitational field generated by high-resolution planetary topography —A case study for the Moon. *Journal of Geophysical Research: Planets 122*(8), 1727–1746.

Housen, K. R. and K. A. Holsapple (2011). Ejecta from impact craters. *Icarus 211*(1), 856–875.

Jutzi, M. and W. Benz (2017, jan). Formation of bi-lobed shapes by sub-catastrophic

collisions: A late origin of comet 67P's structure. *Astronomy and Astrophysics 597*, A62.

Kanamaru, M. and S. Sasaki (2019). Estimation of Interior Density Distribution for Small Bodies: The Case of Asteroid Itokawa. *Transactions of the Japan Society for Aeronautical and Space Sciences, Aerospace Technology Japan advpub*.

Kanamaru, M., S. Sasaki, and M. Wieczorek (2019). Density distribution of asteroid 25143 Itokawa based on smooth terrain shape. *Planetary and Space Science 174*, 32–42.

Kitazato, K., R. E. Milliken, T. Iwata, M. Abe, M. Ohtake, S. Matsuura, T. Arai, Y. Nakauchi, T. Nakamura, M. Matsuoka, H. Senshu, N. Hirata, T. Hiroi, C. Pilorget, R. Brunetto, F. Poulet, L. Riu, J. P. Bibring, D. Takir, D. L. Domingue, F. Vilas, M. A. Barucci, D. Perna, E. Palomba, A. Galiano, K. Tsumura, T. Osawa, M. Komatsu, A. Nakato, T. Arai, N. Takato, T. Matsunaga, Y. Takagi, K. Matsumoto, T. Kouyama, Y. Yokota, E. Tatsumi, N. Sakatani, Y. Yamamoto, T. Okada, S. Sugita, R. Honda, T. Morota, S. Kameda, H. Sawada, C. Honda, M. Yamada, H. Suzuki, K. Yoshioka, M. Hayakawa, K. Ogawa, Y. Cho, K. Shirai, Y. Shimaki, N. Hirata, A. Yamaguchi, N. Ogawa, F. Terui, T. Yamaguchi, Y. Takei, T. Saiki, S. Nakazawa, S. Tanaka, M. Yoshikawa, S. Watanabe, and Y. Tsuda (2019). The surface composition of asteroid 162173 Ryugu from Hayabusa2 near-infrared spectroscopy. *Science 364*(6437), 272–275.

Konopliv, A. S., J. K. Miller, W. M. Owen, D. K. Yeomans, J. D. Giorgini,

R. Garmier, and J. P. Barriot (2002). A global solution for the gravity field, rotation, landmarks, and ephemeris of Eros. *Icarus 160*(2), 289–299.

Kryszczyńska, A., A. La Spina, P. Paolicchi, A. W. Harris, S. Breiter, and P. Pravec (2007). New findings on asteroid spin-vector distributions. *Icarus 192*(1), 223–237.

La Spina, A., P. Paolicchi, A. Kryszczyńska, and P. Pravec (2004). Retrograde spins of near-Earth asteroids from the Yarkovsky effect. *Nature 428*(6981), 400–401.

Lowry, S. C., A. Fitzsimmons, P. Pravec, D. Vokrouhlický, H. Boehnhardt, P. A. Taylor, J. L. Margot, A. Galád, M. Irwin, J. Irwin, and P. Kusnirák (2007). Direct detection of the asteroidal YORP effect. *Science 316*(5822), 272–274.

Lowry, S. C., P. R. Weissman, S. R. Duddy, B. Rozitis, A. Fitzsimmons, S. F. Green, M. D. Hicks, C. Snodgrass, S. D. Wolters, S. R. Chesley, J. Pittichová, and P. van Oers (2014). The internal structure of asteroid (25143) Itokawa as revealed by detection of YORP spin-up. *Astronomy & Astrophysics 562*, A48.

MacMillan, W. D. (1930). *The Theory of the Potential*. McGraw-Hill Book Co.

Marzari, F., A. Rossi, and D. J. Scheeres (2011). Combined effect of YORP and collisions on the rotation rate of small Main Belt asteroids. *Icarus 214*(2), 622–631.

McEwen, A. S., J. M. Moore, and E. M. Shoemaker (1997). The phanerozoic impact

cratering rate: Evidence from the farside of the Moon. *Journal of Geophysical Research E: Planets 102*(E4), 9231–9242.

Miller, J. K., A. S. Konopliv, P. G. Antreasian, J. J. Bordi, S. Chesley, C. E. Helfrich, W. M. Owen, T. C. Wang, B. G. Williams, D. K. Yeomans, and D. J. Scheeres (2002). Determination of shape, gravity, and rotational state of asteroid 433 Eros. *Icarus 155*(1), 3–17.

Miyamoto, H., H. Yano, D. J. Scheeres, S. Abe, O. Barnouin-Jha, A. F. Cheng, H. Demura, R. W. Gaskell, N. Hirata, M. Ishiguro, T. Michikami, A. M. Nakamura, R. Nakamura, J. Saito, and S. Sasaki (2007). Regolith migration and sorting on asteroid Itokawa. *Science 316*(5827), 1011–1014.

Morbidelli, A., H. F. Levison, K. Tsiganis, and R. Gomes (2005). Chaotic capture of Jupiter's Trojan asteroids in the early Solar System. *Nature 435*(7041), 462–465.

Morbidelli, A. and D. Vokrouhlický (2003). The Yarkovsky-driven origin of near-Earth asteroids. *Icarus 163*(1), 120–134.

Motooka, N. and J. Kawaguchi (2012). Study on the gravity field on the surface of Itokawa. In *the 22nd Workshop on JAXA Astrodynamics and Flight Mechanics*, pp. A–15.

Nakamura, T., A. M. Nakamura, J. Saito, S. Sasaki, R. Nakamura, H. Demura, H. Akiyama, and D. Tholen (2001, nov). Multi-band imaging camera and its

sciences for the Japanese near-earth asteroid mission MUSES-C. *Earth, Planets and Space 53*(11), 1047–1063.

Neumann, W., D. Breuer, and T. Spohn (2013). The thermo-chemical evolution of Asteroid 21 Lutetia. *Icarus 224*(1), 126–143.

Nolan, M. C., E. S. Howell, D. J. Scheeres, J. W. McMahon, O. Golubov, C. W. Hergenrother, J. P. Emery, K. S. Noll, S. R. Chesley, and D. S. Lauretta (2019). Detection of Rotational Acceleration of Bennu Using HST Light Curve Observations. *Geophysical Research Letters 46*(4), 1956–1962.

Ostro, S. J., J. L. Margot, L. A. Benner, J. D. Giorgini, D. J. Scheeres, E. G. Fahnestock, S. B. Broschart, J. Bellerose, M. C. Nolan, C. Magri, P. Pravec, P. Scheirich, R. Rose, R. F. Jurgens, E. M. De Jong, and S. Suzuki (2006). Radar imaging of binary near-earth asteroid (66391) 1999 KW4. *Science 314*(5803), 1276–1280.

Pätzold, M., T. Andert, M. Hahn, S. W. Asmar, J. P. Barriot, M. K. Bird, B. Häusler, K. Peter, S. Tellmann, E. Grün, P. R. Weissman, H. Sierks, L. Jorda, R. Gaskell, F. Preusker, and F. Scholten (2016). A homogeneous nucleus for comet 67P/Churyumov-Gerasimenko from its gravity field. *Nature 530*(7588), 63–65.

Ramachandran, P. and G. Varoquaux (2011). Mayavi: 3D visualization of scientific data. *Computing in Science and Engineering 13*(2), 40–51.

Richardson, J. E. and T. J. Bowling (2014). Investigating the combined effects of shape, density, and rotation on small body surface slopes and erosion rates. *Icarus 234*, 53–65.

Rubincam, D. P. (2000). Radiative Spin-up and Spin-down of Small Asteroids. *Icarus 148*(1), 2–11.

Saiki, T., H. Imamura, M. Arakawa, K. Wada, Y. Takagi, M. Hayakawa, K. Shirai, H. Yano, and C. Okamoto (2017). The Small Carry-on Impactor (SCI) and the Hayabusa2 Impact Experiment.

Saito, J., H. Miyamoto, R. Nakamura, M. Ishiguro, T. Michikami, A. M. Nakamura, H. Demura, S. Sasaki, N. Hirata, C. Honda, A. Yamamoto, Y. Yokota, T. Fuse, F. Yoshida, D. J. Tholen, R. W. Gaskell, T. Hashimoto, T. Kubota, Y. Higuchi, T. Nakamura, P. Smith, K. Hiraoka, T. Honda, S. Kobayashi, M. Furuya, N. Matsumoto, E. Nemoto, A. Yukishita, K. Kitazato, B. Dermawan, A. Sogame, J. Terazono, C. Shinohara, and H. Akiyama (2006). Detailed images of asteroid 25143 Itokawa from Hayabusa. *Science 312*(5778), 1341–1344.

Scheeres, D., M. Abe, M. Yoshikawa, R. Nakamura, R. W. Gaskell, and P. A. Abell (2007). The effect of YORP on Itokawa. *Icarus 188*(2), 425–429.

Scheeres, D., E. G. Fahnestock, S. J. Ostro, J. L. Margot, L. A. M. Benner, S. B. Broschart, J. Bellerose, J. D. Giorgini, M. C. Nolan, C. Magri, P. Pravec, P. Scheirich, R. Rose, R. F. Jurgens, E. M. De Jong, and S. Suzuki (2006).

Dynamical configuration of binary near-earth asteroid (66391) 1999 KW4. *Science 314*(5803), 1280–1283.

Scheeres, D., B. Khushalani, and R. Werner (2000). Estimating asteroid density distributions from shape and gravity information. *Planetary and Space Science 48*(10), 965–971.

Scheeres, D. J. (2015). Landslides and Mass shedding on spinning spheroidal asteroids. *Icarus 247*, 1–17.

Scheeres, D. J. and R. W. Gaskell (2008). Effect of density inhomogeneity on YORP: The case of Itokawa. *Icarus 198*(1), 125–129.

Scheeres, D. J., S. J. Ostro, R. A. Werner, E. Asphaug, and R. S. Hudson (2000). Effects of Gravitational Interactions on Asteroid Spin States. *Icarus 147*(1), 106–118.

Schöberl, J. (1997, jul). An advancing front 2D/3D-mesh generator based on abstract rules. *Computing and Visualization in Science 1*(1), 41–52.

Slivan, S. M. (2002). Spin vector alignment of koronis family asteroids. *Nature 419*(6902), 49–51.

Slivan, S. M., R. P. Binzel, S. C. Boroumand, M. W. Pan, C. M. Simpson, J. T. Tanabe, R. M. Villastrigo, L. L. Yen, R. P. Ditteon, D. P. Pray, and R. D. Stephens (2008). Rotation rates in the Koronis family, complete to H âĽĹ 11.2. *Icarus 195*(1), 226–276.

Statler, T. S. (2009). Extreme sensitivity of the YORP effect to small-scale topography. *Icarus 202*(2), 502–513.

Stooke, P. (2012). Stooke Small Bodies Maps MULTI-SA-MULTI-6-STOOKEMAPS-V2.0.

Sugita, S., R. Honda, T. Morota, S. Kameda, H. Sawada, E. Tatsumi, M. Yamada, C. Honda, Y. Yokota, T. Kouyama, N. Sakatani, K. Ogawa, H. Suzuki, T. Okada, N. Namiki, S. Tanaka, Y. Iijima, K. Yoshioka, M. Hayakawa, Y. Cho, M. Matsuoka, N. Hirata, N. Hirata, H. Miyamoto, D. Domingue, M. Hirabayashi, T. Nakamura, T. Hiroi, T. Michikami, P. Michel, R. L. Ballouz, O. S. Barnouin, C. M. Ernst, S. E. Schröder, H. Kikuchi, R. Hemmi, G. Komatsu, T. Fukuhara, M. Taguchi, T. Arai, H. Senshu, H. Demura, Y. Ogawa, Y. Shimaki, T. Sekiguchi, T. G. Müller, A. Hagermann, T. Mizuno, H. Noda, K. Matsumoto, R. Yamada, Y. Ishihara, H. Ikeda, H. Araki, K. Yamamoto, S. Abe, F. Yoshida, A. Higuchi, S. Sasaki, S. Oshigami, S. Tsuruta, K. Asari, S. Tazawa, M. Shizugami, J. Kimura, T. Otsubo, H. Yabuta, S. Hasegawa, M. Ishiguro, S. Tachibana, E. Palmer, R. Gaskell, L. Le Corre, R. Jaumann, K. Otto, N. Schmitz, P. A. Abell, M. A. Barucci, M. E. Zolensky, F. Vilas, F. Thuillet, C. Sugimoto, N. Takaki, Y. Suzuki, H. Kamiyoshihara, M. Okada, K. Nagata, M. Fujimoto, M. Yoshikawa, Y. Yamamoto, K. Shirai, R. Noguchi, N. Ogawa, F. Terui, S. Kikuchi, T. Yamaguchi, Y. Oki, Y. Takao, H. Takeuchi, G. Ono, Y. Mimasu, K. Yoshikawa, T. Takahashi, Y. Takei, A. Fujii, C. Hirose, S. Nakazawa, S. Hosoda, O. Mori, T. Shimada, S. Soldini, T. Iwata,

M. Abe, H. Yano, R. Tsukizaki, M. Ozaki, K. Nishiyama, T. Saiki, S. Watanabe, and Y. Tsuda (2019). The geomorphology, color, and thermal properties of Ryugu: Implications for parent-body processes. *Science 364*(6437).

Szeliski, R. (2011). Computer vision: algorithms and applications. *Choice Reviews Online 48*(09), 48–5140–48–5140.

Tachibana, S., M. Abe, M. Arakawa, M. Fujimoto, Y. Iijima, M. Ishiguro, K. Kitazato, N. Kobayashi, N. Namiki, T. Okada, R. Okazaki, H. Sawada, S. Sugita, Y. Takano, S. Tanaka, S. Watanabe, M. Yoshikawa, and H. Kuninaka (2014). Hayabusa2: Scientific importance of samples returned from C-type near-Earth asteroid (162173) 1999 JU3. *Geochemical Journal 48*(6), 571–581.

Takahashi, Y. and D. J. Scheeres (2014). Morphology driven density distribution estimation for small bodies. *Icarus 233*, 179–193.

Takita, J., H. Senshu, and S. Tanaka (2017). Feasibility and Accuracy of Thermophysical Estimation of Asteroid 162173 Ryugu (1999 JU3) from the Hayabusa2 Thermal Infrared Imager.

Taylor, P. A., J. L. Margot, D. Vokrouhlický, D. J. Scheeres, P. Pravec, S. C. Lowry, A. Fitzsimmons, M. C. Nolan, S. J. Ostro, L. A. Benner, J. D. Giorgini, and C. Magri (2007). Spin rate of asteroid (54509) 2000 PH5 increasing due to the YORP effect. *Science 316*(5822), 274–277.

Thomas, N., H. Sierks, C. Barbieri, P. L. Lamy, R. Rodrigo, H. Rickman, D. Koschny,

H. U. Keller, J. Agarwal, M. F. A'Hearn, F. Angrilli, A. T. Auger, M. A. Barucci, J. L. Bertaux, I. Bertini, S. Besse, D. Bodewits, G. Cremonese, V. Da Deppo, B. Davidssonn, M. De Cecco, S. Debei, M. R. El-Maarry, F. Ferri, S. Fornasier, M. Fulle, L. Giacomini, O. Groussin, P. J. Gutierrez, C. Güttler, S. F. Hviid, W. H. Ip, L. Jorda, J. Knollenberg, J. R. Kramm, E. Kührt, M. Küppers, F. La Forgia, L. M. Lara, M. Lazzarin, J. J. Lopez Moreno, S. Magrin, S. Marchi, F. Marzari, M. Massironi, H. Michalik, R. Moissl, S. Mottola, G. Naletto, N. Oklay, M. Pajola, A. Pommerol, F. Preusker, L. Sabau, F. Scholten, C. Snodgrass, C. Tubiana, J. B. Vincent, and K. P. Wenzel (2015). The morphological diversity of comet 67P/Churyumov-Gerasimenko. *Science 347*(6220).

Thomas, P., M. F. A'Hearn, J. Veverka, M. J. Belton, J. Kissel, K. P. Klaasen, L. A. McFadden, H. J. Melosh, P. H. Schultz, S. Besse, B. T. Carcich, T. L. Farnham, O. Groussin, B. Hermalyn, J. Y. Li, D. J. Lindler, C. M. Lisse, K. Meech, and J. E. Richardson (2013). Shape, density, and geology of the nucleus of Comet 103P/Hartley 2. *Icarus 222*(2), 550–558.

Thomas, P. C. (1993). Gravity, Tides, and Topography on Small Satellites and Asteroids: Application to Surface Features of the Martian Satellites. *Icarus 105*(2), 326–344.

Tsiganis, K., R. Gomes, A. Morbidelli, and H. F. Levison (2005). Origin of the orbital architecture of the giant planets of the Solar System. *Nature 435*(7041), 459–461.

Tsuchiyama, A., M. Uesugi, T. Matsushima, T. Michikami, T. Kadono, T. Nakamura, K. Uesugi, T. Nakano, S. A. Sandford, R. Noguchi, T. Matsumoto, J. Matsuno, T. Nagano, Y. Imai, A. Takeuchi, Y. Suzuki, T. Ogami, J. Katagiri, M. Ebihara, T. R. Ireland, F. Kitajima, K. Nagao, H. Naraoka, T. Noguchi, R. Okazaki, H. Yurimoto, M. E. Zolensky, T. Mukai, M. Abe, T. Yada, A. Fujimura, M. Yoshikawa, and J. Kawaguchi (2011). Three-dimensional structure of hayabusa samples: Origin and evolution of itokawa regolith. *Science 333*(6046), 1125–1128.

Tsuda, Y., M. Yoshikawa, T. Saiki, S. Nakazawa, and S. ichiro Watanabe (2019). Hayabusa2 Sample return and kinetic impact mission to near-earth asteroid Ryugu. *Acta Astronautica 156*, 387–393.

Vavilov, D. E., S. Eggl, Y. D. Medvedev, and P. B. Zatitskiy (2019). Shape evolution of cometary nuclei via anisotropic mass loss. *Astronomy and Astrophysics 622*.

Veverka, J., M. Robinson, P. Thomas, S. Murchie, J. F. Bell, N. Izenberg, C. Chapman, A. Harch, M. Bell, B. Carcich, A. Cheng, B. Clark, D. Domingue, D. Dunham, R. Farquhar, M. J. Gaffey, E. Hawkins, J. Joseph, R. Kirk, H. Li, P. Lucey, M. Malin, P. Martin, L. McFadden, W. J. Merline, J. K. Miller, J. Owen, C. Peterson, L. Prockter, J. Warren, D. Wellnitz, B. G. Williams, and D. K. Yeomans (2000). NEAR at Eros: Imaging and spectral results. *Science 289*(5487), 2088–2097.

Vokrouhlický, D. (1998). Diurnal Yarkovsky effect as a source of mobility of

meter-sized asteroidal fragments: II. Non-sphericity effects. *Astronomy and Astrophysics 338*(1), 353–363.

Vokrouhlický, D., W. F. Bottke, S. R. Chesley, D. J. Scheeres, and T. S. Statler (2015). The Yarkovsky and YORP effects. In *Asteroids IV*, pp. 509–531.

Vokrouhlický, D. and D. Čapek (2002). Yorp-induced long-term evolution of the spin state of small asteroids and meteoroids: Rubincam's approximation. *Icarus 159*(2), 449–467.

Vokrouhlický, D., D. Nesvorný, and W. F. Bottke (2003). The vector alignments of asteroid spins by thermal torques. *Nature 425*(6954), 147–151.

Walsh, K. J., M. Delbó, W. F. Bottke, D. Vokrouhlický, and D. S. Lauretta (2013). Introducing the Eulalia and new Polana asteroid families: Re-assessing primitive asteroid families in the inner Main Belt. *Icarus 225*(1), 283–297.

Walsh, K. J., A. Morbidelli, S. N. Raymond, D. P. O'Brien, and A. M. Mandell (2011). A low mass for Mars from Jupiter's early gas-driven migration. *Nature 475*(7355), 206–209.

Watanabe, S., M. Hirabayashi, N. Hirata, N. Hirata, R. Noguchi, Y. Shimaki, H. Ikeda, E. Tatsumi, M. Yoshikawa, S. Kikuchi, H. Yabuta, T. Nakamura, S. Tachibana, Y. Ishihara, T. Morota, K. Kitazato, N. Sakatani, K. Matsumoto, K. Wada, H. Senshu, C. Honda, T. Michikami, H. Takeuchi, T. Kouyama, R. Honda, S. Kameda, T. Fuse, H. Miyamoto, G. Komatsu, S. Sugita, T. Okada,

N. Namiki, M. Arakawa, M. Ishiguro, M. Abe, R. Gaskell, E. Palmer, O. S. Barnouin, P. Michel, A. S. French, J. W. McMahon, D. J. Scheeres, P. A. Abell, Y. Yamamoto, S. Tanaka, K. Shirai, M. Matsuoka, M. Yamada, Y. Yokota, H. Suzuki, K. Yoshioka, Y. Cho, S. Tanaka, N. Nishikawa, T. Sugiyama, H. Kikuchi, R. Hemmi, T. Yamaguchi, N. Ogawa, G. Ono, Y. Mimasu, K. Yoshikawa, T. Takahashi, Y. Takei, A. Fujii, C. Hirose, T. Iwata, M. Hayakawa, S. Hosoda, O. Mori, H. Sawada, T. Shimada, S. Soldini, H. Yano, R. Tsukizaki, M. Ozaki, Y. Iijima, K. Ogawa, M. Fujimoto, T. M. Ho, A. Moussi, R. Jaumann, J. P. Bibring, C. Krause, F. Terui, T. Saiki, S. Nakazawa, and Y. Tsuda (2019). Hayabusa2 arrives at the carbonaceous asteroid 162173 Ryugu-A spinning top-shaped rubble pile. *Science 364*(6437), 268–272.

Watanabe, S., Y. Tsuda, M. Yoshikawa, S. Tanaka, T. Saiki, and S. Nakazawa (2017). Hayabusa2 Mission Overview.

Werner, R. and D. J. Scheeres (1996). Exterior gravitation of a polyhedron derived and compared with harmonic and mascon gravitation representations of asteroid 4769 Castalia. *Celestial Mechanics and Dynamical Astronomy 65*(3), 313–344.

Werner, R. A. (1997). Spherical harmonic coefficients for the potential of a constant-density polyhedron. *Computers and Geosciences 23*(10), 1071–1077.

Werner, Robert, A. (1994, jul). The gravitational potential of a homogeneous polyhedron or don't cut corners. *Celestial Mechanics & Dynamical Astronomy 59*(3), 253–278.

Wilkison, S. L., M. S. Robinson, P. C. Thomas, J. Veverka, T. J. McCoy, S. L. Murchie, L. M. Prockter, and D. K. Yeomans (2002). An estimate of Eros's porosity and implications for internal structure. *Icarus 155*(1), 94–103.

Yeomans, D. K., P. G. Antreasian, J. P. Barriot, S. R. Chesley, D. W. Dunham, R. W. Farquhar, J. D. Giorgini, C. E. Helfrich, A. S. Konopliv, J. V. McAdams, J. K. Miller, J. Owen, D. J. Scheeres, P. C. Thomas, J. Veverka, and B. G. Williams (2000). Radio science results during the NEAR-Shoemaker spacecraft rendezvous with Eros. *Science 289*(5487), 2085–2088.

Vita – Masanori Kanamaru

Education

1. Doctor of Science in Planetary Science at Department of Earth and Space Science, Graduate School of Science, Osaka University, April 2017 – March 2020.

2. Master of Science in Planetary Science at Department of Earth and Space Science, Graduate School of Science, Osaka University, April 2015 – March 2017.

3. Bachelor of Science in Physics at Department of Physics, Osaka University, April 2011 – March 2015.

Academic Employment

4. Research Assistant, Graduate School of Science, Osaka University, August 2018 – March 2020. Developing a method to estimate interior density distri-

bution within small solar system bodies such as asteroids and comets.

5. Teaching Assistant, Department of Earth and Space Science, Graduate School of Science, Osaka University, April 2015 – September 2016. Responsibilities include: Preparing documents for classes, processing test results and advising undergraduate students on class- and research- related matters.

Publications

*Corresponding author

6. Hirata N.*, Morota T., Cho Y., **Kanamaru M.**, Watanabe S., Sugita S., Hirata N., Yamamoto Y., Noguchi R., Shimaki Y., Tatsumi E., Yoshioka K., Sawada H., Yokota Y., Sakatani N., Hayakawa M., Matsuoka M., Honda R., Kameda S., Yamada M, Kouyama T., Suzuki H., Honda C., Ogawa K., Tsuda Y., Yoshikawa M., Saiki T., Tanaka S., Terui F., Nakazawa S., Kikuchi S., Yamaguchi T., Ogawa N., Ono G., Mimasu Y., Yoshikawa K., Takahashi T., Takei Y., Fujii A., Takeuchi H., Okada T., Shirai K., Iijima Y., "The spatial distribution of impact craters on Ryugu", *Icarus, 338*, March 2020.

7. **Kanamaru M.***, Sasaki S., Wieczorek M., "Density Distribution of Asteroid 25143 Itokawa Based on Smooth Terrain Shape", *Planetary and Space Science, 174*, 32–42, September 2019.

8. **Kanamaru M.***, Sasaki S., "Estimation of Interior Density Distribution for

Small Bodies: The Case of Asteroid Itokawa", *Transactions of the Japan Society for Aeronautical and Space Sciences, 17, 3*, 270–275, January 2019.

In revision

9. Noguchi R., Hirata N.*, Shimaki Y., Nishikawa N., Tanaka S., Sugiyama T., Morota T., Sugita S., Cho Y., Honda R., Tatsumi E., Yoshioka K., Sawada H., Yokota Y., Sakatani N., Hayakawa M., Matsuoka M., Yamada M., Kouyama T., Suzuki H., Honda C., Ogawa K., **Kanamaru M.**, Watanabe S., "Crater depth-to-diameter ratios on asteroid 162173 Ryugu" submitted to *Icarus*.

10. Morota T.*, Sugita S., Cho Y., **Kanamaru M.**, Tatsumi E., Sakatani N., Honda R., Hirata N., Kikuchi H., Yamada M., Yokota Y., Kameda S., Matsuoka M., Sawada H., Honda C., Kouyama T., K. Ogawa K., Suzuki H., Yoshioka K., Hayakawa M., Hirata N., Hirabayashi M., Miyamoto H., Michikami T., Hiroi T., Hemmi R., Barnouin O. S., Ernst C. M., Koasati K., Nakamura T., Riu L., Senshu H., Kobayashi H., Sasaki S., Komatsu G., Tanabe N., Fujii Y., Irie T., Suemitsu M., Takaki N., Sugimoto C., Yumoto K., Ishida M., Kato H., Moroi K., Domingue D., Michel P., Pilorget C., Iwata T., Abe M., Ohtake M., Nakauchi Y., Tsumura K., Yabuta H., Ishihara Y., Noguchi R., Matsumoto K., Miura A., Namiki N., Tachibana S., Arakawa M., Ikeda H., Ishiguro M., Wada K., Mizuno T., Hirose C., Hosoda S., Mori O., Shimada T., Soldini S., Tsukizaki R., Yano H., Ozaki M., Takeuchi H., Yamamoto Y., Okada

T., Shimaki Y., Shirai K., Iijima Y., Noda H., Kikuchi S., Yamaguchi T., Ogawa N., Ono G., Mimasu Y., Yoshikawa K., Takahashi T., Takei Y., Fujii A., Nakazawa S., Terui F., Tanaka S., Yoshikawa M., Saiki T., Watanabe S., Tsuda Y., "Surface evolution of carbonaceous asteroid 162173 Ryugu revealed from global mapping and touchdown operation of Hayabusa2" submitted to *Science*.

Academic Awards

11. Received Outstanding Student Presentation Award at Japan Geoscience Union Meeting, May 2019.

12. Received Career Development Award at the 49*th* Lunar and Planetary Science Conference, March 2018.

Presentations at International Conferences

◯Presenter

Oral presentation

13. ◯**Kanamaru M.**, Sasaki S., Wieczorek M., "Density Distribution within Small Solar System Bodies Based on Smooth Terrain Shape: Asteroid 25143

Itokawa and Comet 67P/Churyumov-Gerasimenko", *Japan Geoscience Union Meeting 2019, PPS03-23*, Chiba, Japan, May 2019.

14. ◯**Kanamaru M.**, Sasaki S., Wieczorek M., "Density Distribution Estimation of Asteroid Itokawa Based on Distribution of Smooth Terrain", *Lunar and Planetary Science Conference 50th, #1414*, Woodlands, Texas, USA, March 2019.

15. ◯Morota T., Cho Y., **Kanamaru M.**, et al., "Timescale of Reddening Process of the Ryugu Surface Based on the Crater Size Frequency Distribution", *Lunar and Planetary Science Conference 50th, #2833*, Woodlands, Texas, USA, March 2019.

16. ◯Cho Y., Morota T., **Kanamaru M.**, et al., "Spatial Distribution and Morphology of Craters on Ryugu: Implications for Surface Processes on the C-Type Asteroid", *Lunar and Planetary Science Conference 50th, #1751*, Woodlands, Texas, USA, March 2019.

17. ◯**Kanamaru M.**, Sasaki S., Wieczorek M., "Estimation of Interior Density Distribution for Small Solar System Bodies", *Japan Geoscience Union Meeting 2018, PPS03-14*, Chiba, Japan, May 2018.

18. ◯**Kanamaru M.**, Sasaki S., "Estimation of Interior Density Distribution for Small Solar System Bodies", *Lunar and Planetary Science Conference 49th, T202, #2902*, Woodlands, Texas, USA, March 2018.

19. ◯**Kanamaru M.**, Sasaki S., "Estimation of Interior Density Distribution for Small Bodies: The Case of Asteroid Itokawa", *Joint Conference: 31st ISTS, 26th ISSFD & 8th NSAT, a91657*, Ehime, Japan, June 2017.

20. ◯**Kanamaru M.**, Sasaki S., "Estimation of Interior Density Distribution for Asteroid Itokawa", *JpGU-AGU Joint Meeting 2017, PPS02-22*, Chiba, Japan, May 2017.

21. ◯**Kanamaru M.**, Sasaki S., "The Effect of Rotation Period on Slope Distribution on Asteroid Itokawa", *Japan Geoscience Union Meeting 2016, PCG10-06*, Chiba, Japan, May 2016.

Poster presentation

22. ◯**Kanamaru M.**, Sasaki S., "Estimation of Interior Density Distribution for Small Bodies: The Case of Asteroid 25143 Itokawa", *The 3rd COSPAR Symposium, P0156*, Jeju Islands, South Korea, September 2017.

23. ◯**Kanamaru M.**, Sasaki S., "Investigating the Effects of the Rotation and Interior Density Distribution on the Surface Gravity Field of Asteroid Itokawa", *Lunar and Planetary Science Conference 48th, T313, #2881*, Woodlands, Texas, USA, March 2017.

24. ◯**Kanamaru M.**, Sasaki S., "Surface mechanical evolution of Itokawa", *JSPS Core-to-Core Program "Planet2" Symposium 2017*, Villefranche sur Mer,

France, February 2017.

25. ◯**Kanamaru M.**, Sasaki S., "Surface gravity and topography on Itokawa", *International Workshop on "Exoplanets and Disks: Their Formation and Diversity III", P11*, Okinawa, Japan, February 2016.

Presentations at Japanese Conferences

◯Presenter

Oral presentation

26. ◯金丸仁明、佐々木晶、諸田智克、長勇一郎、平田 成、平田直之、千秋博紀、嶌生有理、田中智、杉田精司、渡邊誠一郎、「小惑星 Ryugu に働く YORP 効果の数値計算～自転状態の進化史の解明に向けて～」、衝突研究会「天体の衝突物理の解明 (XV) ～小惑星の表層進化～」、講演番号なし、東京、2019 年 11 月。

27. ◯金丸仁明、佐々木晶、Mark Wieczorek、諸田智克、長勇一郎、「小惑星 Ryugu のクレーター形状解析と内部密度分布構造の推定」、日本惑星科学会 2018 年度秋季講演会、S4、北海道、2018 年 10 月（ポスター発表付き口頭発表）。

28. ◯金丸仁明、佐々木晶、「多面体重力場計算モデルを用いた太陽系小天体内部の密度分布推定」、 日本惑星科学会 2017 年度秋季講演会、S7、東

京、2017 年 10 月（ポスター発表付き口頭発表）。

29. ◯金丸仁明、"Investigating the Effects of the Rotation and Interior Density Distribution on the Surface Gravity Field of Asteroid Itokawa"、京阪神・地球惑星物質科学研究会（京都大学・大阪大学・神戸大学 3 研究室合同の研究会）、講演番号なし、大阪、2016 年 12 月。

30. ◯金丸仁明、佐々木晶、「太陽系小天体における自転周期が表面重力場に与える影響」、日本惑星科学会 2016 年度秋季講演会、O6-01、岡山、2016 年 9 月。

31. ◯金丸仁明、佐々木晶、佐伯和人、「Disk Model を用いた小規模天体の重力場計算」、日本惑星科学会 2015 年度秋季講演会、O7-02、東京、2015 年 10 月。

32. ◯金丸仁明、「Disk Model を用いた小規模天体の重力場計算にむけて」、京阪神・地球惑星物質科学研究会（京都大学・大阪大学・神戸大学 3 研究室合同の研究会）、講演番号なし、大阪、2015 年 7 月。

Poster presentation

33. ◯金丸仁明、佐々木晶、Mark Wieczorek、「67P/Churyumov-Gerasimenko 彗星の密度分布構造の推定」、日本惑星科学会 2019 年度秋季講演会、P9、京都、2019 年 10 月。

34. ◯金丸仁明、佐々木晶、Mark Wieczorek、諸田智克、長勇一郎、「小惑星

Itokawa の密度分布構造の推定と小惑星 Ryugu のクレーター形状の解析」、大阪大学大学院理学研究科・基礎科学研究者養成プロジェクト研究成果発表会、#48、大阪、2019 年 3 月。

35. ◯金丸仁明、佐々木晶、「小惑星イトカワにおける表面重力場への自転周期と内部密度分布の影響」、衝突研究会「天体の衝突物理の解明 XII～水質変成から探る太陽系物質進化～」、講演番号なし、兵庫、2016 年 11 月。

36. ◯金丸仁明、佐々木晶、「イトカワの表面重力場と地形の相関」、第 28 回理論懇シンポジウム、講演番号なし、大阪、2015 年 12 月。

Collaboration Visit

37. Nice Observatory, France, October – December 2018.

- Collaborated with Dr. Mark Wieczorek.
- Investigated the internal structure of asteroid 25143 Itokawa.
- Funded by Cross-Boundary Innovation Program, Osaka University.

38. Nice Observatory, France, October – December 2017.

- Collaborated with Dr. Mark Wieczorek.
- Developed a numerical simulation of the gravity field and geology of small bodies.

- Funded by "International Network of Planetary Sciences", Core-to-Core Program, Japan Society for the Promotion of Science.

Professional Membership

39. Science Team Member of Hayabusa2 Project, Optical Navigation Camera Team, April 2017 – present.

- Data processing and validation of camera images and reflectance spectra for the spacecraft mission.
- Geological analysis of the target asteroid 162173 Ryugu such as crater mapping and measurement of crater diameters and depths.
- Numerical modeling of the evolution of Ryugu's spin state with regard to a thermal induced torque (YORP effect).

40. Member of Japan Geoscience Union, February 2016 – present.

41. Member of The Japanese Society for Planetary Sciences, August 2015 – present.